Hole Control in Photonic Crystal Fibres

Chen, Yong

Award date:
2014

Awarding institution:
University of Bath

Hole Control in Photonic Crystal Fibres

Yong Chen

A thesis submitted for the degree of Doctor of Philosophy

of the

University of Bath

Department of Physics

September 2013

Abstract

Photonic crystal fibres (PCFs) are special fibres with air holes which run along the whole fibre length. These holes not only determine the fibres' unique properties, but also provide a new degree of freedom for fibre modifications. In this thesis, we focus on hole control in PCFs from two perspectives: during their fabrication and after they have been made. We found for the first time that the direct information of viscosity was not necessary for description of the fibre drawing process. This conclusion matched our experimental results without recourse to any adjustable fitting parameters.

By post-processing of PCFs, which modifies the cladding and core structure and shape, we have achieved a series of novel devices for both linear and nonlinear applications. We have demonstrated fibre devices with cores resembling Young's double slits that have good performance in terms of compatibility and intensity enhancement for a specific application in fibre optic spectrometers.

The bulk of this thesis reports on higher-order modes and their nonlinear applications. We achieved all-fibre, low loss and broadband mode converters in highly nonlinear PCFs (HNPCFs) which converted the fundamental mode (LP_{01}) to a higher-order mode (LP_{02}), which can then be converted back if necessary. This higher-order mode has been used for supercontinuum (SC) generation and four wave mixing (FWM) at wavelengths unobtainable for the fundamental mode. This is achieved by utilising the profound dispersion properties of the higher-order mode. We also demonstrated another kind of mode conversion: from the fundamental mode to a Bessel-like beam or its Fourier transform version, an annular beam. Three different methods were implemented experimentally to achieve this non-diffractive, self-healing beam.

Acknowledgements

First of all, I would like to thank my supervisor Tim Birks for giving me an opportunity to study at Bath and for believing in me throughout my PhD study. Thank you also for all the supervision, encouragement and inspiration.

William Wadsworth, my second supervisor and an amazing mentor, gave me so much good advice and answered so many questions. Thank you.

Thank yous also go to Jim Stone, the guy who opened the fibre fabrication "door" for me. And thank you for proofreading this thesis.

I would also like to thank Steve Renshaw, John Mitchels, Paul Reddish, Wendy Lambson, and Alan George for sharing expertise in your respective fields.

Thanks to David Bird for allowing me using your PCF modelling code.

I also thank all the members of CPPM, past and present, for making it a truly nice and friendly place to study.

Thank you to all my Chinese friends in the Physics department for making our lunch time no longer boring.

Special thanks should go to Bob Draper for your help during my tough time and for teaching me how to drive.

My final gratitude would go to my family. I would like to thank my parents for your continuous love and support. Thank you to my wife, for always being there for me and for your love. Finally, to my little girl, your smile is a great gift to me, always!

For my family

Contents

Introduction

A photonic crystal fibre is a novel type of optical waveguide, with periodic holes which run along the whole fibre length. The fibre is normally made from a single material, and was conceived and realised by Russell and colleagues in the 1990s [1–3]. The original idea was to trap light in a hollow fibre by the effects of photonic bandgap guidance (PBG) through the construction of a periodic wavelength-scale structure – a photonic crystal, which had been first proposed in an unpublished work [3]. This led to the first theoretical demonstration done by Birks et al., which showed that there indeed exists 2 - D photonic bandgap in such a silica-air structure for out-of-plane propagation of light [1], and several breakthroughs in the experimental realisation in the next few years [2, 4, 5]. The first working PCF was fabricated by Knight et al. in 1996 [2] and led to the discovery of endlessly single mode PCFs [6] as well as many other intriguing properties. The light in this PCF, however was not guided by the so called photonic bandgap effect, instead it was guided by a mechanism denoted as modified total internal reflection. This type of PCF is the main research topic of this thesis. The first photonic bandgap fibre (PBGF) and first fibre which demonstrated photonic bandgap guidance in air, also called hollow core PCF, were realised in 1998 [4] and 1999 [5], respectively.

Although the guidance mechanisms in modified total internal reflection fibres and photonic bandgap fibres are totally different, the ways in which they are fabricated are very similar. Currently the most commonly used method is known as the stack and draw technique [2]. The key component of a PCF is its air holes. The parameters of these holes, like size and distribution, determine its optical properties. In practice, PCFs are drawn in a furnace from preforms that also contain holes. In contrast to features in ordinary solid fibres (like step-index fibres), these holes can profoundly change in size (and indeed in shape) relative to the fibre as a whole, under the influence of surface tension, glass viscosity and pressure differences. To produce PCFs of given designs it is therefore important

to understand how such parameters will affect the final holes, especially from an experimenter's view.

By choosing different designs and fabricating under different conditions, fibres drawn on the fibre drawing tower can vary remarkably and can hence meet different applications. However, they could not do enough to meet all requirements: fibre drawing has its limitations. Post-processing of fibres that have already been drawn becomes important in such cases. Normally the length scale of fibres under post-processing is quite short (sometimes just a few centimetres or millimetres), which is not easy to achieve on a fibre drawing tower. Post-processing is not a new concept for people who are familiar with fibre tapers [7] and fibre gratings [8] in conventional fibres and these devices can also be formed in PCFs by using similar techniques. For example, PCFs can be tapered like conventional fibres to get a narrowed waist, which is connected to untapered fibre at both ends by taper transitions [9]. Submicron PCF cores were made from a PCF with a normal size core (a few microns) with low loss [10]. Different fibre gratings were also realised in PCFs [11, 12].

It should be pointed out again that PCFs are special fibres with air holes in the cladding. These holes provide an extra degree of freedom to change the fibre structure and optical properties when compared to conventional fibres. By applying heating, holes can be collapsed partially to reduce the fibre's air-filling fraction or collapsed totally to form a new core. If pressure is also applied, holes can be inflated or kept at their original size [13]. Furthermore, when a differential pressure is applied, different holes can behave differently depending on individual conditions. Combining these post-processing techniques, a large number of different devices for different applications have been achieved or can be envisioned easily. Some of the devices contributing significantly to this thesis are beam shapers (those changing fibres' mode size or shape), mode filters and mode convertors.

Optical fibres are a good medium for observing nonlinear effects owing to their capability of providing tight optical confinement and long interaction length. With the invention of low loss optical fibres in the 1970s, almost all the principal nonlinear effects that had previously been observed in bulk materials were reinvestigated and reported under simpler conditions [14]. These included Stimulated Raman Scattering (SRS) [15] and Stimulated Brillouin Scattering (SBS) [16], which were studied as early as 1972. Other nonlinear effects such as FWM [17, 18], self phase modulation (SPM) [19], and optical solitons [20] were observed just a

few years later.

All of these effects contribute to new wavelength generation and spectral broadening. However, before the advent of PCFs, there had not been serious research interest in the spectral broadening, as the maximum achievable bandwidth was quite limited. The photonic crystal fibre, unquestionably, has been a driving force for the spectacular spectral broadening phenomenon, supercontinnum (SC) generation. The importance of PCFs for SC generation can be summarised in two main reasons. The first reason is that light can be tightly confined into a small area due to the large refractive index difference between silica core and air cladding. This enhances the power density and makes it easier for nonlinear effects to occur. The second and more critical reason, is that the dispersion profiles of PCFs can be easily engineered to match the wavelength constraints of pump sources.

Until now, almost all efforts about SC generation and individual nonlinear effects were focused on the Gaussian-like fundamental mode. This is probably due to the reason that the fundamental mode's field distribution most closely resembles those of external light sources and systems like laser beams, transmission fibres or spectrometers, greatly simplifying input and output coupling. However, higher-order modes have desirable properties for nonlinear generation and propagation [21–23]. In order to utilise these properties, special devices are needed to excite a single higher-order mode and return the nonlinearly-generated wave back to the fundamental mode at the output. This problem can be solved by our post-processing techniques, which enable us to generate a pure higher order mode through a broadband, low-loss, all fibre mode convertor. Generally speaking, our mode convertors provide a low-loss and broadband tool for investigating this unexplored space of possibilities.

This thesis covers several topics relating to photonic crystal fibres, ranging from PCF fabrication to the post-processing of PCFs for different applications. In particular, by taking advantage of mode convertors, we focused on SC generation and FWM in higher-order modes. Interestingly, all of these are related to hole control, either during or after fibre fabrication.

This thesis is organised as follows:

Chapter 1 provides comprehensive background information about optical fibres. After a brief description of conventional optical fibre and PCFs, it goes on to describe optical fibres' linear properties, such as loss, modes and dispersion. The way how to fabricate a PCF is also covered in this chapter. The final part of

this chapter is about optical nonlinearity, which is important for understanding results presented in Chapters 6 and 7. Chapter 2 provides further background information, about optical fibre transitions and tapering. More importantly, several post-processing techniques are described in detail in this chapter.

Chapters 3 to 8 present the new research finished during my PhD study. Chapter 3 discusses the fibre fabrication process. The hypothesis and modelling is explained first. The experimental results are shown later to check the validity of modelling. Chapter 4 moves to the post-processing of fibres after they have been fabricated. A novel Young's double slits design is presented. Some preliminary results are shown.

Chapters 5 to 7 focus on a specific mode convertor: LP_{01} to LP_{02} mode convertor and its applications in SC generation and FWM. Chapter 5 is devoted to the linear part of this project. After presenting the simulation results, the way how to fabricate such a device is discussed. A detailed characterisation of mode evolution and loss is included. Chapter 6 first discusses the unique dispersion properties of higher order modes and analyses how it relates to UV and blue supercontinuum generation, followed by detailed experimental results. Chapter 7 focuses on FWM in this higher-order mode.

Chapter 8 moves back to linear propagation and concentrates on post-processing of PCFs for Bessel beam generation. Three different ways are implemented to realise this ultra higher order mode. Self-healing and diffraction-free properties are also presented.

Chapter 9 summarises all the results obtained.

Appendix A describes how to derive the model presented in Chapter 3.

At the end of this introduction I would like to acknowledge explicitly my collaborators' contribution and then separate my own work. The background work summarised in Chapter 2 about tapering and post-processing techniques were mainly developed by Tim Birks and William Wadsworth before I joined (although some of the data presented there is mine). Tim Birks contributed the theory described in Chapter 3, which was confirmed by my experimental results there. The detailed derivation of this theory is included in Appendix A for completeness. Tim Birks simulated microwires and mode convertors, mainly in Chapters 5 and 6. He also simulated generic PCFs in Chapter 6, while the experimental fibres were simulated by myself. William Wadsworth helped me understanding the nonlinear experimental results I obtained. He also contributed the data for Fig. 7.1. The second device for generating Bessel beams was ini-

tialised by Jim Stone. I then joined this project and obtained all the experimental results presented in this thesis.

Chapter 1

Basics of optical fibres

This chapter is intended to give an introduction to optical fibres, including both conventional fibres and PCFs and their linear and nonlinear properties. Sections 1.1 and 1.2 describe optical fibre structures and how fibres guide light. The linear properties, like loss, modes and dispersion are discussed in Sections 1.3-1.5. Section 1.6 concentrates on PCF fabrication. In Section 1.7 nonlinear effects in optical fibres are reviewed. A short summary of this chapter is provided in Section 1.8.

1.1 Conventional optical fibres

Generally speaking, an optical fibre is a very thin, highly flexible, nearly transparent dielectric medium for transporting optical information and energy from one place to another [24]. The cross section of a fibre is generally divided into three layers: the core, cladding and jacket or coating, as shown in Fig. 1-1. The fibre core typically has a diameter ranging from several micrometres to several

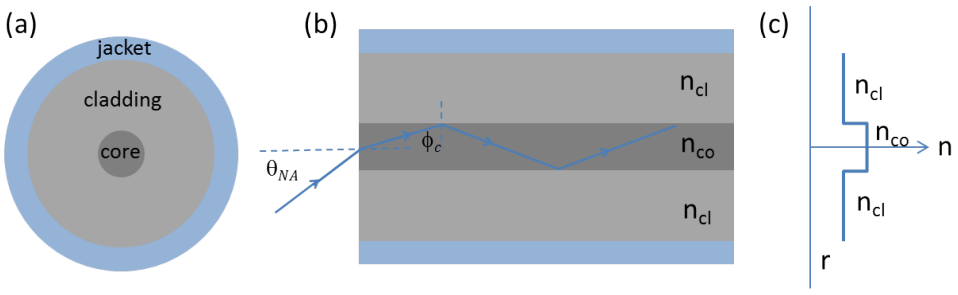

Fig. 1-1: (a) Schematic diagram of the cross section of a conventional fibre; (b) Fibre side view and TIR mechanism; (c) The refractive index profile.

tens of micrometres, depending on if it is a single mode or multimode fibre. It is surrounded by a lower-index cladding layer to provide a refractive index difference for light guidance. Both the core and cladding are made from fused silica with different dopants to adjust the refractive index slightly [24–26]. The typical outer diameter of the cladding is 125 μm for most single mode and multimode fibres. Coating the outside of the fibre there is a plastic jacket to protect the fibre from contamination and damage. More importantly, it has a higher refractive index compared with that of the cladding, so unguided modes will be refracted away and absorbed.

The refractive index profile $n(r, \theta)$, where r represents the cylindrical radial coordinate and θ represents the azimuthal coordinate, does not usually change along the fibre length (z coordinate). However, different fibres may have different profiles of $n(r, \theta)$. The refractive index of silica changes a little when doped, either increased or deceased, depending on the properties of dopants [24]. For example, GeO_2 and P_2O_5 have higher refractive indices than pure silica and so can be used as dopants for fabrication of the core. On the other hand, B_2O_3 and F are suitable for the cladding since they can lower the refractive index of silica. In their simplest form, fibres have a uniform high refractive index within the core and a sharp decrease of refractive index at the core-cladding interface, so that the cladding is of a lower refractive index, as shown in Fig. 1-1(c). This kind of fibre is generally called a step-index fibre to distinguish it from a graded-index fibre in which the refractive index of the core decreases gradually from centre of the fibre to the core-cladding boundary.

The basic mechanism for guiding light in optical fibres, total internal reflection (TIR), has been known from the mid nineteenth century [27, 28]. Light rays incident upon the core-cladding boundary will be partially reflected and partially transmitted. When the angle of incidence is greater than a specific value, which is called the critical angle [28], light will be totally reflected by TIR and confined within the core. The critical angle is given by:

$$\phi_{\mathrm{c}} = \arcsin(\frac{n_{\mathrm{cl}}}{n_{\mathrm{co}}}) \tag{1.1}$$

where n_{cl} and n_{co} indicate the refractive indexes of the core and cladding, respectively. From Eq. (1.1), it is obvious that the core must have a higher refractive index than that of the cladding. Typically, the normalised index difference Δ, which is defined by $\Delta = \frac{n_{\mathrm{co}}^2 - n_{\mathrm{cl}}^2}{2n_{\mathrm{co}}^2} \approx \frac{n_{\mathrm{co}} - n_{\mathrm{cl}}}{n_{\mathrm{co}}}$, is about 0.2% for single mode and

about 1% for multimode fibres [24].

As discussed before, only those light beams whose incidence angles at the core-cladding boundary exceed the critical angle can propagate along the fibre. The numerical aperture (NA) of a fibre is the parameter that represents its light gathering capability, defined as the sine of the maximum angle of an incident light ray upon the fibre end that becomes totally confined in the fibre. The expression for NA is [24]:

$$\mathrm{NA} = \sin\theta_{\mathrm{NA}} = \sqrt{n_{\mathrm{co}}^2 - n_{\mathrm{cl}}^2} \tag{1.2}$$

NA is a very important parameter when considering the efficiency of coupling between a light source and a fibre as well as the loss when splicing between fibres.

1.2 Photonic crystal fibres

A photonic crystal fibre is an optical fibre that incorporates a periodic arrangement, like an array of air holes, running along its length [1–3]. As opposed to conventional optical fibres, PCFs typically are made from just one material - pure silica. This particular type of fibre offers considerable degrees of freedom to achieve unique properties, many of which cannot be expected from conventional optical fibres. These innovative properties attract numerous researchers from all around the world, and make these fibres interesting for a wide range of applications.

There are two main types of PCFs, which depend on the material of the core: solid core photonic crystal fibres (solid-core PCFs) and hollow core photonic crystal fibres (HC-PCFs). If categorised by guiding mechanisms, they can be divided into index-guiding PCFs (guided by modified total internal refection) and bandgap-guiding PCFs (also called photonic bandgap fibres (PBGFs), guided by photonic bandgap effect). In order to characterise the structure of a PCF, there are some important parameters which need to be defined. These parameters are shown in Fig. 1-2, where d denotes the diameter of holes and Λ is defined as the pitch (hole-to-hole separation). The value of d/Λ determines the air-filling ratio, which is very important for the endlessly single mode property of PCFs.

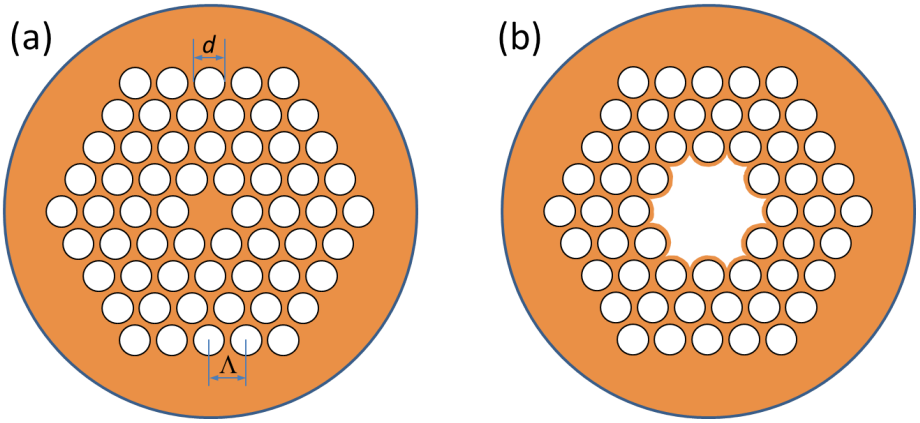

Fig. 1-2: The basic structure of (a) index-guiding PCFs and (b) bandgap-guiding PCFs. Silica regions are represented in gold, while air is represented in white. Here d is the hole diameter, while Λ represents the pitch.

1.2.1 Index-guiding PCFs

An index-guiding PCF generally has a solid core surrounded by periodic air holes in the cladding. The guidance principle of this case is analogous to that of conventional fibres: light is bounded in a solid core by taking advantage of the refractive index contrast between the core and cladding. In an index-guiding PCF, the periodic inclusions in the cladding of lower refractive index material (air holes) reduce the effective refractive index of the cladding. For conventional optical fibres, the typical way to change the index difference between the core and cladding is to change the dopant concentration and materials. However, this method is limited by doping related attenuation. In PCFs, the refractive index difference actually depends on the effective refractive index of the cladding, which can be changed by design over a large range. This freedom of design offers a wonderful opportunity for tailoring the dispersion of a PCF, which will be described in detail later.

1.2.2 Bandgap-guiding PCFs

When the PCF core region has a lower refractive index than the surrounding photonic crystal cladding, light cannot be guided by the traditional way (TIR). However, light can be guided by a photonic bandgap (PBG) [4, 5]. In this kind of confinement, the relatively higher refractive index of the fibre core is no longer crucial to achieve guidance. The periodic, wavelength-scale lattice of microscopic holes in the cladding is a two-dimensional photonic crystal [3, 29, 30], where light

in certain combinations of wavelength and β cannot propagate. It means that this light will be trapped in the core and cannot leak out. This guiding mechanism is quite unusual and cannot be obtained in conventional optical fibres and it opens a whole new set of interesting possibilities.

It should be stressed that this thesis will focus on index-guiding PCFs and the concept of PBGF is mentioned here just for completeness.

1.3 Loss

The power reduction of a signal when propagating along an optical fibre is called the loss. A number of mechanisms can contribute to the total loss of a fibre. Based on the type of mechanism, the loss can be divided into two main categories: intrinsic and extrinsic losses [24]. Intrinsic loss comes from the properties of the materials used to manufacture the fibre and can be reduced by choosing appropriate materials and improving fabrication processes. In contrast, the extrinsic loss has its origins in the imperfections during fibre fabrication processes and can be reduced to a very low level. There are three main intrinsic loss mechanisms for a fibre: unltraviolet (UV) absorption, infrared (IR) absorption and Rayleigh scattering. The UV absorption has an electronic origin and sets the short wavelength edge of the transparency window of silica, which spans from about 0.2 to 2.5 μm [31]. However, for wavelengths longer than 400 nm, the contribution of UV absorption is relative small and this gives way to another intrinsic loss mechanism for the fundamental limit for the loss below 1600 nm: Rayleigh scattering. Rayleigh scattering is proportional to λ^{-4} (λ is the wavelength) and caused by density fluctuations (leading to refractive index fluctuations) of SiO_2 and other dopant molecules during fibre fabrication process. It has been reported that Rayleigh scattering can be reduced through thermal treatments, like annealing [32]. The IR absorption arises from the lattice vibration modes of silica and dopant glasses. The most important extrinsic loss is the one caused by the presence of OH. The OH ions have a strong absorption peak around 2.75 μm and several overtones across the whole transparency window of silica, such as those at 1.38 μm and 0.95 μm. The waveguide imperfections give rise to another extrinsic loss. The features of these loss mechanisms is summarised in Fig. 1-3.

Apart from the aforementioned factors which affect the loss properties, there are more which need to be considered for PCFs. The confinement loss arises from the finite extent of the periodic cladding structure and needs to be accounted for

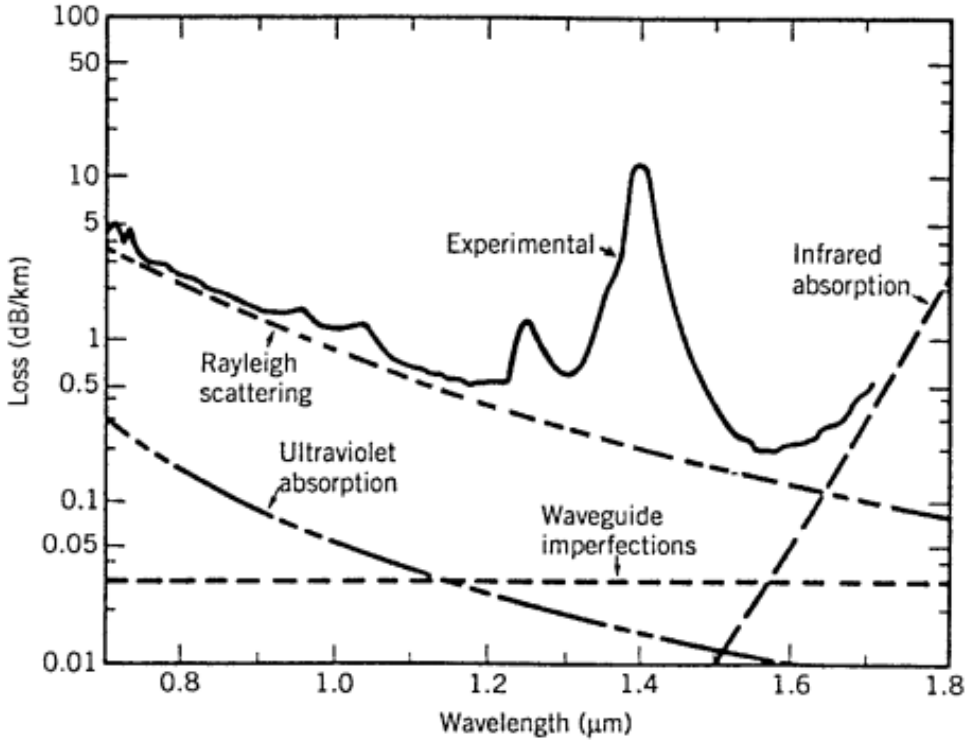

Fig. 1-3: Typical loss spectrum of a conventional fibre, showing different mechanisms contributing to the total loss (From Ref. [24]).

during PCF design. The surface quality of holes surrounding the core plays a key role for the reduction of loss for solid core PCF [33]. For hollow core PCFs, it was suggested that the ultimate loss is limited by the surface roughness originated from frozen-in surface capillary waves [34].

Currently, the lowest loss for a conventional step-index fibre is 0.148 dB/km at 1570 nm, and this fibre has a pure silica core and fluorine doped cladding [35]. For a solid core PCF, the lowest loss value reported so far is 0.18 dB/km, obtained by reducing the hole surface imperfections [33]. For hollow core PCFs, this value has the potential to be lower, as light in this kind of fibre is supposed to travel in air instead of silica. However, until now the lowest number achieved is 1.2 dB/km [34], much higher than its counterparts.

There are many methods which can be chosen to measure the loss of a fibre. Among them, the cut-back technique has been intensively used [36] and it is also the way measurements were made for this thesis. After the power (P_{o}) at the output end of a fibre has been measured, a piece of fibre with length of L is cut off and the power (P_{i}) at the new end is recorded and measured again. During these processes, the input coupling condition should not be changed. The loss is

given by:

$$\alpha_{\mathrm{dB}} = -10\log_{10}(\frac{P_{\mathrm{o}}}{P_{\mathrm{i}}}) \tag{1.3}$$

The attenuation is expressed as loss per unit length (α_{dB}/L). The schematic diagram is shown in Fig. 1-4. This technique also can be used to measure the insertion loss of optical devices with essentially the same procedure.

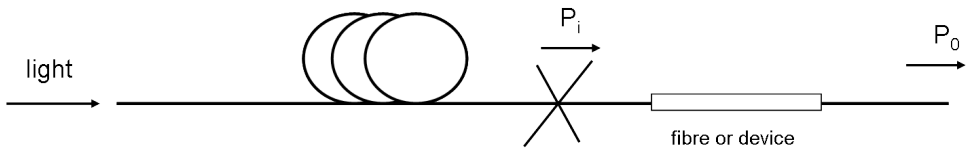

Fig. 1-4: Schematic diagram of the cut-back technique for measuring loss.

1.4 Modes

1.4.1 General information

A light wave whose field distribution does not change during its propagation along a fibre, except for phase, is called a mode of the fibre. In practice, by solving Maxwell's equations and applying appropriate boundary conditions, one is able to find all the allowed modes in a fibre with the knowledge of the physical parameters. Each one has a specific light distribution pattern and its full description involves six-component hybrid electromagnetic fields. There is an important parameter, β, which is the component of the wave vector along the fibre axis and called propagation constant, corresponds to each mode. Only a finite number of modes are guided in a fibre. This also means just certain values of β are allowed and satisfy the following condition [24]

$$\kappa n_{\mathrm{cl}} < \beta < \kappa n_{\mathrm{co}} \tag{1.4}$$

where $\kappa = 2\pi/\lambda$. The reason for $\kappa n_{\mathrm{cl}} < \beta$ is that the mode should be confined in the core by TIR. The higher β is, the lower the order of the mode is.

The first mode (with the highest β) is called the fundamental mode. The number of modes can be guided in a specific fibre is determined by its physical parameters and the guided wavelength, which can be described by the V value [37]

$$V = \frac{2\pi}{\lambda} a (n_{\mathrm{co}}^2 - n_{\mathrm{cl}}^2)^{1/2} \tag{1.5}$$

where a is the core radius. The relation between the V value and how many modes are guided in a fibre is shown in Fig. 1-5. According to their polarization properties, these mode can be divided into four categories: transverse electric (TE) modes, transverse magnetic (TM) modes and hybrid (HE and EH) modes. For a TE mode, the axial component of the electric field becomes zero, therefore the electric field lies entirely in the transverse plane. While for a TM mode this is true for the magnetic field. In the case of HE and EH modes neither field is completely transverse. In Fig. 1-5, it is obvious that all higher order modes are cut off and just the HE_{11} mode still exists when $V < 2.405$. In this case, we call HE_{11} mode the "fundamental mode" and it never be cut off in step index fibres.

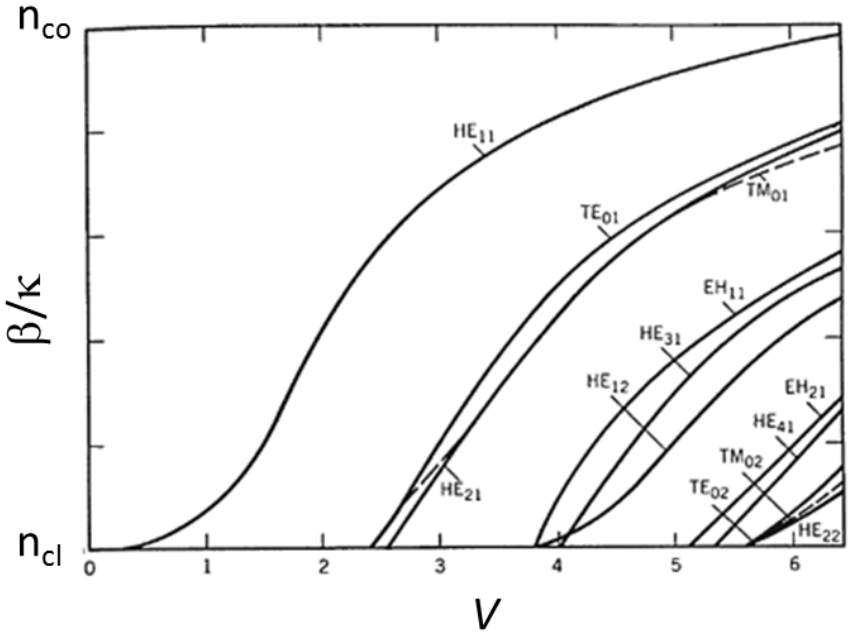

Fig. 1-5: The mode index β/κ as the function of the V parameter (From Ref. [38]).

Generally speaking, we can get an exact mode description. However, the process is quite complex and may not be necessary. In most cases, the index difference between the core and cladding is very small. In this situation, a scalar "weak guidance" approximation can be applied [7]. Within this assumption, linearly polarised modes $\mathrm{LP}_{\ell \mathrm{m}}$ substitute the vector modes $\mathrm{TE}_{0\mathrm{m}}$, $\mathrm{TM}_{0\mathrm{m}}$, $\mathrm{HE}_{\ell \mathrm{m}}$ and $\mathrm{EH}_{\ell \mathrm{m}}$. The relations between them are summarised in Table 1.1.

The subscripts ℓ and m of an LP mode can be used to deduce the mode's

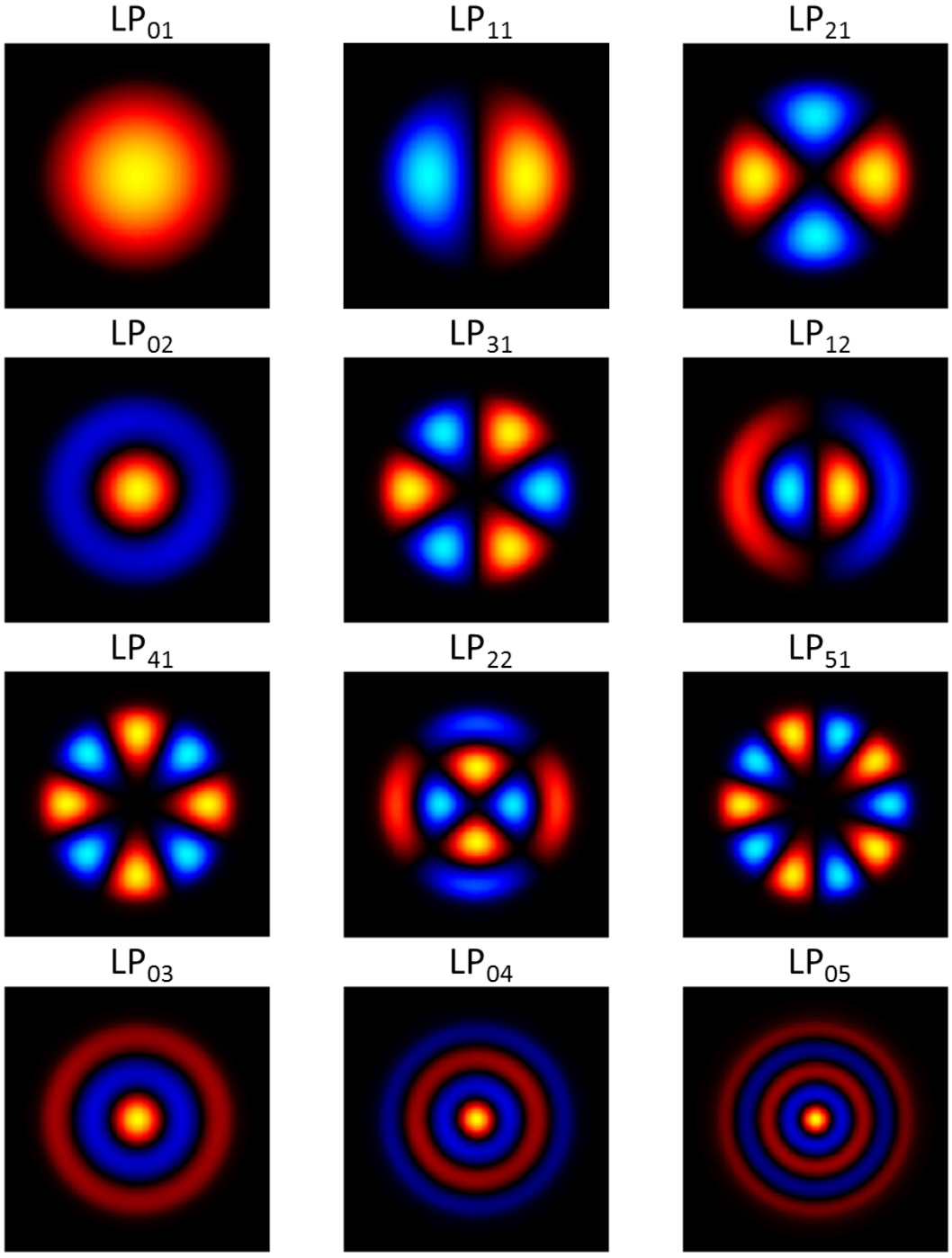

Fig. 1-6: Electric field (E) amplitude profiles of some LP modes. Red and blue represent opposite signs of E.

Table 1.1: Relations between LP modes and exact vector modes

LP mode	Corresponding vector mode
LP_{0m}	HE_{1m}
LP_{1m}	HE_{2m}, TE_{0m}, TM_{0m}
$LP_{\ell m}(\ell \geq 2)$	$HE_{\ell+1,m}$, $EH_{\ell-1,m}$

intensity profile. The value of 2ℓ gives the number of maxima (or minima) in the intensity in the azimuthal direction, while the other parameter m gives the number of maxima in the intensity in the radial direction [24, 39]. Some low order modes are shown in Fig. 1-6.

1.4.2 Endlessly single mode PCFs

According to Eq.(1.5), a single mode fibre actually supports many modes if the wavelength of guided light is short enough. This means all conventional fibres will lose their single mode property beyond a critical wavelength. But this is not always the case for PCFs. One of the intriguing properties of a PCF is that, by appropriately designing its cladding structure, it can be endlessly single mode [6].

In the case of a PCF, the refractive index in the cladding is not uniform. There is not a constant value for n_{cl} as in the case of step-index fibres at a specific wavelength. Instead other parameters are needed to describe it, like the effective cladding index, n_{eff} and propagation constant of the fundamental space-filling mode, β_{FSM}, with the relation:

$$n_{\mathrm{eff}} = \beta_{\mathrm{FSM}}/\kappa \tag{1.6}$$

The fundamental space-filling mode is the fundamental mode of the infinite photonic crystal cladding [6].

Then the V value in PCFs can be defined as [6]

$$V_{\mathrm{eff}} = \frac{2\pi\Lambda}{\lambda}(n_{\mathrm{co}}^2 - n_{\mathrm{eff}}^2)^{1/2} \tag{1.7}$$

where the pitch Λ is used instead of the core radius since the core radius in a PCF is not well defined.

Compared with conventional optical fibres whose V increases monotonously when decreasing the wavelength, the way how V (or can be called V_{eff} here) in PCFs changes is more complex, for the reason that n_{eff} is wavelength dependent. For the light of shorter wavelength the field pattern becomes more concentrated

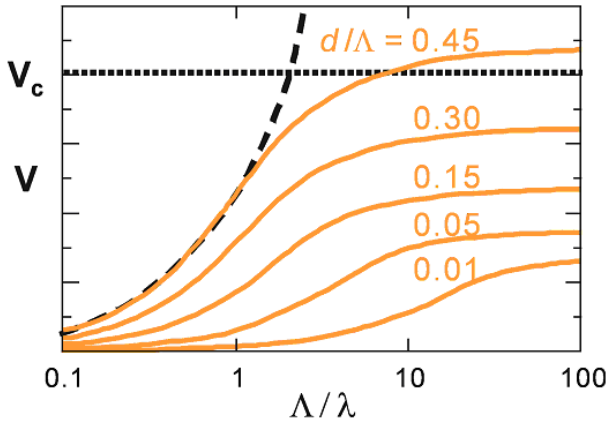

Fig. 1-7: Variation of V parameter with Λ/λ for a range of values of d/Λ (solid lines). The results for a typical conventional fibre (broken line) is also included for comparison (From Ref. [42]).

in the silica regions and avoids the holes, which means higher effective cladding index. This counteracts the dependence on wavelength in the denominator in Eq. (1.7). This implies, in some situations, one can extend single mode range to a very short wavelength, or even for all wavelengths, in this case the fibre is said to be endlessly single mode [6].

The variation of V with Λ/λ for PCFs with different values of d/Λ is shown in Fig. 1-7. The dashed curve which illustrates the V value of a typical conventional fibre is also included for comparison. When $\lambda \to 0$, and hence $\Lambda/\lambda \to \infty$, the V value increases monotonously in conventional fibres, however it approaches a constant in the PCFs. If we use the definition shown in Eq.(1.7) for PCFs, the second mode is cutoff around V value of 4.1 instead of 2.405 for that of conventional step-index fibres [40]. This means that for a small enough d/Λ (around 0.4), the fibre becomes endlessly single mode.

It should be noted that all the discussions above are based on one defect case, which just one hole is missing to form the core in the periodical lattice. For the case of the core formed by more than (less than) one hole (in other words, the diameter of core is bigger (smaller) than $2\Lambda - d$), similar but more rigorous(loose) condition need to be fulfilled. For example, d/Λ less than 0.165 was suggested for endlessly single mode when the core was formed by a 3-hole-missing design [41].

1.5 Dispersion

1.5.1 General information

Dispersion is another important property to characterise an optical fibre. It describes how different components of optical waves, such as frequencies and modes, travel at different speeds in a fibre. For a particular mode, the dispersion manifests itself through the frequency dependence of the mode's propagation constant β. This phenomenon is also referred to as chromatic dispersion, for it involves frequency (colour). Mathematically, one can expand β in a Taylor series about the centre frequency ω_0 to get a physical meaning about effects of dispersion [37]:

$$\beta(\omega) = n(\omega)\frac{\omega}{c} = \beta_0 + \beta_1(\omega - \omega_0) + \frac{1}{2}\beta_2(\omega - \omega_0)^2 + \cdots , \tag{1.8}$$

where $n(\omega)$ is the refractive index and

$$\beta_m = (\frac{d^m\beta}{d\omega^m})_{\omega=\omega_0}, \qquad m = 0, 1, 2, 3, ... \tag{1.9}$$

β_1 and β_2 are related to $n(\omega)$ and its derivatives through the relations [37]

$$\beta_1 = \frac{1}{\upsilon_g} = \frac{n_g}{c} = \frac{1}{c}(n + \omega\frac{dn}{d\omega}) \tag{1.10}$$

$$\beta_2 = \frac{1}{c}(2\frac{dn}{d\omega} + \omega\frac{d^2n}{d\omega^2}) \tag{1.11}$$

where n_g and υ_g are the group index and group velocity, respectively. In this definition, β_1 is the group delay, and β_2 represents the group-velocity dispersion (GVD) [37]. In engineering the dispersion parameter, D (in ps/(km·nm)), defined as $d\beta_1/d\lambda$, is normally used to describe the dispersion. D is related to β_2 by

$$D = -\frac{2\pi c}{\lambda^2}\beta_2 \tag{1.12}$$

For bulk-fused silica the refractive index $n(\omega)$ can be described by the Sellmeier equation

$$n^2(\omega) = 1 + \sum_{j=1}^{m}\frac{B_j\omega_j^2}{\omega_j^2 - \omega^2} = 1 + \sum_{j=1}^{m}\frac{B_j\lambda_j^2}{\lambda^2 - \lambda_j^2} \tag{1.13}$$

where $\lambda_j = 2\pi c/\omega_j$, c is the speed of light in vacuum. And $B_1 = 0.6961663$, B_2

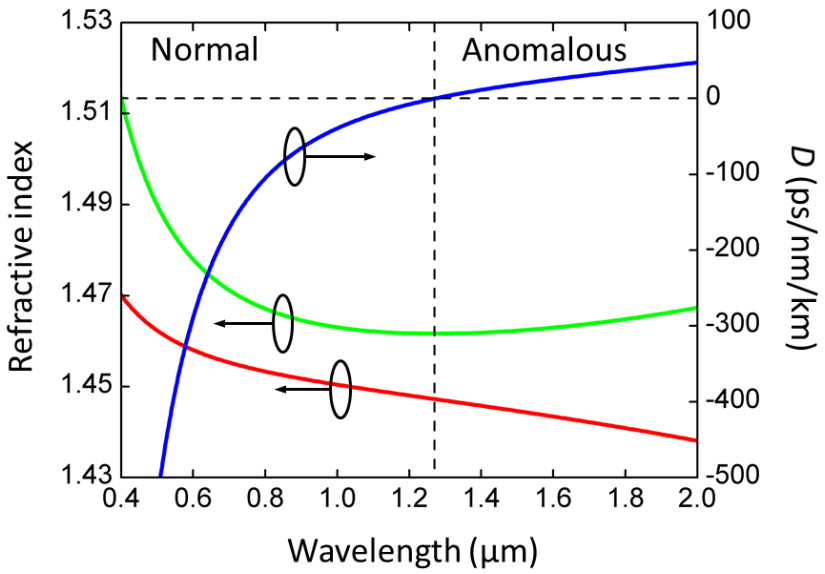

Fig. 1-8: Variation of refractive index n (red), group index n_g (green) and dispersion D (blue) with wavelength for fused silica.

= 0.4079426, B_3 = 0.8974794, λ_1 = 0.0684043 μm, λ_2 = 0.1162414 μm, and λ_3 = 9.896161 μm, which are obtained experimentally [43].

Fig. 1-8 shows the wavelength dependence of n_g and D of bulk silica calculated from the above. The most important feature is that D becomes zero at a wavelength of about 1.27 μm. This wavelength is an important parameter of a fibre, which is known as the zero dispersion wavelength (ZDW). Accordingly, the wavelength region where $D < 0$ ($\beta_2 > 0$) is called the normal dispersion regime. In contrast, the wavelength region where $D > 0$ ($\beta_2 < 0$) is called the anomalous dispersion regime [37].

It should be noted that the aforementioned dispersion for bulk-fused silica is actually the material dispersion. Another kind of chromatic dispersion, called waveguide dispersion, should be included when waveguide effects becomes important. The total dispersion is the combination of these two. As a result of this, the experimentally measured ZDW for a standard single mode fibre is around 1.31 μm [37].

When a fibre supports more than one mode, another dispersion named intermodal dispersion needs to be considered. This is because the group velocities are different for different modes even at the same wavelength. Normally, for a step-index fibre the fundamental mode travels faster than other higher-order modes. Differential group delays between different modes of the order of several nanoseconds per kilometre are possible in these fibres. This is the reason why single mode

fibres are used in long-haul telecommunication system, although more and more studies have been done recently to extend it to a multi-mode regime [44, 45].

1.5.2 Dispersion engineering in PCFs

One of the main features of a PCF is that its dispersion properties can be remarkably engineered to match different applications. The dispersion profile, especially the position of ZDW, is important for the nonlinear work presented in this thesis, like the SC and FWM discussed in Chapters 6 and 7.

The total dispersion of a fibre mainly consists of material dispersion and waveguide dispersion. A modification to either of them will changes the overall dispersion properties. As mentioned before, it is possible to change the material dispersion by changing dopant types and dopant concentration levels [25, 26]. This also affects the core-cladding refractive index difference, which modifies the waveguide dispersion properties as well. Furthermore, the core size of a fibre can be varied, which is another way for changing waveguide dispersion.

The scope of dispersion engineering of conventional fibres is limited compared with PCFs. The weak core-cladding refractive index difference (usually less than 1%) of a conventional fibre means the contribution of waveguide dispersion to the overall dispersion is generally quite small. Even for a high germanium dopant level of 30 mol%, the refractive index difference between the core and cladding is still just around 3% [14]. Furthermore, a high dopant concentration always brings high scattering loss. In contrast, the core-cladding refractive index difference can be made quite large in PCFs. In principle, the average index of the cladding of a PCF can be close to that of air if a high air filling fraction is considered, while the core index remains similar to that of silica. As a result of this large refractive index contrast, the waveguide effect is more prominent and plays a much important role than in a conventional fibre.

The waveguide effect can be understood from the wavelength dependence of the guided mode's effective index for a fixed core size. If the wavelength of light is much less than the diameter of the core, light stays predominately in the core and the modal index approaches the refractive index of the core material. However, when core size is much smaller than the wavelength, light expands and spreads into the cladding. The mode effective index close to the refractive index of cladding. Therefore, the tendency is that mode effective index deceases when wavelength increases. The detailed relationship depends on the exact structure

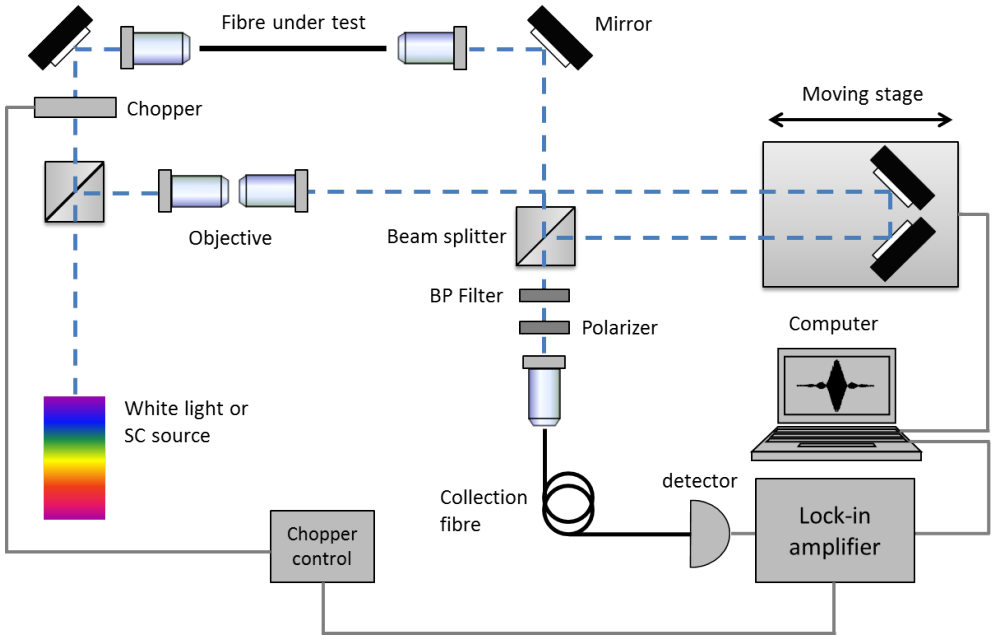

Fig. 1-9: Schematic diagram for dispersion measurement using the low-coherence white-light interferometric technique. BP filter is the bandpass filter.

and the refractive index contrast between the core and cladding [14].

It should be stressed that dispersion management in PCFs is very easy and flexible. There is a lot of design space which can be used for this purpose. For example, the hole to hole pitch, hole diameter and core diameter can be adjusted to obtain a desired dispersion profile.

1.5.3 Dispersion measurement

In this thesis, the dispersion is measured using a low-coherence white-light interferometric technique [46], which is based on a Mach-Zehnder interferometer. The experimental setup is shown in Fig. 1-9. The white supercontinuum light source is split into two beams and propagates along the two arms of the interferometer. One arm contains a short piece of fibre under test, while the other is in free space with a movable mirror stage to change the optical path in this arm. These two beams are recombined in a second beam splitter and collected by a short piece of fibre. The bandpass filter is used for selecting a narrow wavelength band for the measurement. If the fibre is birefringent, a polariser is used for choosing different polarisation directions. As the signal received is normally quite weak, a lock-in amplifier is necessary in our experimental setup.

The basic idea of this dispersion measurement method is that when the light

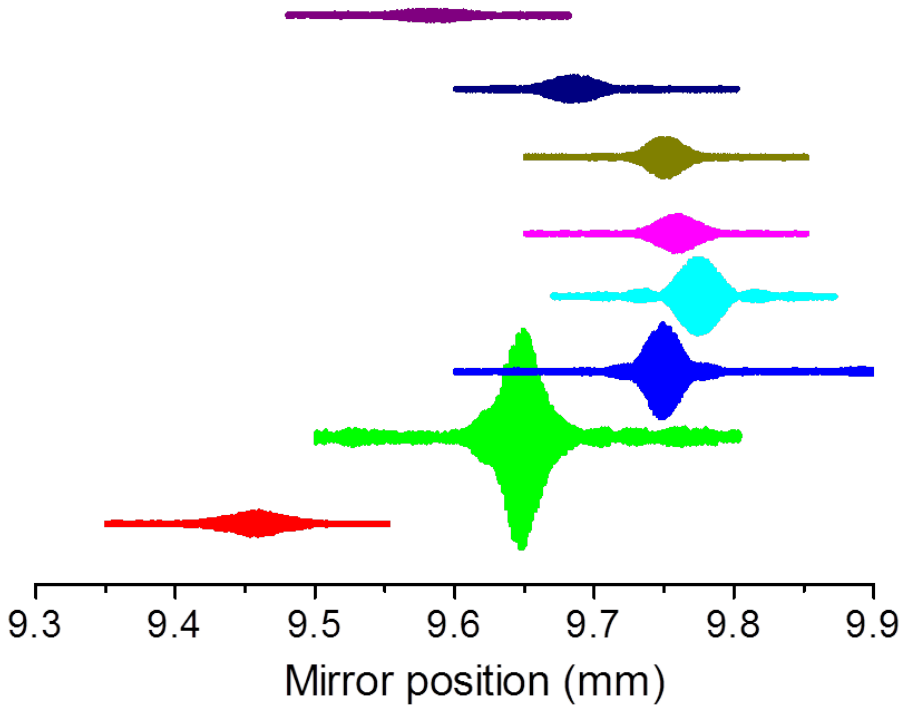

Fig. 1-10: Typical interferograms for wavelengths of 600 nm to 900 nm, from bottom to top (in different colours), recorded when measuring the dispersion of a tested fibre. It can be seen that the peak positions of the fringes change with wavelength.

beams from two arms have the same group delay and overlap each other, a clear interference fringe can be seen from the detector. As different wavelengths have different group delays in the tested fibre, the corresponding mirror positions where interference fringe appears are then also different. This constructs a relationship between the group delay information of the tested fibre and the mirror positions. The latter is easy to measure in experiment. It should be noted that it's the variation of the mirror position which is needed for the calculation of dispersion, not the absolute position value. Fig. 1-10 is a typical plot showing the interference pattern versus mirror position for different wavelengths. In practice, how many wavelengths should be measured and how close they are depend on the dispersion profile of the fibre to be measured and wavelength range of interest.

From the relationship between the group delay in the tested fibre and mirror positions, one can get [46]

$$\frac{d(Ln_g)}{d\lambda} = 2\frac{dx}{d\lambda}, \tag{1.14}$$

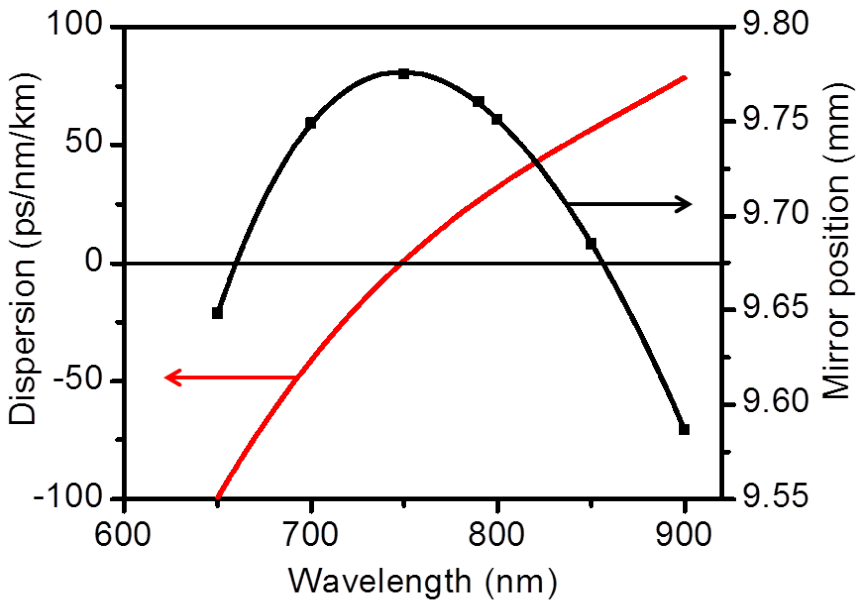

Fig. 1-11: The fringe peak positions which are extracted from Fig. 1-10 (black squares) and its polynomial fit (black solid curve). The dispersion curve (red) is also shown, which calculated from the the first-order derivative of $x(\lambda)$.

where L is the length of fibre under test and x is the mirror position corresponding to fringe peak at different wavelengths. The factor of 2 accounts for the double optical path change of $2\Delta x$ due to a mirror movement of Δx.

The dispersion parameter D can be rewritten as

$$D = \frac{d\beta_1}{d\lambda} = \frac{1}{c}\frac{dn_g}{d\lambda} \tag{1.15}$$

Combining Eqs.(1.14) and (1.15) yields

$$D = \frac{2}{cL}\frac{dx}{d\lambda} \tag{1.16}$$

The fringe position information is extracted from Fig. 1-10 and replotted versus wavelength in Fig. 1-11. In order to calculate D, the data is post-processed by a polynomial fit method to get a function $x(\lambda)$. According to Eq.(1.16), D is obtained by taking the first-order derivative of $x(\lambda)$, which is also shown in Fig. 1-11. For this particular PCF, the ZDW for the fundamental mode is 749 nm.

1.6 Fabrication of PCFs

One of the most important pieces/equipment for fabricating fibres is the drawing tower. Depending on different applications and requirements, the tower's design and properties actually are quite different. However, the main components of a draw tower are similar, and are shown in Fig. 1-12. A preform is heated up to about 2000°C in the furnace and drawn to fibre by drawing it out at a faster speed than it is fed in.

For PCF fabrication, the procedure is more complicated. There are a few ways for making a PCF. Among them, the stack and draw method is the most common way for making high quality PCFs [2]. It normally involves four stages: capillary drawing, stack making, cane drawing and finally fibre drawing, which is shown in Fig. 1-13.

In the first stage, capillaries and rods with desired diameters, normally 1-2 mm, are drawn from fused silica tubes and large solid rods. The second stage is to stack the capillaries and rods by hand to build a scale-up version of the final fibre, called a stack, about 2 cm in diameter. For solid-core PCFs, the central element of the structure is a rod, which forms the core. For a hollow core PCF, the core region is created by simply removing few rings of the central capillaries. This stack is then inserted into a jacket tube to form a preform. Fibre will be drawn from this preform by a two-step process, which is shown in the third and fourth stages of Fig. 1-13. In the third stage canes with diameter of several mm are drawn from the preform (scaling it down to a smaller size). In the final stage, the cane is put into a jacket tube and drawn to fibres.

The way described above involves drawing a stack to a cane and then a cane to a fibre, which can be called two-step fibre drawing process. It is possible to draw the stack to a fibre directly, which is one-step fibre drawing process. However, the two-step fibre drawing process is normally adopted for PCF fabrication as it has many advantages. Firstly, it makes the fibre design easier as some fibres cannot be made by a one-step fibre drawing process in practice. For example, for easy of handling, the diameter of capillaries and rods need to be more than 1 mm. If the core size designed for a final fibre is around 2 μm, the value commonly found in highly nonlinear PCFs, this means that a direct draw-down ratio of more than 500 is needed for one-step fibre drawing. For a final fibre with diameter of 125 μm, the stack need to be built would have a diameter of more than 6.25 cm. Furnaces with element bigger than this are not easily available to researchers

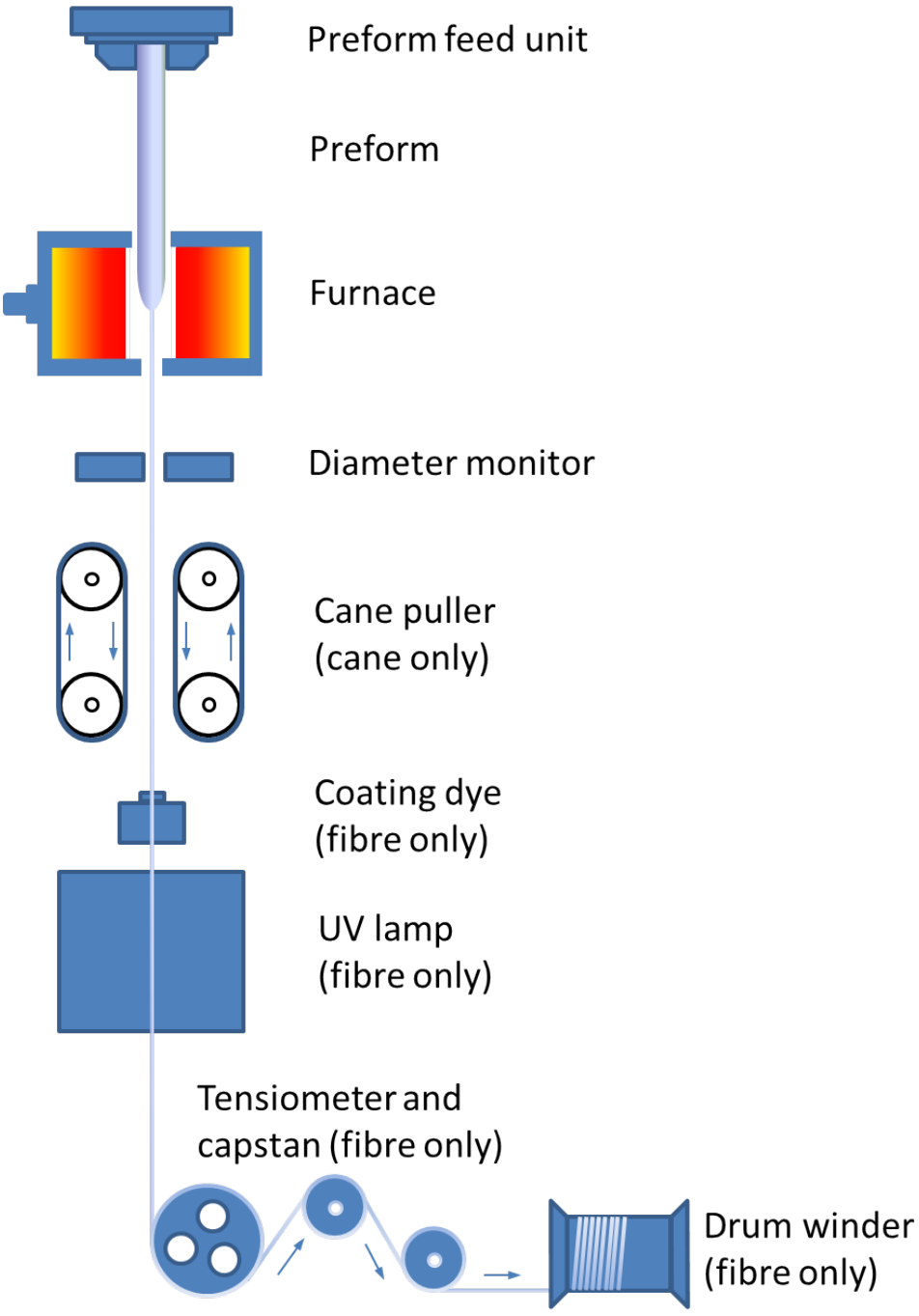

Fig. 1-12: Schematic diagram of a fibre drawing tower.

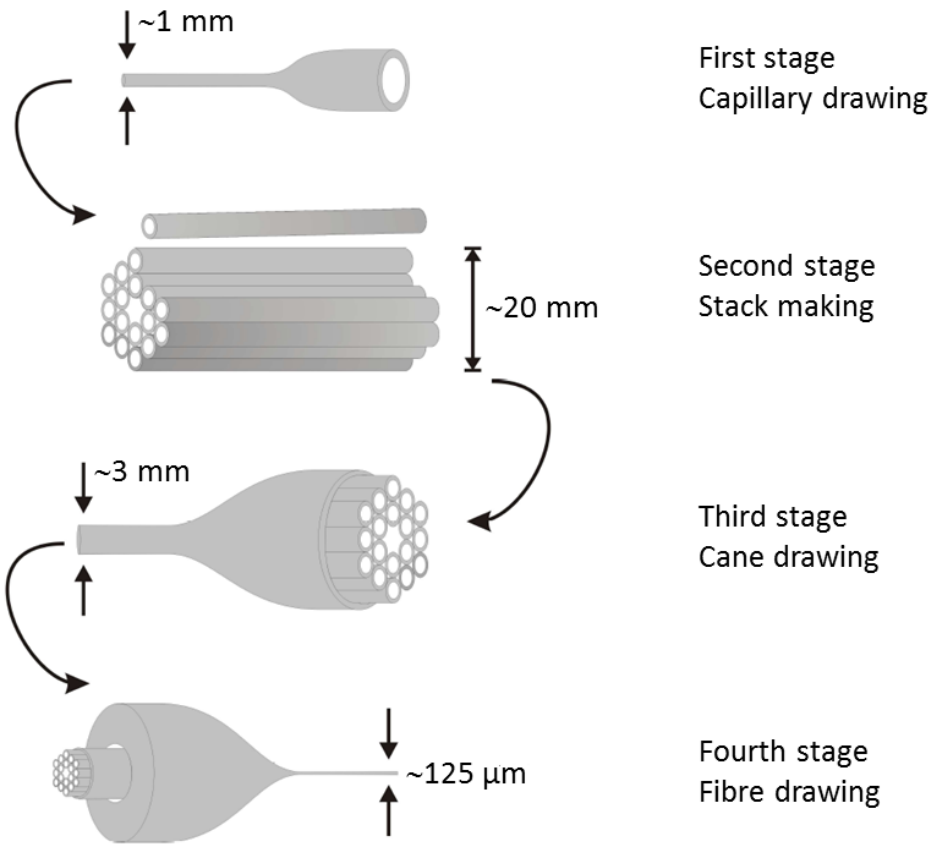

Fig. 1-13: Schematic diagram shows the procedures for fabrication of PCFs [47].

in academia. This means that the stack would be too large for the furnace if the fibre drawing process without a cane stage. Secondly, the cane provides a useful and convenient intermediate platform for more control over fibre structure. Pressure and vacuum can be used to maintain, inflate and collapse the holes to get more versatile structures. Finally, the two-step fibre drawing process helps control the hole pattern in a PCF in a way which minimises the deformation during fibre drawing process. Although capillaries are normally drawn under the same condition, some variation still exists between them. Another source of variation arises from the way how to build a stack. The holes in the innermost and outermost ring of the hexagonal array feel different forces compared with the rest of the structure and deform when the preform is drawn to fibre. As pressurisation is normally used for PCF fabrication, the difference between holes will be exaggerated. The two-step fibre drawing process allows the fabricator to apply a greater stress at the wide end of the glass body for a given stress at the narrow end, the latter being limited by the tensile strength of the glass [48].

1.7 Nonlinearity in optical fibres

Although silica, which optical fibres are made from, does not have a high nonlinear response and hence not a highly nonlinear material, the geometrical structure (the mode field diameter can be in the order of microns) and the long interaction length allow nonlinear effects to be enhanced. In this section we consider the nonlinear effects in fibres which are crucial for understanding the experimental results presented later. It is not intended to give a comprehensive description of all optical nonlinearities. The main purpose is to build up basic background knowledge for the phenomena described in Chapters 6 and 7. There are a lot of prominent textbooks available in this field for detailed further reading, such as refs. [24] and [37].

1.7.1 Quantifying nonlinearity

Nonlinearity in opitcal fibres can be quantified in a number of ways. One important way is to use the nonlinear parameter known as γ, which is the phase change per unit length per unit power and expressed in the form

$$\gamma = \frac{n_2 \omega_0}{c A_{\text{eff}}}, \tag{1.17}$$

where n_2 is the nonlinear index coefficient and A_{eff} is the effective mode area in a fibre. For a mode with electric field distribution of $E(x, y)$, A_{eff} is defined as

$$A_{\text{eff}} = \frac{(\int\int_{-\infty}^{\infty} |E(x,y)|^2 dxdy)^2}{\int\int_{-\infty}^{\infty} |E(x,y)|^4 dxdy} \tag{1.18}$$

There is another parameter for defining the propagation length over which nonlinear effects become significant: nonlinear length L_{NL}

$$L_{\text{NL}} = \frac{1}{\gamma P_0}, \tag{1.19}$$

where P_0 is the peak power of the input pulse. We can also defines the propagation length L_{D} over which dispersion effects become important

$$L_D = \frac{T_0^2}{|\beta_2|}, \tag{1.20}$$

where T_0 is the input pulse width. The comparison between dispersion length L_{D} and nonlinear length L_{NL} provides information as to whether dispersive or nonlinear effects are dominant for pulse evolution in a fibre.

1.7.2 Self-phase modulation

Self-phase modulation (SPM) originates from the intensity dependence of the refractive index, which is one of the nonlinear phenomena governed by $\chi^{(3)}$. $\chi^{(3)}$ is the 3rd order susceptibility of silica, which gives rise to lots of nonlinear effects in optical fibres. The intensity dependence of the refractive index causes an intensity dependent phase shift to be experienced by an optical pulse during its propagation in optical fibres. As a result of SPM, one can see a spectral chirp develop across the pulse but the temporal shape is kept unchanged. If we neglect dispersive effects and initial chirp, SPM always induces spectral broadening. At the leading edge of a pulse, new red-shifted frequencies will be generated, while new blue-shifted frequencies emerge at the trailing edge of the pulse. The change of phase and frequency depends considerably on the shape and intensity of the input pulse. However, in some cases dispersive effects cannot be neglected, which can lead to some interesting phenomena, like forming a soliton.

1.7.3 Soliton effects

As discussed before, dispersion causes different frequency components to travel at different speeds and hence broaden a pulse. If the pulse propagates in the normal dispersion regime, the broadening rate will be enhanced. However, the situation becomes totally different for a pulse propagating in the anomalous dispersion region of a fibre. The interplay between anomalous GVD and SPM will lead to a stabilised waveform known as an optical soliton [37]. The word soliton essentially means a localised nonlinear structure which will propagate undistorted over a long length.

It is useful to define a parameter based on L_{D} and L_{NL}, with the form

$$N^2 = \frac{L_{\mathrm{D}}}{L_{\mathrm{NL}}} = \frac{\gamma P_0 T_0^2}{|\beta_2|}. \tag{1.21}$$

This parameter N defines the order of a soliton and is quite important for understanding the physics behind it. For the case of the fundamental soliton, $N = 1$, which means that both SPM and GVD are equally important during pulse propagation. Once the soliton is formed, the pulse's temporal and spectral properties are unchanging with propagation distance along the fibre. This phenomenon can be understood by an inspection of the chirps caused by SPM and GVD. In the anomalous regime where a soliton forms, the dispersion-induced chirp is negative while the SPM-induced chirp is positive. The contributions of these two can compensate for each other and maintain a chirp-free environment in the case of $N = 1$ [37]. It must be noted that it is not necessary for the input pulse has a perfect sech shape or exactly $N = 1$. During its propagation along the fibre, the pulse can adjust itself to become an soliton. Fig. 1-14 (a) shows the spectral and temporal evolution of the fundamental siliton over 2 soliton periods. The soliton period Z_{sol} has the form

$$Z_{\mathrm{sol}} = \frac{\pi}{2} L_{\mathrm{D}}. \tag{1.22}$$

The situation is different for a higher-order soliton, in which N is larger than 1. The spectral and temporal dynamics of a $N = 3$ higher-order soliton are shown in Fig. 1-14(b). The parameters used in the calculation for this higher-order soliton are the same as those for the fundamental soliton except for the peak power, which is necessary for changing the soliton order. It can be seen from Fig. 1-14(b), that at the beginning SPM dominates the whole process and the pulse is broadened in frequency and compressed in time. However, as the pulse

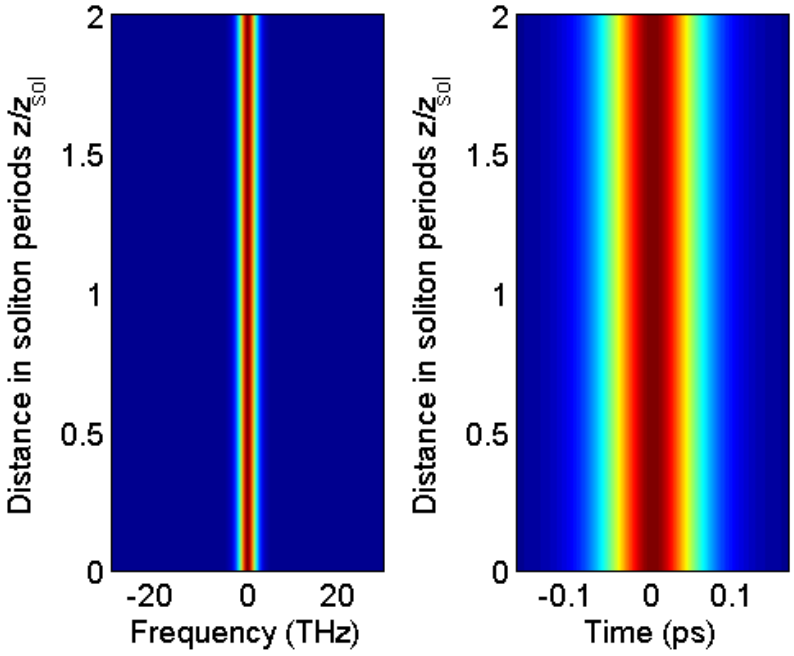

(a)

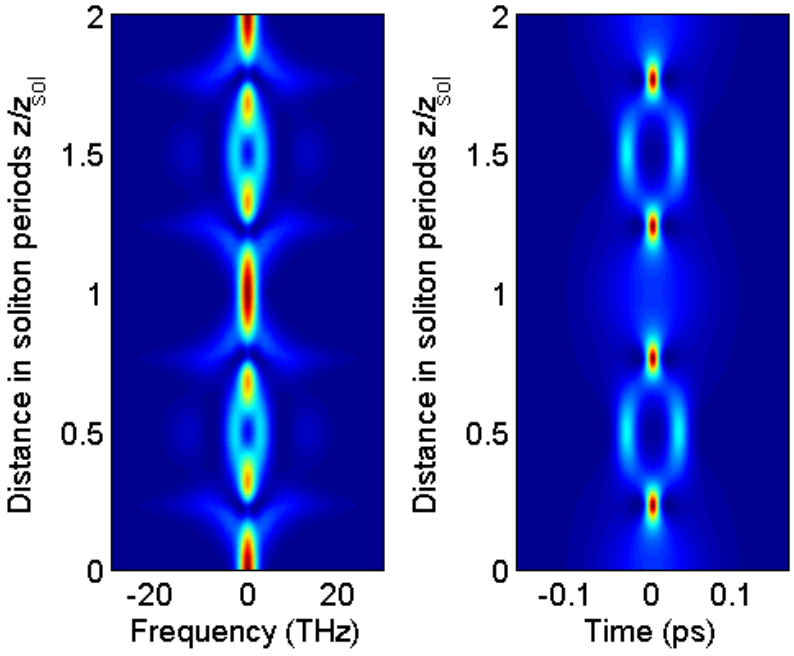

(b)

Fig. 1-14: Spectral (relative frequency) and temporal evolution for (a) N=1 and (b) N=3 solitons over 2 soliton periods. The intensity colour maps are plotted on a linear scale. Only the effects of β_2 and SPM are considered when plotting these figures [49].

becomes narrow (in time) and broad (in frequency), the GVD plays a more and more important role, after this SPM dominates again. In Fig. 1-14 we can see these periodic properties. The soliton periods Z_{sol} has a clear meaning here.

However, this kind of ideal periodic soliton, in practice, is not stable to even slight perturbations. The source of perturbations can be either from the fibre's linear properties, such as higher-order dispersion, or nonliear properties, such as intrapulse Raman scattering. These higher-order solitons, due to perturbations, are split into a train of fundamental solitons, a process known as soliton fission [50, 51]. The generated fundamental solitons undergo further dispersive and nonlinear propagation. The soliton fission and related soliton effects are crucial for the SC generation in PCFs and have been intensively investigated in the last 10 years.

1.7.4 Four wave mixing and modulation instability

Four wave mixing (FWM) is another third order nonlinear effect governed by $\chi^{(3)}$ and an important process for new wavelength generation. Basically, it means that two photons at frequencies ω_1 and ω_2 are annihilated to generate two new photons at frequencies ω_3 and ω_4 with a relationship of $\omega_3 + \omega_4 = \omega_1 + \omega_2$. For the case where ω_1 doesn't equal ω_2, this is called non-degenerate FWM. In optical fibres, the special case refereed to as degenerate FWM is more familiar and takes the forms of $\omega_1 = \omega_2$ and $\Omega = \omega_1 - \omega_3 = \omega_4 - \omega_1$ (assuming $\omega_4 > \omega_3$), where Ω is the frequency shift from pump ω_1. ω_3 is known as the idler with a down shifted frequency while ω_4 is known as the signal with an up shifted frequency.

As FWM is a parametric process, it is useful to define a phase mismatch term κ as

$$\kappa = 2\gamma P_0 + \Delta\beta \tag{1.23}$$

where $2\gamma P_0$ represents phase mismatching caused by nonlinear effects and $\Delta\beta$ comes from dispersion and can be expressed as

$$\begin{aligned} \Delta\beta &= \beta(\omega_3) + \beta(\omega_4) - 2\beta(\omega_1) \\ &= \beta(\omega_1 - \Omega) + \beta(\omega_1 + \Omega) - 2\beta(\omega_1) \end{aligned} \tag{1.24}$$

By applying the Taylor expansion of β obtained form Eq. (1.8), Eq. (1.24) can be expressed as

$$\Delta\beta = 2\sum_{n=1}^{\infty} [\beta_{2n}/(2n)!]\,\Omega^{2n} \tag{1.25}$$

Note that only even order dispersion coefficients contribute to $\Delta\beta$, as the odd terms cancel out during the calculation. For an efficient FWM process to occur the phase matching conditions need to be fulfilled along with the energy conversation. These two conditions can be expressed as

$$\kappa = 2\gamma P_0 + \Delta\beta = 0 \tag{1.26}$$

and

$$2\omega_1 = \omega_3 + \omega_4 \tag{1.27}$$

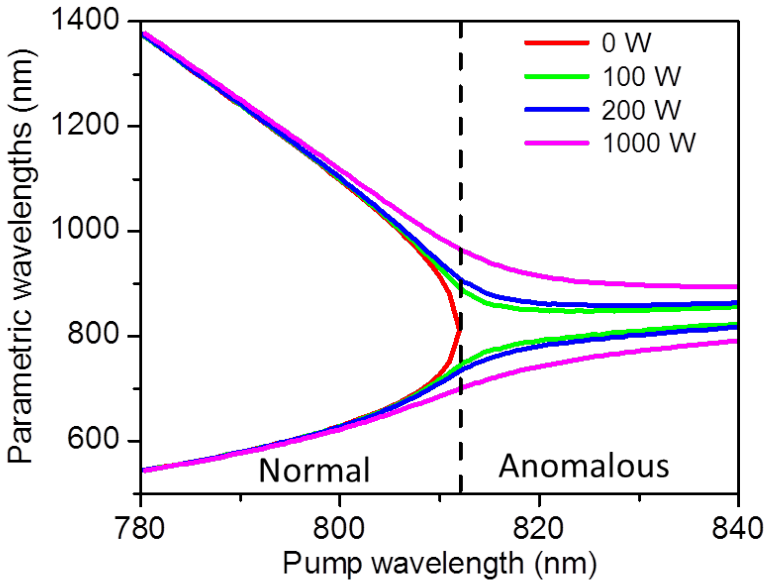

Fig. 1-15: Typical FWM phase matching diagram for the fundamental mode of a PCF with a ZDW at 812 nm.

Eqs.(1.27) and (1.26) then can be used to calculate the phase matching diagram for different pump wavelengths and pump powers.

In practice, the way to deal with $\Delta\beta$ is different depending on how the information of β is available. For example, by using the full vector numerical model based on the supercell plane-wave method [52], we can get the β values directly and then these values can be applied to (1.26). For the case of disperion measured

from an experiment, only the β_2 is known to us. However, the dispersive curve can be expanded as a Taylor series with dispersion coefficients β_{n}. Then (1.25) can be used for the phasematching calculation [53].

A typical FWM phase matching diagram for the fundamental mode of a PCF is shown in Fig. 1-15. This mode has a ZDW at a wavelength of 812 nm and the pump wavelengths cover both normal and anomalous dispersion regions. Note that Fig. 1-15 is shown in wavelength not frequency just for convenience. There are several interesting things that can be observed from this figure. Firstly, signal and idler wavelengths are well separated from the pump wavelength in the normal dispersion regime, while in the anomalous regime FWM peaks appear near to the pump wavelength. Secondly, the positions of the signal and idler wavelengths largely depend on the pump powers in the anomalous region, which means $2\gamma P_0$ plays a very important role for phase matching. In contrast, in the normal dispersion region, this dependence becomes very weak as the pump wavelength moves away from the ZDW. Interestingly, we can see phase matched signal and idler peaks even when $P_0 = 0$ W in the normal dispersion region, suggesting that phase matching can be achieved by the contribution from dispersion alone, although there is no gain for these wavelengths to grow as $P_0 = 0$ W. The parametric gain g can be expressed as [49]

$$g = \left[(\gamma P_0)^2 - (\kappa/2)^2\right]^{1/2} \tag{1.28}$$

This gain is the source for the initial growth and amplification of the sidebands (signal and idler) of the FWM process. Although the peak gains for both normal and anomalous dispersion regions are the same (γP_0 when the phase mismatching is zero), the gain bandwidth for the anomalous region is relatively broad while that for the normal region is very narrow [49].

The sidebands generated by FWM in frequency will lead to a temporal modulation to the input pump wave and break up it. This causes stable CW light to become unstable, a process referred to as modulation instability (MI). It is well known that FWM and MI actually describe the same physical phenomenon but in different domains [37, 49]. MI is a time domain description while FWM is based on the frequency domain. The name "MI" is widely used, especially for describing phenomenon in the anomalous dispersion region.

It is noted that all the discussion here are based on the quasi-CW assumption, which ignores the group velocity difference between different wavelengths. In reality, the pulse walk off effect should be considered when short pulses are used,

as a temporal overlap is essential for effective FWM to happen.

1.7.5 Raman effects

The aforementioned nonlinear effects are elastic, which means that there is no energy exchange between the input optical field and silica. Optical fibres play a passive role. However, there exists stimulated inelastic scattering processes, like SRS, in which optical field transfers part of its energy to the optical fibre and in this way optical fibres play an active role [37].

In the process of Raman scattering, a pump photon is down-converted into a lower frequency Stokes photon, and a phonon associated with a vibrational mode of the medium. The pump photon can be scattered to a higher frequency if it can combine an available phonon. The higher frequency component is called the anti-Stokes. This up-conversion process is very rare as it requires both phase matching and energy conservation. However, in some cases, especially under the influence of FWM, both Stokes and anti-Stokes can be observed in experiment [54].

Due to the amorphous properties of silica, the Raman gain g_{R} provided by Raman scattering in optical fibres extends over a large frequency range (up to 40 THz) with a broad peak located around 13 THz [37]. This is quite useful for SC generation but also reduces the coherence of the spectrum generated. If a short pulse is involved, like a soliton, the SRS can happen within it, a process called intrapulse Raman scattering. The low frequency components of a soliton pulse can be amplified at the cost of the high frequency components. The net effect of this is, that the soliton continuously moves to longer wavelength, is called the soliton self-frequency shift.

1.7.6 Dispersive wave generation

The perturbation from higher order dispersion can cause a soliton to transfer energy to a narrow band resonance, a process called dispersive wave generation. It is a very important mechanism for generation of new wavelenghs in the normal dispersion region and can be considered as a Cherenkov radiation process in the optical field [55]. A phase matching condition involving the linear phase of the dispersive wave and linear and nonlinear phase of the soliton is used for determining the position of this resonance [49, 55].

Different solitons generate different dispersive waves at different wavelengths. All of these wavelengths contribute to the spectrum broadening in the normal

dispersion region, usually the blue region of a SC spectrum. However, this dispersive wave emission cannot account for the continuous blue shift of the short-wavelength edge of a SC as the amplitude of the resonance radiation decays exponentially as solitons move to longer wavelengths. The interplay between solitons and dispersive waves, however, causes this phenomenon. Generally speaking, the dispersive waves are trapped by the decelerating solitons [56, 57]. As the solitons are red shifted to longer wavelength due to Raman effects, the dispersive waves continuously shift to the short wavelength side (blue shifted). This process won't stop until the solitons cannot exist due to high loss or moving to the normal dispersion region.

1.7.7 Supercontinuum generation

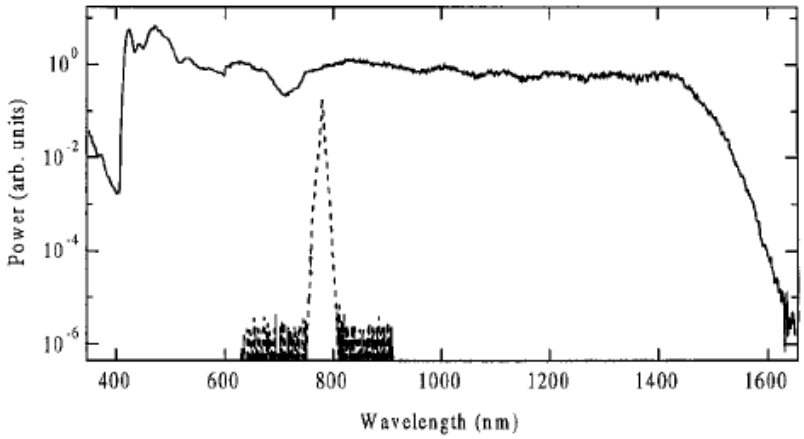

Fig. 1-16: Typical supercontinuum spectrum generated in a photonic crystal fibre. The dashed curve shows the spectrum of the initial 100 fs pulse. From Ref. [58].

Supercontinuum generation is a phenomenon where a narrow-band incident pulse undergoes extreme nonlinear spectral broadening to yield a broadband spectrally continuous output [49]. Although SC was first discovered by Alfano and Shapiro [59] in a bulk glass, and has since been investigated in a wide variety of nonlinear media, the advent of photonic crystal fibres allowed this field to take off. The typical SC spectrum is shown in Fig. 1-16, extending from the violet to the infrared. This SC was generated by propagating pulses of 100 fs duration and kilowatt peak powers through a PCF near the zero-dispersion wavelength [58].

The detailed physical mechanisms behind supercontinuum generation are very complex, and largely depend on the parameters of the fibre and pump. Generally

speaking, we can divide SC generation into two categories: SC generation pumped by femtosecond pluses and SC generation from longer pulses (from picosecond to CW). In the femtosecond regime, the main mechanisms are soliton fission, dispersive wave generation and Raman effects. In the long pulse regime, four-wave mixing and modulation instability play a very important role to break up the long pulse and initialise the spectral broadening process. The resulting short pulses evolve into a train of fundamental optical solitons. Raman effects and dispersive wave generation are also important and further broaden the spectrum.

1.8 Summary

This chapter gives a comprehensive review about the fundamentals of optical fibres, which is important for the research described in this thesis. Although PCFs are quite different from conventional fibres, there exist lots of common properties between them. The loss, modes and dispersion properties are the basics of an optical fibre, all of which are summarised here. The fabrication procedure of optical fibres, especially PCFs, is also briefly discussed in this chapter. This is important for the work reported in Chapter 3. Nonlinear fibre optics has a long history and the advent of PCFs has brought this research area to a new level. In this chapter, some basic concepts of nonlinearity are summaried for the understanding of Chapters 6 and 7.

Chapter 2

Fibre transitions and PCF structure modifications

In this chapter, we consider post-processing techniques, which will be used for the experiments described later. In Section 2.1, the taper rig and how to make adiabatic transitions are explained. Almost all post-processing processes carried out in this thesis are related to structure changes of a PCF and normally cause losses. However the loss can be extremely low if adiabaticity is satisfied. In Section 2.2, cladding modification techniques are discussed in detail.

2.1 Optical fibre transitions

2.1.1 Fibre tapering and the taper rig

Fibre tapering is an important and effective post-processing technique that can vary the nature of a fibre waveguide remarkably. This technique has been inten-

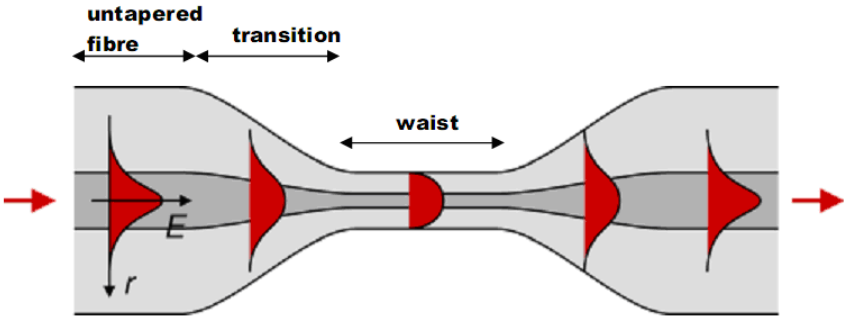

Fig. 2-1: A fibre taper and light propagation along it (From Ref. [60]).

sively used for conventional fibres, making optical components such as directional couplers [61] and beam expanders [62].

Technically speaking, an optical taper is made by stretching a heated fibre. In this way, a structure with a narrow stretched filament (called the taper waist), each end of which is connected to an untreated fibre by a conical tapered section (called the taper transition), can be formed, as shown in Fig. 2-1.

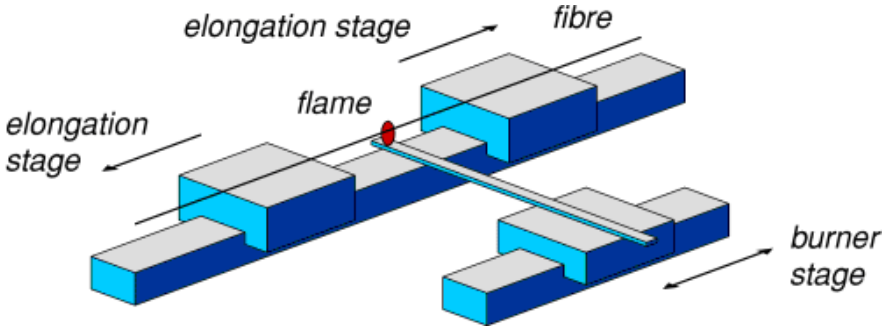

Fig. 2-2: Taper rig setup (From Ref. [60]).

Experimentally, a taper rig is used to obtain the structures needed. The home-made taper rig at the University of Bath is easy to control and very versatile, based on a modification of the "flame brush" technique [9]. As shown in Fig. 2-2, it consists of three motorised stages, two of them used to stretch the fibre and the third one for moving a burner that supports a small flame. The flame is produced by burning oxygen and butane. Through changing of the amount and ratio of these two gases, one can control the temperature and the size of the flame. The movement of these stages are controlled through a computer. The degree of accuracy of the designed structure along the fibre is of the order of a few millimetres, which is mainly determined by the size of flame (If the oxy-butane flame is replaced by a carbon-dioxide laser beam, the accuracy can be enhanced to several hundred micrometres [11]). Using this setup, high performance optical tapers with lengths of up to 20 cm and diameters of down to 100 nm can be obtained [10].

2.1.2 Adiabatic transitions

We need to keep the loss of our devices as low as possible. In this case, we need to consider the light propagation in a taper and understand adiabatic transitions.

Transitions link the fibre taper waist to the unprocessed fibre ends. Furthermore, the function of a transition is to couple light from the unprocessed fibre,

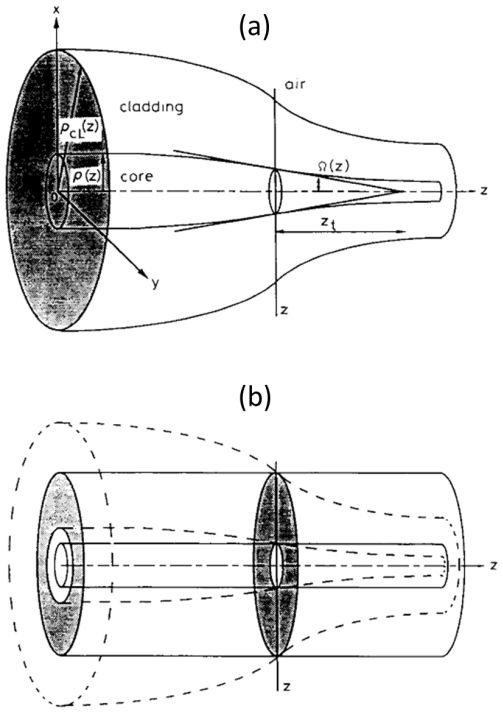

Fig. 2-3: Local mode concept (From Ref. [63]).

usually in the fundamental mode, to the taper waist with a low loss, keeping the same mode as before, and then couple it back to the untreated fibre. Because of the departure from translation invariance, transitions can profoundly change the field distribution of a mode. As light propagates along the optical taper, the field distribution is unable to change rapidly enough to adjust itself with the variation of the structure if the transition is not well designed [63]. These dramatic structural changes in the transitions cause light to be coupled to higher-order modes and lost. The concept of a mode mentioned before must be generalised to that of a local mode in this case. The local mode at point z is defined as the mode of a uniform fibre with the same dimension at that position. This is shown schematically in Fig. 2-3 (b) [7, 63]. Each point along the transition has a corresponding propagation constant $\beta(z)$.

Imaging that light travels from one position to another in a transition. There will be some light coupling from one local mode to another, which is referred to as "local mode coupling" [7]. However, if the transition is gradual enough, in other words, the taper angle is small enough everywhere along it, the local mode conserves power as it propagates and the coupling from this local mode is negligible. In this way, the local mode evolves adiabatically into the neighbouring local

mode of the next position. Mathematically, there exists a length-scale criterion based on the comparison of the local taper length scale z_{t} with the beat length L_{B} between two possible closest modes [63]. If $z_{\mathrm{t}} >> L_{\mathrm{B}}$ everywhere along the taper, there is nearly no mode coupling and light propagates adiabatically along it with negligible loss. This corresponds to a taper angle $\theta(z)$ much smaller than a local delineating angle $\Omega(z)$(where $z_{\mathrm{t}} = L_{\mathrm{B}}$, Fig. 2-3 (a)) [63]:

$$\theta(z) << \Omega(z) = (\rho(z)/2\pi)(\beta_1 - \beta_2) \tag{2.1}$$

where the $\rho(z)$ is the core radius. If the light propagates in a mode with a propagation constant of β_1, then β_2 is the propagation constant of the mode that the first mode is most likely to couple into.

Eq.(2.1) gives us a reference for determining the condition of adiabatic transitions. Experimentally, a several-centimetre long transition is normally enough for connecting an untreated fibre (125 μm) to its waist (several microns).

The above discussion is about how to achieve an adiabatic transition. In certain situations, another type of extreme transition, an abrupt transition, needs to be considered. This transition can mean lots of mode coupling. The theory for analysing it reduces to a mode excitation problem, which can be found in many optical waveguide textbooks [7].

2.2 PCF structure modifications

The methods of tapering applied to conventional fibres for structure changes can also be applied to PCFs. Furthermore, the air holes in PCFs' cladding provide another degree of freedom for modification. A lot of interesting devices will be possible if we can make the holes get bigger or smaller. If a technique can change the structure in any way which one wants, for example, making some holes become bigger, while others become smaller, the potential of PCFs will increase dramatically. All of these are discussed in this section.

2.2.1 Surface tension theory

From the theory of surface tension, it is known that the excess hydrostatic pressure p_{st} required to balance collapse for a cylindrical hole in a liquid is [13, 64]

$$p_{\mathrm{st}} = 2\gamma_{\mathrm{st}}/d \tag{2.2}$$

where γ_{st} is the surface tension of the liquid and d is the diameter of the hole. Whether the holes expand or shrink depends on the difference between internal gas pressure p_o and p_{st}. If $p_o > p_{st}$, the hole will expand, while in the opposite situation $p_o < p_{st}$, the hole will shrink. As the surface tension γ_{st} changes little with temperature in silica glass [13, 65], the changing tendency of a hole in a PCF, say shrinking or expanding, depends only on the internal pressure and the diameter of that hole. Other variables, like the temperature (which affects the viscosity) of silica glass and the magnitude of pressure difference $p_o - p_{st}$ just determine the changing speed of this tendency [13].

Although there is some contrary evidence about the value of γ_{st} for silica glass recently [34], here we still adopt the commonly-quoted value, which means $\gamma_{st} = 0.3$ J/m^2 [65], and Eq. (2.2) can be rewritten in terms of pressure in bar and hole diameter in μm [13]:

$$p_{st}(\text{bar}) = 6/d(\mu\text{m}) \tag{2.3}$$

Experimentally, there is another parameter need to be considered: gas flow speed in holes. This is very important for those time consuming experiments, which may carried out in a long piece of PCFs with small holes. Typically, the $1/e$ time to fill a sealed hole to (absolute) pressure p_H is [66]:

$$\tau = \frac{128\eta L^2}{\pi^2 d^2 p_H} \tag{2.4}$$

where $\eta = 1.6 \times 10^{-5}$ Pa s for nitrogen, L is the length of a PCF. For a 1 metre long PCF with the hole diameter of 1 μm, filled by dry nitrogen to $p_H = 2$ bar (1 bar over ambient), the typical filling time is about 20 minutes.

2.2.2 Differential pressurisation techniques

According to the surface tension theory given in Section 2.2.1, the changing tendency of holes in PCFs can be expanding, shrinking or keeping their original size. However, in order to achieve changes in multi-directions at the same time, one need to make sure the pressure in different holes is not the same. This means some holes are under higher pressure p_1, while other holes are under a relative lower pressure condition p_2. This can be achieved by the differential pressurisation techniques, which include hole plug process, differential pressurisation and heating treatment.

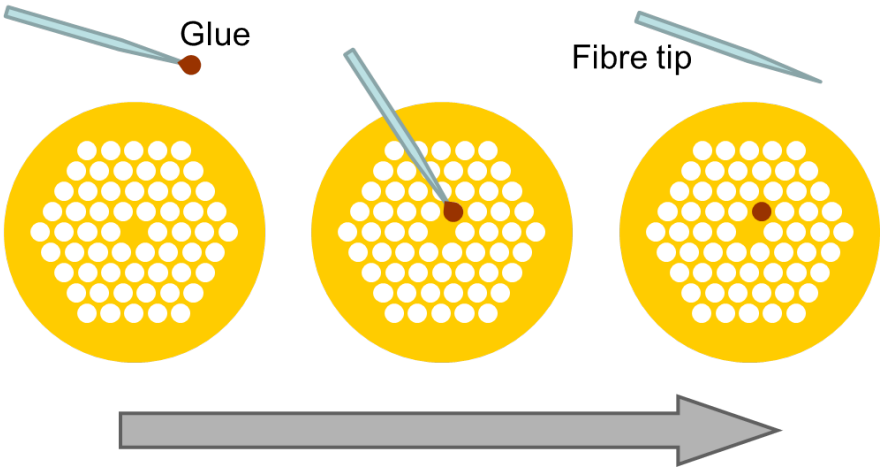

Fig. 2-4: Schematic for hole plug process. Silica areas are shown in gold, while holes are shown in white.

Hole plug process

The hole plug process is intended to create a platform for selectively applying pressure [39, 67]. We selectively plug some holes with glue while leaving others open, which is schematically shown in Fig. 2-4. These plugged holes remain at atmospheric pressure, while a different pressure can be applied to other open holes. When treated on the taper rig, these two types of holes behave expand or contract differently and form desired structures.

A Nikon microscope (Eclipse LV100) with suitable objectives is used for the purpose of hole plug. Objectives of 5X and 50X powers are those used frequently. The whole setup is shown in Fig. 2-5. The main equipment is the Nikon microscope, while to the left of it there is an x-y-z stage for holding and moving a small fibre tip. This optical taper (the fibre tip) with a waist diameter of about 1 μm is made from conventional fibre (SMF 28) using the taper rig.

We plug the holes with a UV-sensitive glue which can be cured after exposure to a UV light. The difficulty of this experiment is about how to distribute the glue in the holes of the fibre end as designed. One needs to make sure only target holes have been plugged without contaminating any other holes. The size of the holes in PCFs is quite small (some of them may be less than 2 microns in diameter), therefore a suitable fibre tip is an important tool for this purpose.

The target fibre which needs to be glued and another short piece of SMF 28 fibre used for storing glue on its end face (called glue tank) are stationed in parallel on one side of a small metal bar, as shown in Fig. 2-5(right). First, we move the small tip to touch the glue tank fibre to pick up a small amount of glue.

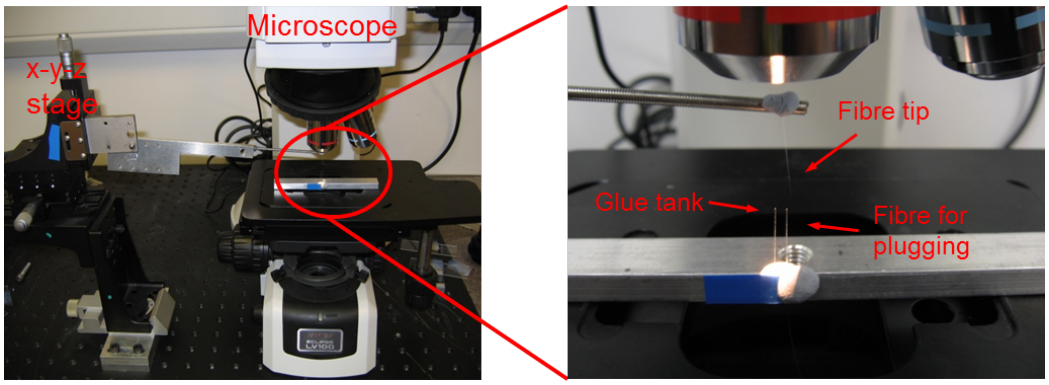

Fig. 2-5: Photographs about the experimental setup for hole plug.

Second, the x-y-z stage is used to move this tip to the target fibre end. By moving the tip to the target fibre hole, the glue can be placed in that hole, Fig. 2-4. All these processes are conducted under the microscope. We change objective lenses frequently to meet the requirement for precise control. Repeating this process, we can plug another hole and so on. Using this way, we can make any plugged hole pattern. For example, a fibre with four holes plugged along a line through the core is shown in Fig. 2-6 (b), while the original fibre is shown in Fig. 2-6 (a). Finally, the processed fibre end need to be exposed to UV light for a few minutes to solidify the glue.

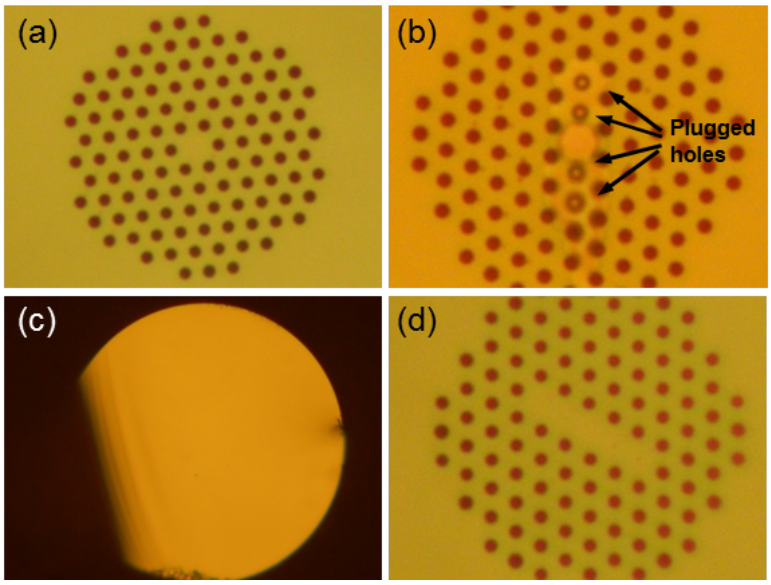

Fig. 2-6: Optical micrographs of the original fibre (a), four holes plugged in one end (b), sealed endface in the other end (c), and the processed structure (d). Not the same scale.

Although the idea of hole plug technique is very simple, there are many challenges during experiment. For fibres with very small holes (less than 2 microns), especially those holes that are very close, it is extremely difficult to avoid contaminating other holes which you do not want to be plugged. However, after some practice, one can do it well.

Differential pressurisation and heating treatment

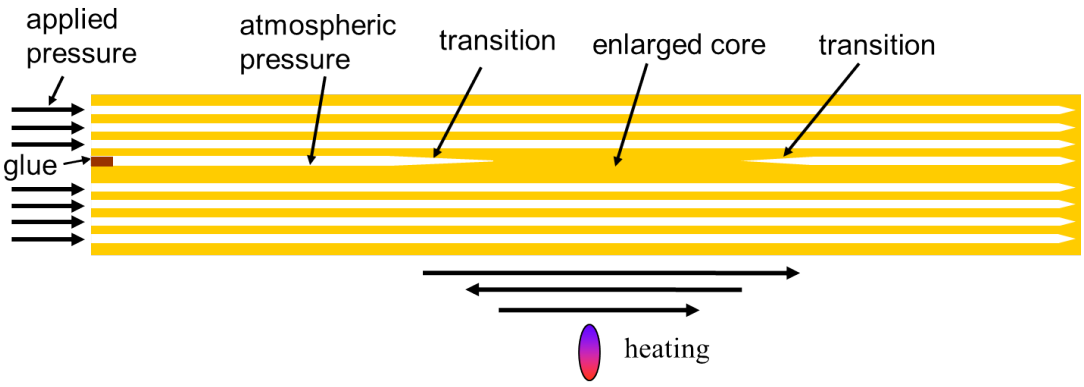

Fig. 2-7: Schematic longitudinal cross section of a PCF under the differential pressurisation and heating process. The left endface of this fibre has been selectively plugged with glue, and the right endface is totally sealed. Silica areas are shown in gold, while holes are shown in white.

After the holes have been plugged, a differential pressurisation and heating process [67] can be applied to achieve desired structure modifications, which is schematically shown in Fig 2-7.

Firstly, the other end face of the fibre is heated by a big flame to collapse all holes (which also can be done with a fusion splicer), as shown at the right side of Fig 2-7.

Secondly, high pressure dry nitrogen is applied to the fibre assisted by a gas cell. The plugged end of the fibre is connected to the gas cell, which is supplied with nitrogen at a pressure of a few bar as determined from Eq. (2.3). The plugged holes can be considered as sealed cavities: nitrogen cannot go inside these holes and the pressure in them remains at atmospheric pressure. The other, open holes, become loaded to the right pressure to balance the effects of surface tension.

Finally, a short length of this fibre is heated on the taper rig. Due to different pressures in different holes, the trend of hole change is different. The plugged holes will collapse under heating. The position and temperature of the flame and

the heating time can be adjusted to control the collapse and get desired variation along the fibre length. Other holes can keep their original size thanks to the pressurised gas. Obviously these holes can be expanded if the applied pressure is even higher.

Following these procedures, the fibre with four holes plugged shown in Fig. 2-6(b) can be post-processed to get the designed structure. Fig. 2-6(c) shows the totally sealed end, which resembles a silica rod. The final cross section of the treated fibre is shown in Fig. 2-6(d). A rectangular core with 5:1 aspect ratio is formed by the collapse of the four plugged holes.

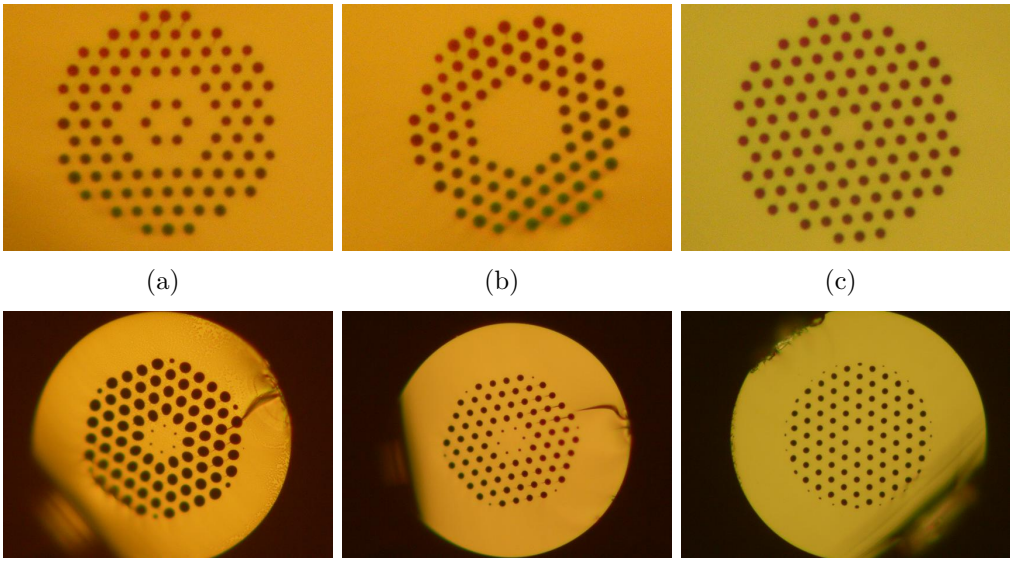

Fig. 2-8: Some possible results. (a-b) are based on the original PCF in (c); (d-e) are based on the original PCF in (f).

Versatility of this technique

The technique described here is very versatile, and some possible results are shown in Fig. 2-8. Almost any kind of change to the structure of the cladding can be achieved easily by following the steps given above. By controlling the flame's movement, we can vary the structure along the fibre length. Furthermore, complex structures can be obtained by repeating these procedures a few times, which will be described in Chapter 5.

2.3 Summary

In this chapter, several post-processing techniques are discussed. The taper rig is an important piece of equipment for the work described subsequently in this thesis. The way how to change to structure of a PCF has been reviewed in detail.

Chapter 3

Hole size prediction and control in the fibre drawing process without knowing the viscosity

We report the first analytical description of the drawing of fibres with holes that does not require knowledge of the viscosity (or temperature) of the glass in the furnace. Instead the effect of viscosity is represented by the fibre draw tension which, unlike viscosity, can readily be measured in practice by the fibre fabricator. A special fibre was made to test our model. It is found that the model matches experiments without recourse to any adjustable fitting parameters. These results give directions as to how hole size can be controlled by varying draw tension, pressure and drawdown ratio, which is important for special fibres, like photonic crystal fibres.

3.1 Introduction

As mentioned in Chapter 1, photonic crystal fibres contain air holes that run along the length of the fibre. The holes give the guided light properties that can be difficult or impossible to obtain in fibres of more conventional design. The fibres are drawn in a furnace from preforms that also contain holes. In contrast to features in ordinary solid fibres, these holes can profoundly change in size (and indeed in shape) relative to the fibre as a whole, under the influence of surface tension, glass viscosity and pressure differences. To produce PCFs of given designs it is therefore important to understand how such parameters affect

the final holes.

Several published treatments of this problem range from detailed numerical studies of complex multi-hole structures to simplified analytical models whose strict validity is limited but which give insight [68–73]. However, these studies suffer from an important drawback from the experimenter's point of view: the results are expressed in terms of the viscosity of the glass in the furnace. Unfortunately the viscosity along the glass body is unknown to the fibre fabricator, not even as a single parameter along a uniform hot-zone length, let alone in its full form as a distribution $\mu(x)$ along the preform/fibre axis x. Thus authors typically make assumptions about the temperature T of the glass and deduce the viscosity from the material's reported $\mu(T)$, or alternatively fit $\mu(x)$ as a free parameter to their experimental data. The most thorough experiments included careful measurements of the temperature distribution $T(x)$ along a preform in the furnace and extrapolated to the process temperature of silica glass, and use of the best available published information for $\mu(T)$ in silica [73].

We show that knowledge of viscosity can be completely eliminated from the analysis, at least in the case of a hole that is isolated from other holes and small compared to the outer diameter of the fibre. Instead we express the hole size in terms of the draw tension F, which is not only knowable but is routinely logged during fibre fabrication. Enough assumptions and approximations are made to render the problem analytical, while still representing the effects of surface tension, pressurisation and arbitrary viscosity profiles. The result is equivalent to Fitt et al's small-hole result [69], but for the first time allows direct comparisons with experiments based entirely on known experimental parameters. Indeed, the only variables relating the final and initial hole sizes are the draw stress, the draw-down ratio and the hole pressure. On the other hand, these three parameters can be used to achieve a desired hole size or hole size difference.

In order to verify our model, a special fibre was designed and fabricated based on the standard stack and draw technique. It has three holes with different sizes. It is found that our modelling results are a good approximation for isolated holes drawn in real fibres by measuring the final diameters of three dissimilar holes. These measurements confirm our key finding, that draw stress in the fibre governs hole size irrespective of how the stress is changed. Furthermore the measured hole sizes match the predictions of our model with no introduction of any adjustable fitting parameters.

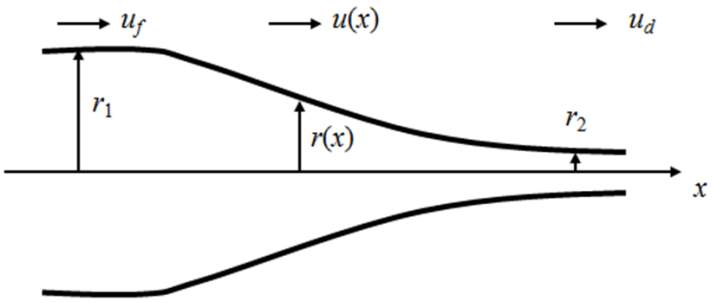

Fig. 3-1: Undeformed drawdown of a cylindrical glass body from preform radius r_1 to fibre radius r_2 via intermediate radius $r(x)$ at position x within the furnace. The preform is fed into the furnace at feed rate u_f and the fibre is drawn out at draw speed u_d.

3.2 Analysis

Previous reports took a general fundamental starting point such as the Navier-Stokes equation of fluid mechanics, and carefully applied various simplifications to deduce the answers of interest [69–73]. Instead, to avoid the full complexity of these equations, we start with a small number of much-simpler expressions describing individual effects such as hole collapse under surface tension and fibre drawing under an elongating force. We adopt approximations that were found allowable in the previous studies: we neglect inertia, gravity and temperature differences transverse to the draw direction x; we assume a slender neck-down region; and we assume incompressible glass with a known temperature-independent surface tension. We also restrict our study to the drawing of a fibre from a preform containing a single hole that is small compared with the outer diameter – the simplest system capable of representing the effects of viscosity distribution, surface tension and applied pressure. This approach gives a derivation that can be more easily followed by the non-mathematician while still leading to a non-trivial result.

The hole will change size when the preform is drawn. Firstly, all transverse dimensions decrease as the fibre is drawn down in size. Secondly, the hole is subject to transverse forces due to surface tension, viscosity and applied pressure differences. In the first case we consider drawdown in the absence of transverse forces (i.e., as if the hole is a solid glass feature in the preform). A preform of radius r_1 is fed into a furnace at the feed rate u_f and a fibre of radius r_2 is drawn out at the draw speed u_d, all in the direction of positive x, Fig. 3-1. The furnace

gives the glass a viscosity distribution $\mu(x)$, defined for all x by having infinite values outside the furnace. We assume the drawing process has reached a steady state, with a constant draw tension F, and that volume of glass is conserved. In the second case we consider heating in the absence of draw down. In the furnace, a hole with radius $R(x)$ under the balance of three transverse forces: the inward pressure p_{st} caused by surface tension, effective pressure p_{v} induced by viscosity for preventing any size changes and finally the hydrostatic pressure difference p_0. In a small time interval, the small diameter changes due to both can be added to form a differential equation that can be solved. Following these procedures and solving a differential equation we get the analytical description of hole radius $R(\rho)$, Eq. 3.1, as a function of local drawdown ratio ρ, which varies from $\rho = 1$ at the preform ($x \to -\infty$) to $\rho = \rho_0 = r_2/r_1$ at the final fibre ($x \to \infty$).

The mathematical derivation of this analytical solution was carried out by Tim Birks and is beyond the scope of this chapter. Instead, it is provided in the appendix A. Here we only show the final results whose validity will be tested experimentally later. If the initial hole radius (in the preform) is R_0, the local hole radius can be expressed as

$$R(\rho) = \rho e^{\frac{-3\pi p_o r_1^2}{2F}\rho^2}\left[e^{\frac{3\pi p_o r_1^2}{2F}}R_0 - \frac{3\pi\gamma_{st}r_1^2}{F}\int_\rho^1 e^{\frac{3\pi p_o r_1^2}{2F}z^2}dz\right]. \tag{3.1}$$

The integral in Eq. (3.1) does not have elementary solutions in general. However, it can be expressed in terms of the error functions erf and erfi. Setting $\rho = \rho_0$ in Eq. (3.1) gives the final hole size in terms of parameters that are readily known. In particular, it is not necessary to know anything about (or make assumptions about) the viscosity profile $\mu(x)$ along the glass body. This is because viscosity determines the dynamics of hole-size changes and fibre drawing in the same way. The relationship between the hole sizes in the preform and the fibre Eq. (3.1) depends only on the three easily measurable parameters of draw tension, draw-down ratio and hole pressure, given that surface tension can (despite some contrary evidence [34]) be taken to be a known material constant.

Insight is gained by subtracting copies of Eq. (3.1) for two holes of different initial radii $R_{0,1}$ and $R_{0,2}$ to find their size difference in the final fibre (or indeed at intermediate points) without the integral term

$$R_2 - R_1 = \rho e^{E(1-\rho^2)}\left[R_{0,2} - R_{0,1}\right]. \tag{3.2}$$

where $E = \frac{3\pi p_o r_1^2}{2F}$ is exaggeration parameter. This shows that the hole size dif-

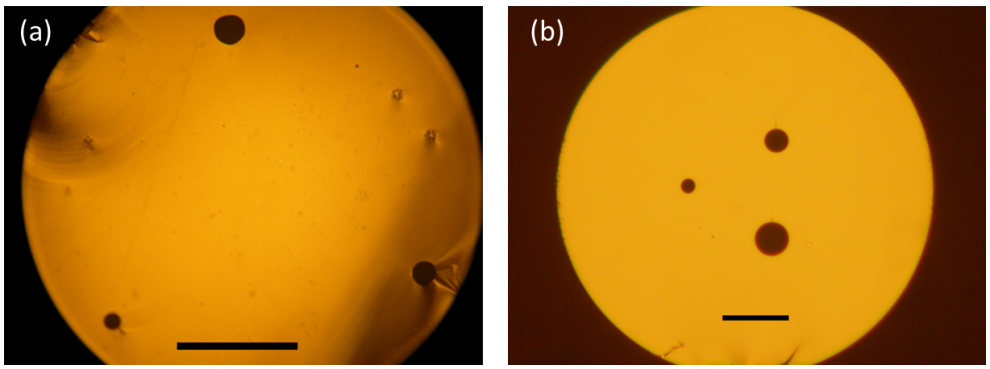

Fig. 3-2: Optical micrographs of (a) the preform cane (1 mm scale bar) and (b) a typical fibre drawn from the preform (20 μm scale bar).

ference scales with the drawdown ratio ρ but multiplied by an exponential factor whose size depends mainly on what can be termed the exaggeration parameter E, since $1 - \rho^2 \approx 1$ at the fibre. Although pressurisation is widely used to stabilise the absolute hole size when drawing PCFs despite the collapsing effects of surface tension, according to Eq. (3.2) it causes holes of different sizes to diverge exponentially in size according to the ratio of the pressure difference to the draw tension. The extent to which the sizes diverge reduces with increasing draw stress (i.e., for lower temperatures, shorter hot zones or faster processes).

3.3 Experimental tests

3.3.1 Fibre design and experiment

In order to verify the validity of Eqs.(3.1) and (3.2), we designed and fabricated a three hole fibre. These three holes should be isolated and not affect each other or be affected by outside environment to meet the assumption in our model: a single isolated hole. Standard stack and draw technique was used to make such a stack. Instead of using lots of capillaries to form a normal PCF stack, most of this stack was made of solid rods except three-hole regions (using capillaries). In order to minimise deformation from stack to cane, special care was taken, such as using relatively thick capillaries to form the three-hole region and appropriate temperature. The cane image is shown in Fig. 3-2 (a), containing three isolated holes of differing diameters 150, 203 and 263 μm and separated by 2.6 mm from each other. This cane was used to draw our fibres. A preform was assembled from this cane, with a surrounding jacket tube to increase the outer diameter. The

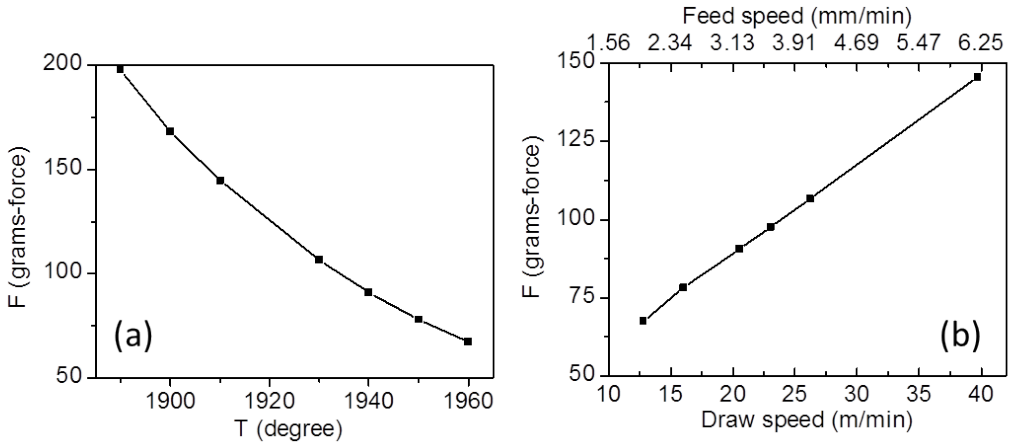

Fig. 3-3: Graphs showing how draw tension changes as a function of (a) recorded temperature at a fixed draw speed and (b) draw speed at a fixed temperature.

stack and preform were made specifically to test our model, and were not designed to make fibres that guide light. In each draw, nitrogen gas with a given pressure p_o above atmospheric pressure was applied to all three holes, subjecting them to identical un-normalised draw parameters except for the different initial hole radii R_0. The fibres were drawn at various draw speeds and furnace temperatures, resulting in various measured draw tensions, but in all cases the ratio of preform feed rate and fibre draw speed was kept fixed at a value that yielded a fibre diameter of 125 μm when the holes were negligible in size. This ensures that the final drawdown ratio ρ_0 is fixed for all the experiments. The final hole radii were measured using a high-power optical microscope, for which we conservatively estimate the diameter uncertainty to be $\pm 1\mu$m.

The diameters of the three holes were recorded for a given applied pressure as a function of draw tension F, where F was changed in two independent ways. Firstly, the furnace temperature was adjusted with the process speeds fixed, which changes the viscosity of the glass in the furnace, Fig. 3-3(a). Secondly, the process speed was adjusted (by changing the preform feed and fibre draw speeds by a common factor) with the temperature fixed, which keeps the viscosity constant, Fig. 3-3(b).

We also monitored the diameters of the three holes when the applied pressure was varied. During these process, all other parameters were kept constant.

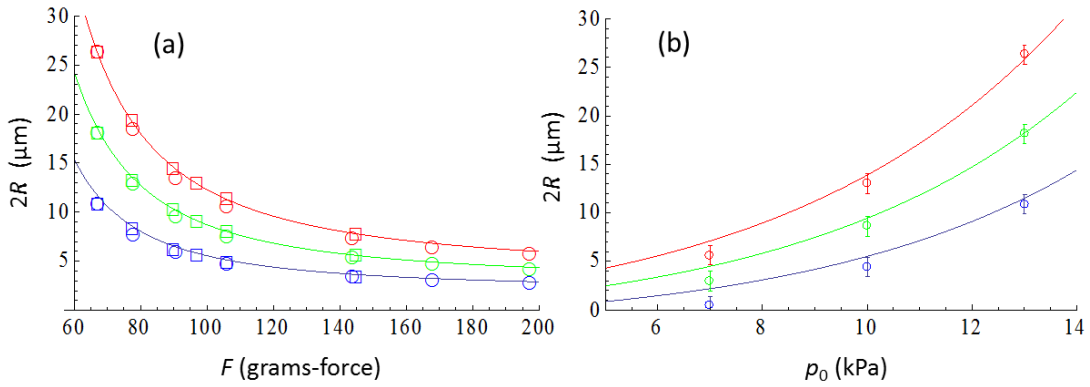

Fig. 3-4: (a) (points) Measured final diameter $2R$ versus draw tension F for three holes in a fibre. F was varied by varying T between 1960 - 1890 °C (circles) or the process speeds with u_f/u_d fixed and u_f between 2 - 6.2 mm/min (squares), from a common pivotal case where $F = 67$ grams-force, $u_f = 2$ mm/min, $u_d = 12.8$ m/min, $r_2 = 62.5$ μm, $p_o = 13$ kPa and $T = 1960$ °C. (lines) Corresponding predictions from Eq. (3.1) taking $\gamma_{st} = 0.3$ Jm^{-2}. (b) (points) Measured final diameter $2R$ versus hole pressure p_o, where the other parameters match the pivotal case in (a). (lines) Corresponding predictions from Eq. (3.1).

3.3.2 Results

One of the key findings in our model is that draw stress has the same effect on hole size no matter how it is changed when the drawdown ratio kept constant. In this case, the difference between draw stress and draw tension is just a constant, which is equal to the glass area in the transverse plane. There are many ways to change draw tension: temperature, draw speed, hot-zone length, temperature profile within the furnace, or even gas flows in the furnace. Due to availability and controllability, we concentrated on temperature and draw speed to check the relationship between them and the draw tension. Each time just one parameter, temperature or draw speed, was changed, while other effects kept untouched. Typical results are shown in Fig. 3-3. Fig. 3-3(a) was obtained when temperature was varied from 1890 °C to 1960 °C while the draw speed kept constant at 12.8 m/min. It shows that the draw tension decreases with temperature. The exact shape of this curve is determined by the viscosity profile of glass in this temperature range [74], which is not important for our model here. How the draw tension is changed by draw speed is shown in Fig. 3-3(b) when the temperature was kept at a constant value of 1960 °C. During this process, the feed rate was also changed proportionally in order to keep a constant draw down ratio. This time we can see a directly linear relationship between them. It must be noted

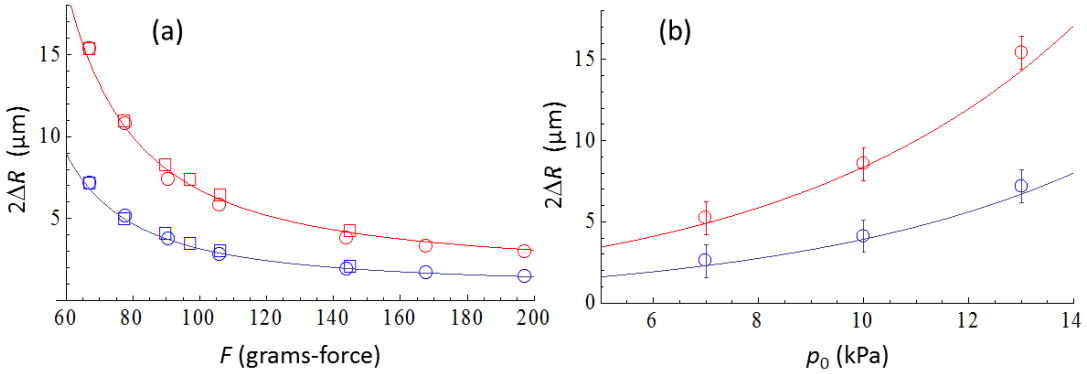

Fig. 3-5: (a) (points) Measured differences between the final diameters of the smallest hole and (red) the biggest hole and (blue) the intermediate hole versus draw tension F . (lines) Corresponding predictions from Eq. (3.2) taking $\gamma_{st} = 0.3$ Jm^{-2}. (b) (points) Measured differences between the final diameters of the smallest hole and (red) the biggest hole and (blue) the intermediate hole versus hole pressure p_o. (lines) Corresponding predictions from Eq. (3.2) . The data used for this graph is the same as Fig. 3-4.

that it is just the curve shape or relationship which are important, not the exact values or coefficients. The exact values could be varied by other parameters or even vary from time to time as the furnace elements degrade.

The measured diameter variations $2R(F)$, plotted as points in Fig. 3-4(a), coincide for the two different ways of changing F, confirming our result that the draw stress in the fibre has the same effect regardless of how it is changed. We therefore expect that changing the draw tension by instead changing the hot-zone length or the temperature profile within the furnace would also have no effect other than via F, though we were not able to test this because only one furnace element was available to us.

Fig. 3-4(a) also shows that the predictions of the model, plotted as continuous lines, are quantitatively matched by the experiments. We emphasise that this was achieved without the introduction of any adjustable fitting parameters.

How hole size changes by varying pressure p_o was also tested for common values of the other parameters, Fig. 3-4(b). The experiments matched Eq. (3.1) very closely at all pressures, and confirmed that positive pressure exponentially exaggerates hole size differences.

Eq. (3.2) was also tested by plotting the hole size differences between the diameters of the smallest hole and the biggest hole and the intermediate hole versus different draw tension F, Fig. 3-5(a), and different applied pressure p_o, 3-5(b). The data used for Fig. 3-4 and Fig. 3-5 are based on the same experiment

and essentially the same. The predictions of the model were plotted as continuous line for comparison between experiment and theory. It is obvious that they agree with each other excellently.

It is confirmed by our experimental results that our model is very accurate and efficient for predicting hole size changes during fibre draw process. This unquestionably can help fibre fabricators control the hole size to meet specific requirements and applications.

3.4 Discussion and conclusions

We have shown the sizes of isolated holes in optical fibres can be modelled without any need to know the viscosity distribution (or associated parameters such as temperature and hot-zone length) along the hot glass body. Our model accommodates the effects of surface tension and pressurisation of the holes, and predicts that the outcome depends only on the pressure p_o in the holes, the drawdown ratio ρ_0 (fixed by the ratio of the preform feed rate and the fibre draw speed) and the draw tension F in the fibre, with surface tension γ_{st} as the sole material constant. Other variables, such as feed rate, draw speed, preform diameter, fibre diameter, hot-zone length, furnace temperature and the profiles of temperature and viscosity, are relevant only in so far as they determine these three. It is thus possible for the first time to simulate the outcome of at least some PCF drawing experiments (those where the holes are well-separated [75]) using only quantities that can actually be measured, since unlike viscosity the draw tension in the fibre is well-defined and routinely measured and logged by fibre fabricators.

Our result Eq. (3.1) expressed as hole radius $R(\rho)$, where the drawdown ratio ρ_0 in the final fibre is determined by the process speeds, is straightforward to calculate. There are many ways to draw a fibre with a hole of a given size starting with a given preform, by suitably varying both hole pressure and draw tension to give a particular $R(\rho_0)$. However, our even-simpler result Eq. (3.2) highlights how positive pressure, despite its widespread use to stabilise holes while drawing fibres, causes small differences in hole size to become exaggerated according to the parameter E.

A three hole fibre was specifically designed and fabricated to test our model. It is found that draw tension varied by temperature and draw speed has the same effect on holes size change. It is reasonably to think that other ways of changing draw tension would have the same effect, although they are not available to us.

The experimental results confirmed the tendency of hole changes predicted by our model, especially those from the Eqs. (3.1) and (3.2). It is suggested that a high draw stress is desired for minimising hole size divergence during fibre drawing process. Although positive pressure is normally used for fabricating PCFs, it also exaggerate the difference between dissimilar holes.

Chapter 4

Optical fibre spectrometer based on Young's slits

Hole control during fibre drawing process was discussed in the preceding chapter. From now on, we will investigate how the hole pattern and core structure of a PCF can be modified after it has been made, and related applications based on these modifications. The modification can be done either by using a taper rig or a fusion splicer, depending on specific applications. The purpose of this chapter is to make a Young's double slits based device, which has potential applications in fibre optic spectrometers.

4.1 Introduction

A spectrometer is an instrument which can accurately measure the spectral information of a light source and has numerous applications in both scientific and industrial areas. A conventional spectrometer often relies on dispersive elements, such as gratings or prisms, to get wavelength-dependent diffraction or refraction pattern. In its standard configuration, there exist variable slits used for beam control. By rotating the dispersive elements, each time just a small portion of the dispersed light can reach the photodetector and has been interrogated. The spectral-to-spatial mapping then gives accurate information about spectral distribution and its intensity by a properly calibrated spectrometer. However, containing moving parts means that it may suffer from mechanical problems and misalignment. Moreover, for a high resolution and high dynamic range measurement, several pieces of large dispersive elements are needed, making the system bulky and expensive to build.

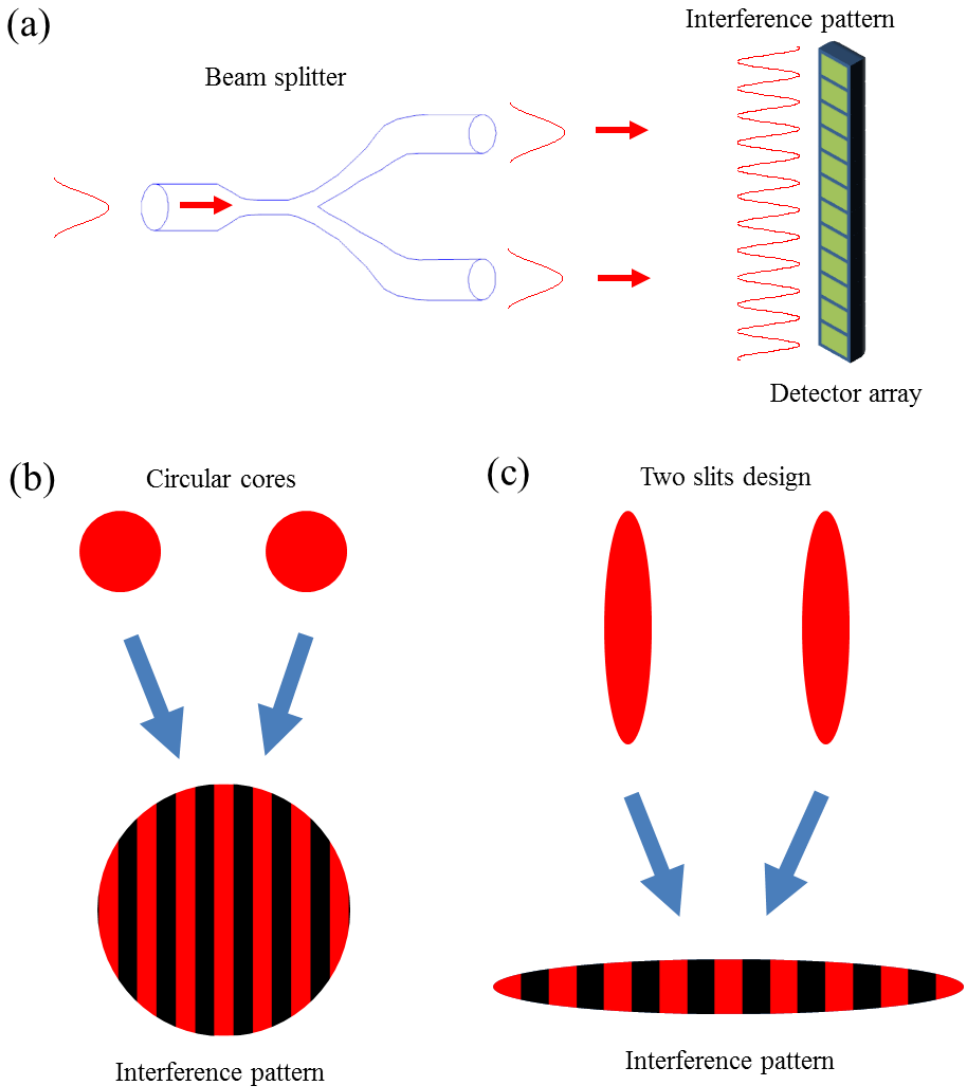

Fig. 4-1: (a) Typical configuration for static, passive, fibre based spectrometers. (b) Schematic diagram about the near field patterns and corresponding far field interference pattern for fibres with circular cores. (c) as (b) but for fibres with high aspect ratio, slits-like cores.

Our collaborators in PiePhotonics are interested in portable, passive spectrometers, no scanning parts and no moving elements, based on the interference of two beams [76]. An input beam has been equally split into two via a beam splitter, or an optical fibre Y-junction, as shown in Fig. 4-1(a). These two beams come out of the fibres and interfere with each other to generate an interferogram in the far field. This is like the Young's slits experiment, but with circular slits. A detector array is used to capture this signal for post-processing and analysis. The spectral and phase information can be obtained by fringe counting and weighting algorithms and Fourier transform processing.

Normally the fibre used is a conventional single mode fibre (for example, Corning SMF-28) and has a circular core. A Gaussian shape beam is guided in the core and evolves into a similar Gaussian shape far field when it comes out of the fibre end. It can be imagined that the interference pattern of two such beams, which is the case for the spectrometer, will be also Gaussian shape but with modulated pattern caused by interference. This process is schematically shown in Fig. 4-1 (b). Considering that the detector used is a 1-D CCD array, which is not compatible with the shape of the interference pattern generated, this means most of light can not be captured and will be wasted. This affects its sensitivity, especially for detecting weak signals. The other problem is that the uncaptured signal becomes stray light, increasing noise level and reducing the dynamic range. Obviously, it is worthy to design and make a device producing an interference pattern compatible with the detector array by changing the core and cladding structure. Moreover, it is more favourable to combine two fibres into one, which means two cores inside one fibre. This could facilitate compact and reliable devices. Fig. 4-1 (c) shows this new design. Two parallel beams with high aspect ratio come out of two rectangular slit-like cores, and evolve to the far field, which is the Fourier transform of the near field pattern. During this diffraction, the long and short axes of the pattern swap, to give a shape perfectly matching the structure of 1-D detector array, Fig. 4-1 (c). It has previously been demonstrated that a transition from a normal circular core to a rectangular core with high aspect ratio [67] can be achieved with the technique discussed in Chapter 2. In that paper, the modified core shape gave improved coupling efficiency from a diode laser, based on a similar principle discussed here.

In the rest of this chapter, we will demonstrate this idea by modifying a coreless fibre. Slit-like cores were obtained by post-processing the holey region of this new fibre. This project was started in the last few months of my PhD study, so

I did not have enough time to fully exploit the advantages of this new design. However, this proof-of-concept demonstration clearly shows two key things. First, Young's double slits design gave much better performance compared to that of the circular core design in terms of compatibility and intensity enhancement. Second, this design can be achieved in just one fibre with two cores instead of two fibres with separated cores.

4.2 Fibre fabrication and experimental results

In order to realise the new design shown in Fig. 4-1 (c), a special fibre is needed. The separation between two slits determines fringe numbers and related resolution and should be made as large as possible. This means that a normal PCF is not ideal for post-processing to get Young's double slits, as the central core will limit the separation. So we started from a core-less cane with the structure shown in Fig. 4-2 (a). The cane was made by Agata Witkowska during her PhD study, so was immediately available to me when I started this project, which saved my time (no need to begin with a new stack). It was made by the standard stack and draw technique but without a core rod. This 4.8 mm cane was then put into a jacket tube to make a fibre shown in Fig. 4-2 (b). The outer diameter, pitch and hole size of this fibre are 125 μm, 4.36 μm and 1.58 μm, respectively. The d/Λ was designed to be less than 0.4, which follows the endlessly single mode rule [6].

This fibre was then used for post-processing, using techniques discussed in Chapter 2. At one end all holes were sealed. At the other end, some selected holes had been plugged with glue and kept at atmospheric pressure, while others had been pressurised to balance surface tension when heated on a tapering rig. After this treatment, different core shapes can be formed. In order to have a direct comparison between designs shown in Fig. 4-1 (b) and (c), two different core structures were made, which are illustrated in Fig. 4-4 (a). The first one was made by collapsing two widely separated single holes. Strictly speaking, these cores are hexagonal instead of circular due to the stacking method. However, they can be considered as circular and are good analogue to that shown in Fig. 4-1(b). The other device had two slit-like cores (with an aspect ratio of 4:1), which resembles that of Fig. 4-1 (c). The separation between cores are the same in these two devices, which is 22 μm. Both devices had similar lengths of about 9 cm.

The experimental setup shown in Fig. 4-3 was used to characterise devices. A supercontinuum source was coupled to the devices via objective lenses. By

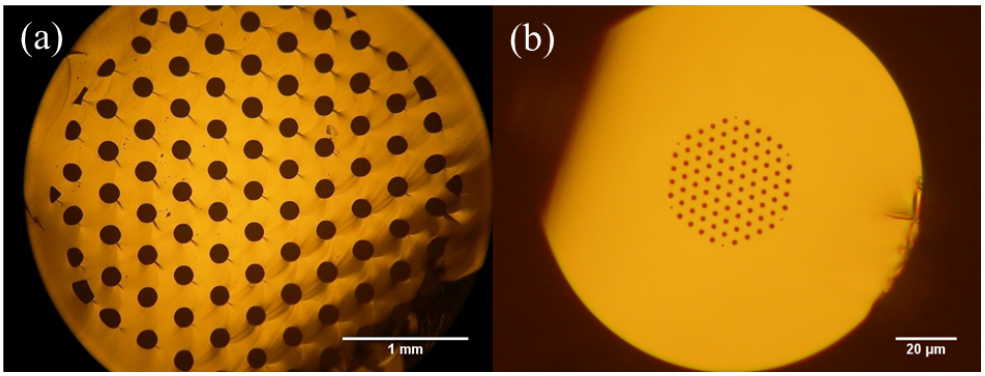

Fig. 4-2: (a) The cane used to make a coreless fibre. Due to the limited field of view of the optical microscope used, this image just shows the central part of the cane, which had a diameter of 4.8 mm. The holey region, however, can easily be seen. (b) The coreless fibre made from the cane shown in (a) and used for the experiment.

adjusting the coupling position, light can be coupled to both cores simultaneously. Devices were plastered with Tipp-Ex to remove cladding modes. This experiment was carried out at 1550 nm, using a 10 nm bandpass filter. Another objective lens was used to image the near field patterns and the interference fringes, which were captured by an InGaAs camera, Fig. 4-4 (b-d).

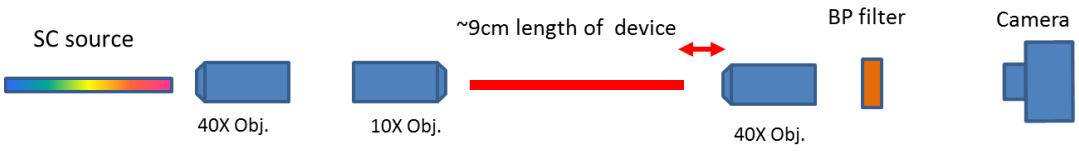

Fig. 4-3: A schematic of the characterisation setup. SC, supercontinuum source; Obj., objective; BP filter, bandpass filter.

These two devices behaved as expected. In the near field, fundamental modes were excited by the input beam which was broad enough to illuminate both cores. Near field pattern evolved to its far field as it propagated in free space. For circular cores, a Gaussian shape was observed (with modulated patterns). In contrast, for the double slit-like cores, light was confined to a much narrow area, which matches with the detector array used in a static fibre spectrometer. By analysing the intensity distribution and evolution of captured images from near field to far field, we can compare the performance in term of intensity enhancement. Light intensity in the case of circular cores was higher than that of the double-slit case in the near field. However, in the case of far field, we saw much higher intensity distribution in the case of double slits, Fig. 4-4 (c-d).

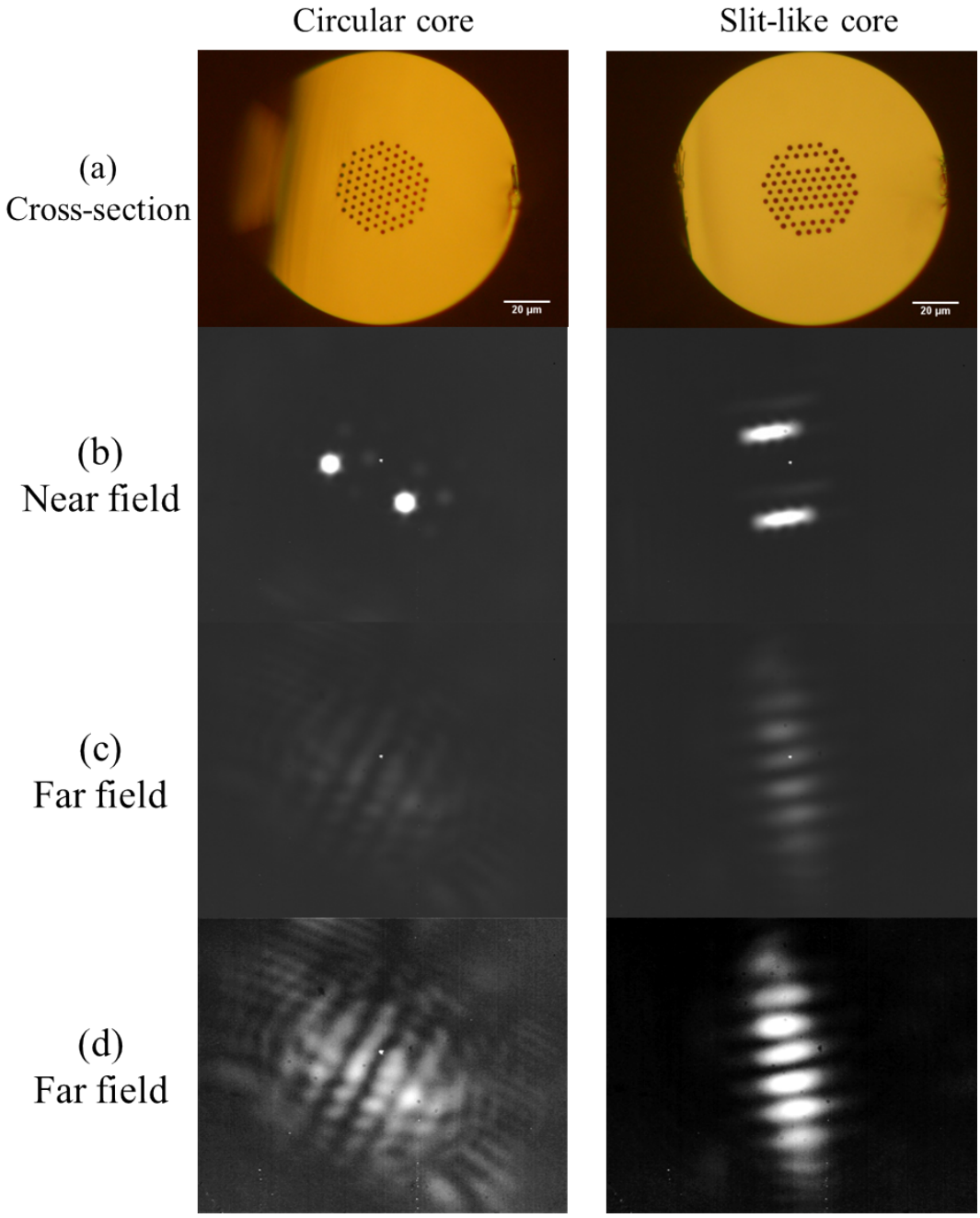

Fig. 4-4: (a) Cross section comparison for devices with circular cores and high aspect ratio, slit-like cores.(b-d) Corresponding near field and far field patterns at the wavelength of 1550 nm and captured by an InGaAs Camera, which has some obvious bad pixels. The far field patterns (c) were obtained as near field (b), but the imaging lens was defocused. (d) is the same as (c), but with increased brightness and contrast (the same amount in both) to highlight faint features. (b-d) are shown to the same scale.

4.3 Conclusion and discussion

We have demonstrated that the interference pattern based on Young's double slits has much improved performance over that based on normal circular cores. The well-defined interferogram is compatible with the 1-D detector array used for static, passive fibre based spectrometers. Enhanced intensity is critical to increase the sensitivity for weak signal detection.

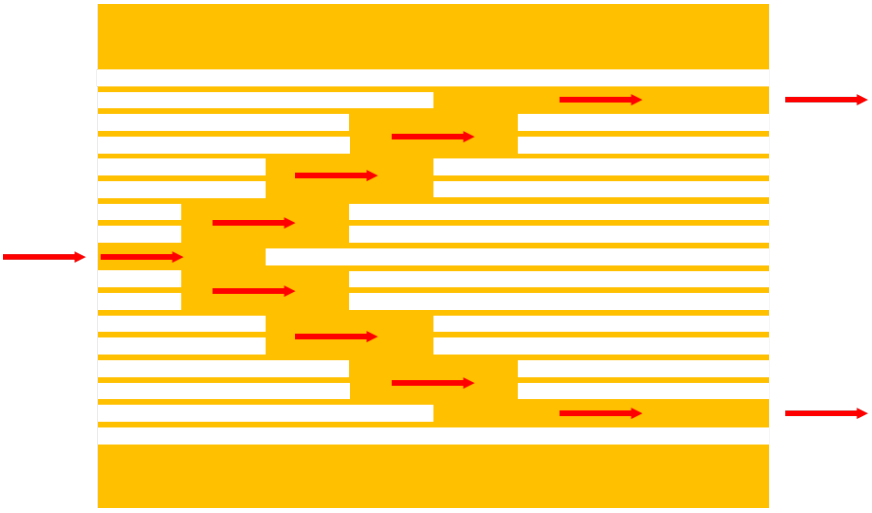

Fig. 4-5: Schematic diagram about core walk-off design. Silica area is shown in gold, while holes area is shown in white.

Due to time constraints, I did not fully explore all the advantages provided by this novel design. For the same reason, although the results shown here are promising, they are not perfect and have some limitations. There are still a lot of things which can be done to improve the performance and make it commercialisable in the future. I will end this chapter by briefly mentioning several problems and possible solutions.

First, it is necessary to increase the number of fringes. The limited number of fringes will lower the resolution and reduce the accuracy that can be obtained. This can be solved by making another fibre with more rings of holes and larger diameter. Slits can then be made with larger separation by using similar post-processing techniques.

Second, the coupling efficiency should be addressed. For the purpose of a proof-of-concept demonstration, this was not particularly important and so we ignored it. For the device shown in Fig. 4-3, the core structure was uniform along the whole device length. This requires a very large beam to excite both cores,

especially when the separation becomes bigger. However, a core walk-off design can solve this problem, which is shown schematically in Fig. 4-5. Light will be coupled to the central core formed by collapsing the central hole. This is exactly the same as normal coupling which can have very high coupling efficiency. A few outside holes will be collapsed to form a slit-like core, and light will spread out [67]. Then more holes collapsed to form big rectangle core. After this, this big rectangle cores will be split into two when holes reappear (at selected positions). This process will be repeated until the separation is large enough. All the transitions should be gradual to avoid coupling.

Chapter 5

LP_{01}-LP_{02} mode convertors

In the last two chapters, we described how hole control techniques were used in fibre drawing and for making devices by post-processing of fibres. We will continue the discussion on these techniques, and particularly focus on post-processing of PCFs after they have been made by the standard stack and draw technique. In this chapter, all-fibre, low loss, broadband LP_{01}-LP_{02} mode convertors are made in highly nonlinear PCFs using the techniques described before.

5.1 Introduction

Until now, most of the research done in optical fibres has focused on the fundamental mode. The reason is understandable: it simplifies the fibre design and related optical system. Single mode fibres are commonly used in current telecommunications systems to avoid intermodal dispersion effects, which happen in multimode fibres and limit the possible data propagation rate available for an optical fibre communication system. When designing a fibre, higher order modes can be easily cut off by choosing an appropriate V parameter. The other reason is that the field distribution of the fundamental mode most closely resembles those of external light sources and detection systems. This greatly simplifies the input and output coupling and enhances the coupling efficiency. However, higher order modes have many features that are different or sometimes impossible for the fundamental mode. For example, it has been shown that the TE_{01} mode has the lowest loss in a Bragg fibre which supports multiple modes [77]. Moreover, the intensity distribution and polarisation properties make cylindrical vector beams suitable for applications like molecule and atom trapping/guiding and laser machining [78]. Some higher order modes, including TE_{01} and TM_{01}

mode, provide a possibility for eliminating polarisation mode dispersion (PMD) and get a true single mode operation. The mode guided in the so-called single mode fibres is HE_{11} and actually has two polarisations if the mode degeneracy is considered. However, the TE_{01} or TM_{01} modes are non-degenerate, which in principle can be used to avoid PMD in an optical transmission system. Furthermore, Ramachandran's group has investigated the LP_{02} mode for dispersion compensation, for the reason that by an appropriate design it can have high normal dispersion at telecommunication wavelengths [79]. They also studied its anomalous dispersion property at short wavelengths [80]. Purnananda et al.'s result shows that the HE_{21} mode has a blue shifted zero dispersion wavelength, compared with that of the fundamental mode [23]. Actually, this property also applies to other higher order modes [81]. The main reason for this is that higher order modes are more sensitive to the properties of optical waveguides. In other words, waveguide dispersion plays a more important role. In the next two chapters, we will investigate this property in detail and apply it for SC genearation and FWM. Other higher order modes like Bessel beams have numerous interesting properties, among which are non-diffraction and self-healing. Practically Bessel beams can be resembled by a very higher order mode (LP_{0n}) [82, 83].

Even in the field of telecommunication, people are reinvestigating the advantages of multi-mode fibres. This is due to the increasing demand for large transmission capacity, driven by rapidly increased internet traffic, like cloud computing and higher speed ports [84, 85]. In the view of information theory, multiple modes provide another degree of freedom and additional capacity.

In practice, excitation of higher order modes in a controlled way is not easy. Compared to the design principle of single mode fibres, which normally means reducing the V parameter, there is not a straightforward way to keep a particular higher order mode while getting rid of the fundamental mode. Ways to achieve high efficiency coupling which have been reported since the early days of optical fibres [86, 87]. A tilted or offset beam is usually suggested for this purpose. A few attempts have followed these suggestions by carefully focusing a Gaussian beam to the fibre core by trial and error [21, 22, 88]. It is easy to understand that this way is neither efficient nor stable. A small perturbation will change the mode pattern significantly.

The fundamental mode can be efficiently and, more importantly, stably excited in a single mode fibre. If we then can find a way to transfer the energy of the fundamental mode to the desired higher order mode, this problem can be

fully solved. Undoubtedly, a specially designed mode convertor is a useful and efficient component for this requirement.

A well-known mode convertor is the one that takes advantage of the long-period grating (LPG). As long as the grating period of the LPG matches the beat length between the modes of interest, there will be resonant coupling between these two modes. However, the performance of this mode convertor is limited by the fact that it is based on the resonance in a fibre grating. High efficient mode conversion only happens over a very narrow spectrum range: over coupling or under coupling result in some residual power in the input mode, reducing the extinction ratio dramatically [79]. It can therefore only be used for a specifically narrow band of wavelengths even though it has been carefully designed and fabricated.

Other types of mode convertors using methods like optical phase shifters [89], multiple mechanical bends [90], or holograms generated by spatial light modulators [91] have also been investigated. However, all of these proposals are complicated and need other mechanical or optical components.

Intensive studies have been carried out at the University of Bath on low loss, all-fibre mode convertors. By controlling the sequence of propagation constants of different modes and the symmetry of a waveguide structure, high efficiency mode conversion (100% in theory) has been achieved. A series of stable and wavelength independent mode converters based on endlessly single mode PCF were successfully demonstrated [92, 93]. For example, Lai et al. made an LP_{01}-LP_{02} mode convertor based on a 5 μm core single mode PCF. It had a high extinction ratio, low loss and broad working range (600-1200nm) [92]. Using the same fibre but different design, Witkowska et al. achieved an LP_{01}-LP_{11} mode convertor (TE_{01} and HE_{21} mode) [93].

These mode convertors perform well for some applications. However, they were formed in endlessly single mode PCFs, so higher order modes can only exist in the treated part. If the generated higher order mode needed for further studies, bulk optics may be needed for coupling it into other fibres that have the ability to support higher order modes. Undoubtedly, this introduces unavoidable loss. One important application of higher order modes is for blue/UV supercontinuum generation. However, the enlarged core in the mode convertors previously reported is a poor nonlinear medium: it is too big, too poorly controlled, and its length is limited to a few centimetres by the post-processing method.

To overcome these problems, a new mode convertor is reported in this chap-

ter. Highly nonlinear PCFs, rather than endlessly single mode PCFs, were used for this purpose. More importantly, the generated higher order mode doesn't stop at the treated part of the device, it squeezes into the original core of the fibre in an adiabatic way (no mode coupling) and continues its propagation along the following length of the fibre. This way provides a monolithic way (no splices, cleaves, and butt coupling) for the fundamental mode to be converted to a higher order mode, which can then be used for other applications. If it is necessary, this higher order mode can also be converted back to the more familiar fundamental mode, as we will discuss in this and the following chapters. Moreover, the higher order mode has a potential to be converted to even higher order modes by concatenated mode convertors (combining two or three mode convertors).

This chapter gives a detailed description about this LP_{01}-LP_{02} mode convertor. Simulation results obtained by the scalar beam propagation method (BPM) gave a good understanding about the principles of this convertor and provided guidance for the experiment. Experimentally, the post-processing technique was used to modify the cladding structure of the PCF to favour such a conversion. Linear characterisation of this mode convertor revealed its good properties, such as high mode purity (more than 20 dB), low loss (0.1 dB at some wavelengths), and broadband conversion (at least 400-1100 nm). The applications of this mode, like supercontinuum generation and FWM, will be discussed in Chapters 6 and 7.

5.2 Simulation

Propagation of light along mode convertors was simulated by BPM using the commercial software BeamPROP [94]. The model fibre was based on the measured dimensions of fibre PCF-SC-A, Fig. 6-4. The transitions were formed by allowing sets of holes to change diameter linearly without deforming the lattice. With reference to the locations A-H in Fig. 5-1, the lengths of the various sections were 0 mm (A-B), 0 mm (uniform B), 10 mm (B-D), 0 mm (uniform D), 10 mm (D-F) and 10 mm (F-H). The input wave was the fundamental mode of the modelled fibre found by the same software. In our mode convertors, controlled hole size variations along the fibre couple light from the LP_{01} mode of an unprocessed PCF to the LP_{02} mode of an enlarged core.

Mode conversion formally occurs between locations A and B, where the fibre's second ring of holes abruptly disappears to form a parasitic annular core. The fundamental mode of the composite two-core waveguide now occupies this (larger)

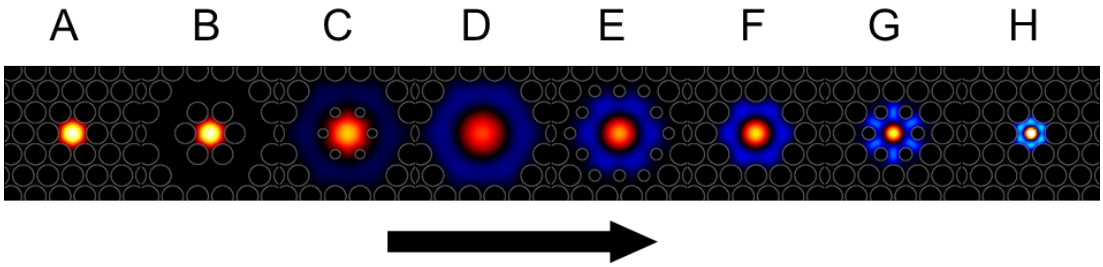

Fig. 5-1: Simulated field distributions superimposed on a simplified model structure. Red and blue indicates opposite phases in the field, and the grey circles are the hole boundaries.

annular core, and the light in the original core finds itself in a higher mode of the same symmetry. However, only the label "fundamental mode" moves to the annular core: the light itself stays where it is and its field distribution is unaffected. Next the first ring of holes gradually shrinks and disappears to form a common enlarged core (B-D). Since this transition is adiabatic, the light remains in the higher mode, now recognisable as the LP_{02} "sombrero" mode of the enlarged core [92].

The enlarged core at D is a poor nonlinear medium. Moreover, the generated LP_{02} mode is needed for further investigation (without the aid of other optics). We therefore added a further transition (beyond that in [92]) where the vanished holes reappear gradually: first the second ring (D-F) then the first ring (F-H). This shrinks the core and adiabatically squeezes the LP_{02} mode into the core of the original unprocessed fibre. The mode now propagates in this small, well-controlled core along a distance limited only by the fibre length. The structure's adiabaticity, and the lack of any resonant basis to its operation, make it efficient and low-loss across all the fibre's guided wavelengths.

Loss and mode purity were calculated from overlap integrals of the output fields with the appropriate mode field distributions. For the wavelength of 532 nm the transmission loss from input light in the LP_{01} mode was 0.0015 dB to the LP_{02} mode after the mode convertor. For the wavelength of 1000 nm the loss was 0.003 dB, illustrating not only the efficiency but also the broad wavelength range. For both wavelengths the mode purity was better than 34 dB.

The operation of the mode convertor is based on adiabatic propagation (so that the light stays in a given order of mode for a given symmetry) except between locations A and B, where the abrupt appearance of the annular core changes the mode order without affecting the field distribution. A calculation of the mode

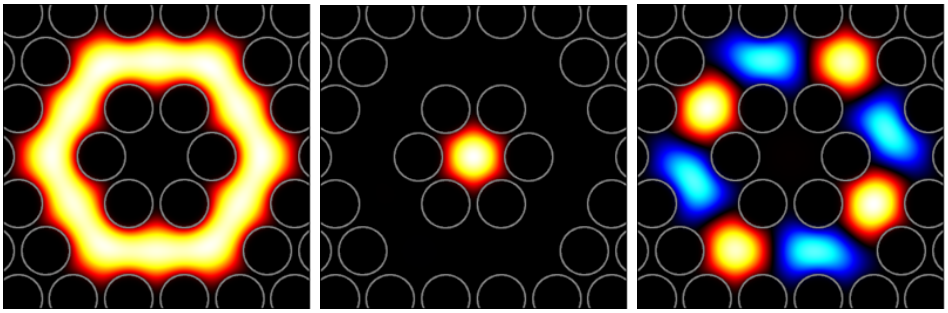

(a) (b) (c)

Fig. 5-2: Calculated fields in the composite two-core fibre structure at location B, for (a) the fundamental mode, (b) the 10th mode and (c) the 9th mode.

spectrum at location B identifies the various guided modes of the composite structure. As expected, the fundamental mode (ie, the mode of greatest propagation constant, β) fills the annular core with uniform phase, which is illustrated by Fig. 5-2(a). The input mode localised in the central core, Fig. 5-2(b), is in fact the spatial mode of 10th greatest β. The intervening 8 modes are localised in the annular core with aziumthal phase variations, one example being plotted in Fig. 5-2(c). These modes do not have the same symmetry as the input wave, and so play no role in a symmetrically-varying mode convertor.

The transition between A and B is conceptually abrupt, in the sense of being the opposite of adiabatic. However, it does not need to be abrupt on a practical length scale, just much shorter than the length scale for directional coupling between the cores at the point along the transition where they are phase-matched [63]. We estimate this length scale to be of the order of a metre for 532 nm light. Thus the "abrupt" transition can be quite long in practice. A BPM simulation of just the transition between A and B, but prolonged over 10 mm, showed that the loss of light from the central core (in what looks like the LP_{01} mode of the central core but is now the LP_{02} mode of the composite two-core waveguide) was $<$0.0001 dB for 532 nm light.

5.3 Fabrication

Mode filters

The mode converter is for LP_{01}-LP_{02} mode conversion and the fibre used is a HNPCF that supports lots of modes. Furthermore, cladding modes can also be excited. In order to make sure the mode at the input end is a pure LP_{01} mode,

a mode filter (MF) need to be fabricated in front of the mode convertor, filtering out all higher order modes and cladding modes.

Following the discuss in Section 1.4, it is easy to understand that heating a short length of a HNPCF to shrink the holes in the cladding can make this HNPCF behave locally as a single mode fibre.

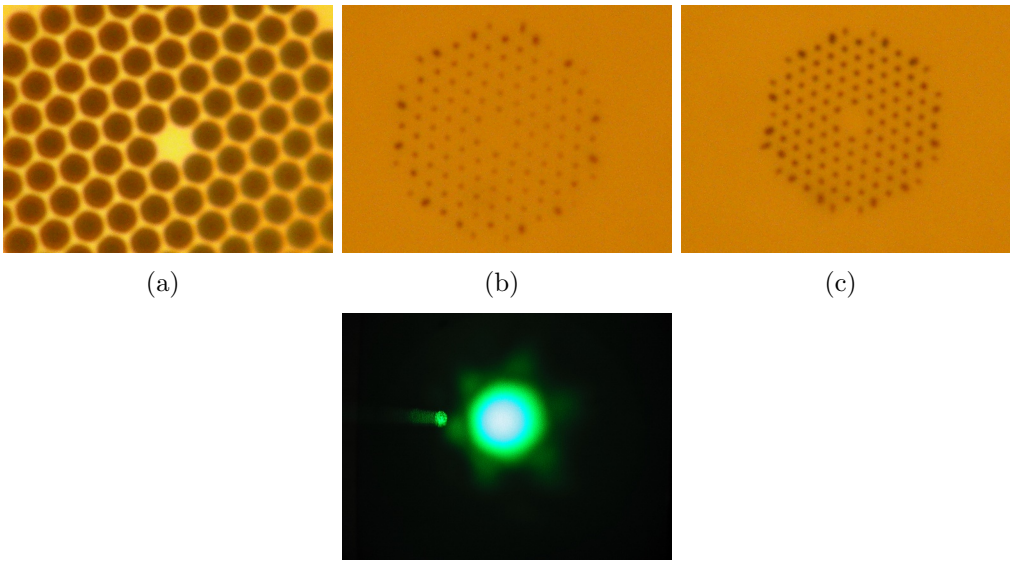

(a) (b) (c)

(d)

Fig. 5-3: Optical micrographs of the cross-sections of (a) the original HNPCF (b) the mode filter without taper, d/Λ is less than 0.1. and (c) the mode filter without taper, d/Λ is a little bigger than 0.1. (d) shows the far field mode pattern after this mode filter when illuminated by a 532nm laser.

We used the taper rig to make mode filters. Although the diameter of the core can be approximately represented by $2\Lambda - d$ in the unprocessed fibre, Fig. 5-3(a), its relative size was disproportionatly changed and much larger than $2\Lambda - d$ when the cladding holes collapsed during the treatment on the taper rig. In practice, the HNPCF just supports the fundamental mode at 532 nm when its structure becomes the one shown in Fig. 5-3(b). However, the confinement loss is high for fibres with such small holes (small d/Λ). The other problem is that it is difficult to control the taper rig (flame, burner speed, reversal times) to get the right structure. A little more heat will collapse all holes, while a little less heat means the fibre still supports other modes: the tolerance becomes smaller. In our experiments, we found by tapering the mode filter a little bit will help us to get a stable mode filter with relatively big holes, shown in Fig. 5-3(c). The far field pattern shows just the fundamental mode left after the mode filter, Fig. 5-3(d).

Mode convertor

The post-processing techniques were also used to make the mode convertors. The procedure involved two main steps.

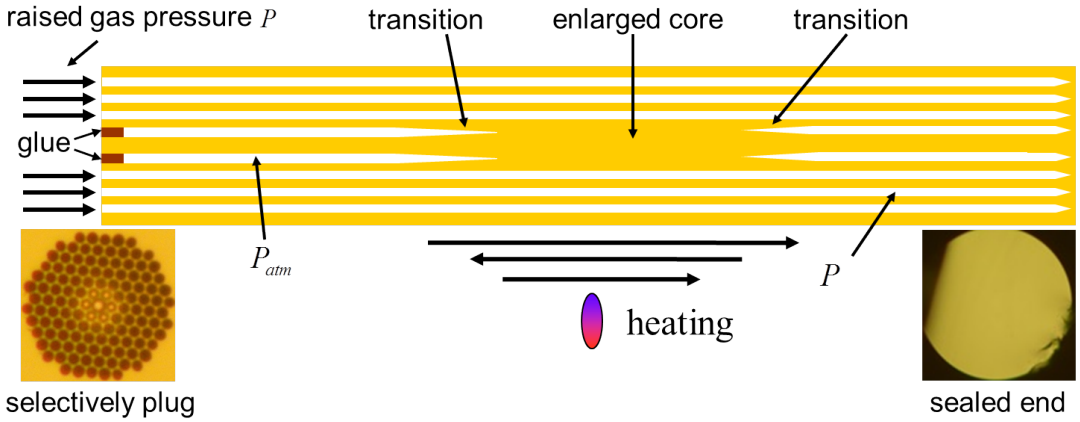

Fig. 5-4: First step of fabrication of a mode convertor. Silica areas are shown in gold, while holes areas are shown in white.

In the first step, the first ring of 6 holes around the core at one end face of the fibre were plugged by UV sensitive glue, while the other end face was completely collapsed, as shown in Fig. 5-4. Dry nitrogen at suitable pressure (P) was applied to the fibre (the end with 6 holes plugged) to raise the pressure in the unplugged holes (so that only 6 plugged holes remained at atmospheric pressure, P_{atm}). Then a short piece of about 8.5 cm of the fibre was heated on the tapering rig. The pressurised holes almost kept their original size, but the plugged holes collapsed to form a new large core around the original one. The transitions linking the sections with and without the expanded core were gradual. The whole structure at this stage is illustrated in the Fig. 5-4.

In the second step, we first cut a short piece of blocked fibre to get a fresh end and make the first ring of holes open again. Then the second and third ring of 30 holes of the same fibre were blocked. A similar procedure was applied to seal the other end of the fibre. Dry nitrogen was used again to raise the pressure in remaining holes (so that only 30 plugged holes remained at atmospheric pressure at this time). The processed fibre was treated on the tapering rig again, and is shown in Figure 5-5. At this time the heated part (about 6 cm long) was left shifted when compared to the former heated position. Now the transitions at each end are different: the left end transition was abrupt, whereas the right end transition was gradual.

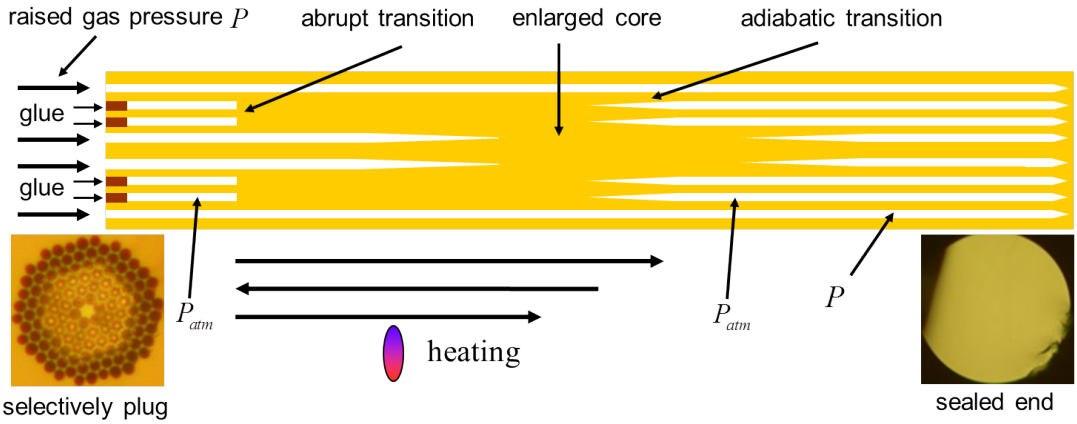

Fig. 5-5: Second step of fabrication of a mode convertor. Silica areas are shown in gold colour, while holes areas are shown in white colour.

The mode convertor was about 10 cm long and only tapered a bit to keep the fibre taut.

Whole device

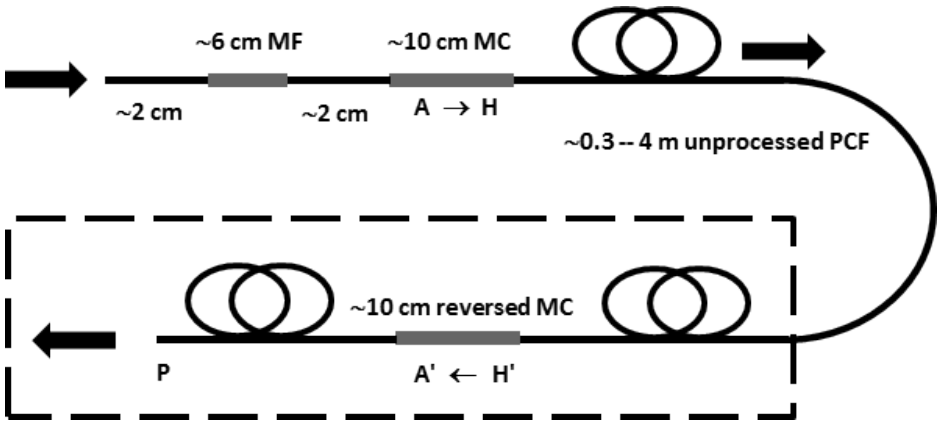

Fig. 5-6: Schematic of the whole device

The whole device for further applications consists of a 6 cm long MF, a 10 cm long MC and several metres of unprocessed HNPCF, as shown in Fig. 5-6, before the box section.

5.4 Characterisation

By applying the knowledge discussed above, a series of devices using different fibres were made to favour the nonlinear experiments carried out in Chapters 6

and 7. Here, we give the linear results obtained from devices made using fibre PCF-SC-A, although results from other fibres are very similar.

5.4.1 Near field and far field

In order to know whether our device behaves as expected, it is necessary to check the near and far field mode patterns, as shown in Fig. 5-7. These mode patterns in the fibre were measured using a separately-generated LP_{01} mode supercontinuum as a white-light source [53]. This light was coupled into the fibre under test. Far-field light patterns were projected onto a sheet of white paper and photographed using a compact consumer digital camera, using the unfiltered white light. Near-field patterns were imaged onto a lens-less camera using a 40X microscope objective (NA = 0.65) via a bandpass filter transmitting the wavelength of interest with a 10 nm passband. The camera was a CCD device for 400 to 1000 nm wavelengths (Basler, A631F) and an InGaAs array for wavelengths beyond 1000 nm (Xenics, Xeva). The near-field images in Fig. 5-7(e) are therefore not to the same scale as those in Fig. 5-7(c,d).

After having the correct near and far field mode pattern in the output of mode convertor (position H of Fig. 5-7), it is interesting to know the evolution of the structure and mode inside. The mode convertor was cut back to inspect these changes. Fig. 5-7(b) shows cross-sectional optical micrographs of the mode convertor at different positions. The changes along the structure are gradual except for the sudden appearance of the annular core between A and B over a distance of <2 mm. The light patterns at intermediate locations, Fig. 5-7(c-f), were also investigated. These compare well qualitatively with the simulated patterns (plotted again in Fig. 5-7(a) for completeness) and with each other, and confirm that the input at A is indeed in the LP_{01} mode. The patterns in the enlarged core at D are less symmetric than in the simulation, probably because the post-processed core is imperfectly symmetric. However, the output patterns at H are clear LP_{02} modes across the whole wavelength range from 400-1100 nm. Examination of the dark ring in the near-field images indicates an LP_{02} mode purity of at least 20 dB [92]. The images for location C in Fig. 5-7 were over-exposed to highlight faint peripheral features in the images. No such features were visible in similarly over-exposed images at location B (not shown).

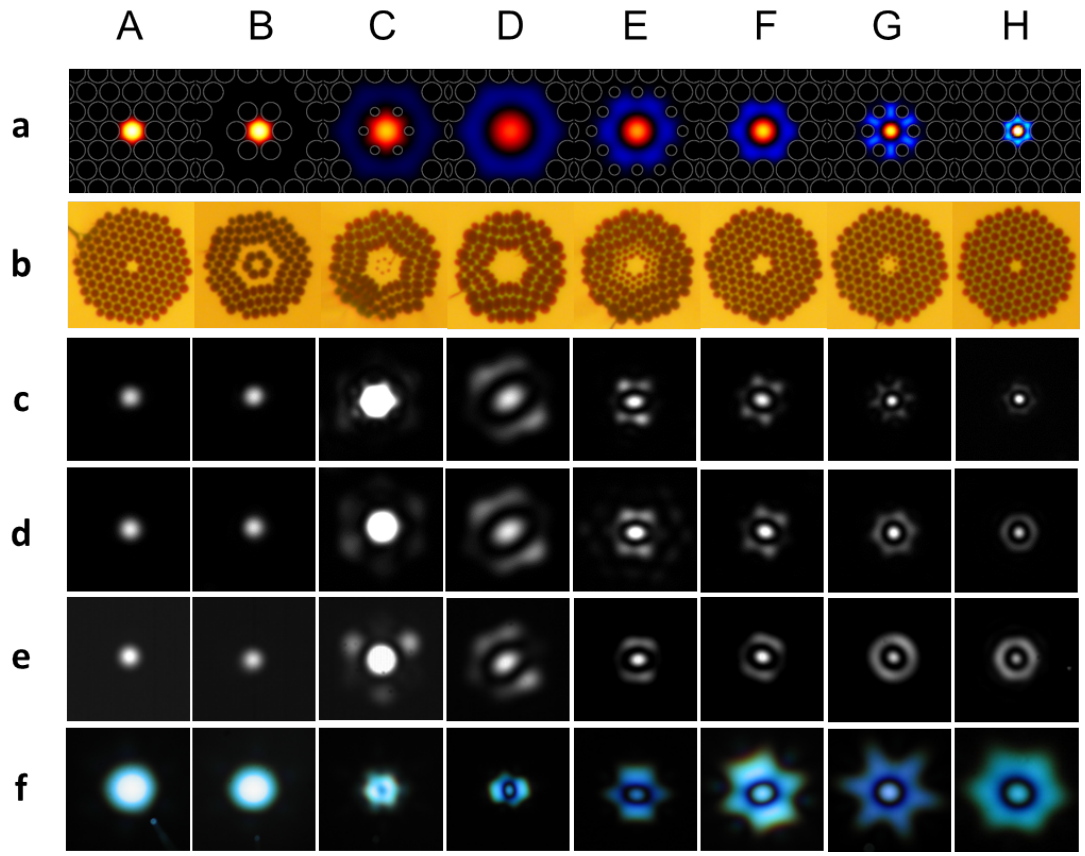

Fig. 5-7: Cross sections at locations A-H along an LP_{01} to LP_{02} mode convertor, with input in the fundamental LP_{01} mode. (a) Simulated field distributions shown here again for completeness. (b) Optical micrographs of an experimental structure made from fibre PCF-SC-A. The holey region in the untreated fibre (locations A and H) is 23 μm across. (c-e) Measured near-field patterns for light with wavelengths of (c)400 nm, (d)800 nm and (e)1100 nm. (f)Measured far-field patterns for white light.

5.4.2 Loss

The insertion loss of the mode convertor was less than 0.5 dB across the 450-800 nm wavelength range, and as low as 0.1 dB at some wavelengths.

It is also interesting to know the losses of different modes in an HNPCF. The mode filter and mode convertor provide a solution to get a pure LP_{01} (after the mode filter) and LP_{02} (after the mode convertor) mode and then the losses of these modes in that fibre.

The cut-back technique was used for this purpose. Transmission spectra were recorded using a laser driven xenon discharge light source (Energetiq, EQ99) and an optical spectrum analyser (Ando, AQ6315B). Measurements of attenu-

ation spectra for the LP_{02} mode was achieved by performing both transmission measurements with two different lengths of fibre downstream of a full device (a mode filter and a mode convertor). Absolute values measured by the spectrum analyser were unreliable because the more-divergent LP_{02} mode was less completely coupled into the instrument than the LP_{01} mode and more sensitive to the fibre cleave. More accurate single-wavelength measurements were made using bandpass-filtered light and a large-area photodiode to ensure collection of all of the divergent LP_{02} mode. The results are shown in Fig. 5-8.

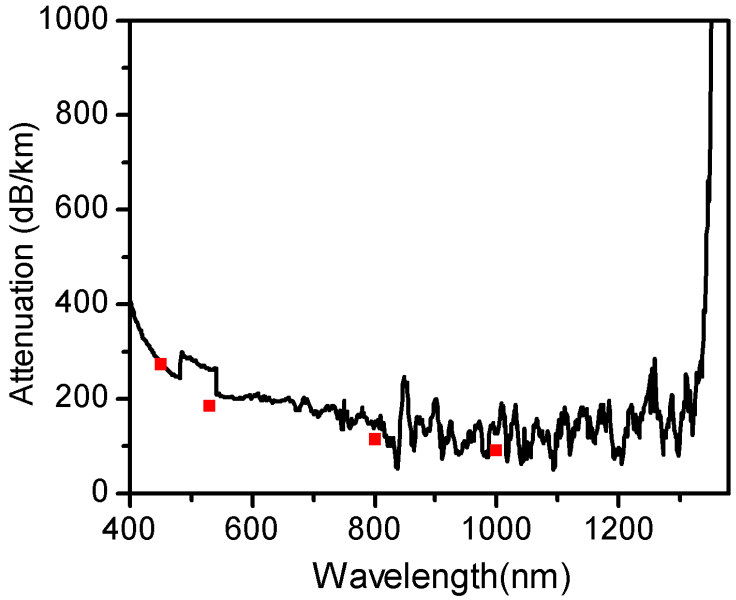

Fig. 5-8: Measured attenuation spectrum of the LP_{02} mode of PCF-SC-A. The points are more-reliable single-wavelength measurements

For comparison, a similar procedure was applied to get the loss of LP_{01} of this fibre. However, just the mode filter was needed in this case. The attenuation graph is plotted in Fig. 5-9.

Silica glass in general and silica fibres in particular show many attenuation features which are evident in the measurements of attenuation in Fig. 5-8 and Fig. 5-9 . Both of these two graphs show a rising attenuation in the short wavelength side arising from Rayleigh scattering in bulk silica and surface scattering at the edge of the core in this small core PCF [95]. Compared to LP_{01} mode, the attenuation of the LP_{02} mode of this fibre is much stronger because of the greater overlap of the LP_{02} mode with the core boundary, causing more surface scattering. The steep edge around 1350 nm in Fig. 5-8 is not the beginning of a

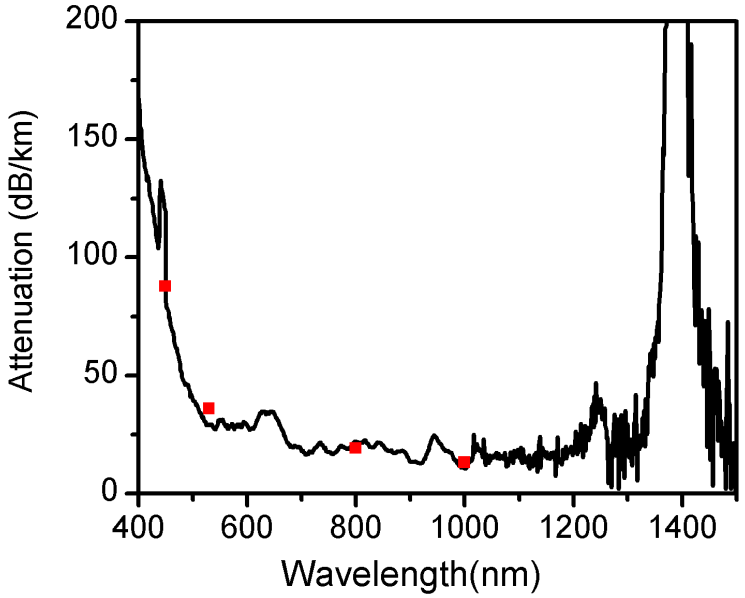

Fig. 5-9: Measured attenuation spectrum of the LP_{01} mode of PCF-SC-A. The points are more-reliable single-wavelength measurements

very strong O-H absorption but rather is due to cutoff of the LP_{02} mode. Conventional step-index fibres with germanium dopants in the core have a strong absorption edge at about 380 nm. This is absent in pure silica PCF and allows transmission at the short UV wavelengths. PCF-SC-A was fabricated without using drying or annealing techniques, and as a result exhibits a strong absorption close to 1380 nm due to vibrational excitations of O-H bonds in the silica [95], which can be seen in Fig. 5-9.

5.5 Converting back to LP_{01} mode

As discussed before, the LP_{01} mode is more useful than higher order modes, as most optical components are designed for this mode. After utilising the privileged properties of higher order modes, it is better to convert them back to the more useful fundamental mode. The conversion actually is straightforward: by letting the LP_{02} mode pass through another mode convertor whose structure is exactly the same as the first one but in the reverse direction. This part of the device is shown in the box area of Fig. 5-6. Simulation results confirm this conversion, which are shown in Fig. 5-10. For the wavelength of 532 nm the transmission loss was 0.0025 dB back to the LP_{01} mode after the second (reverse) mode convertor.

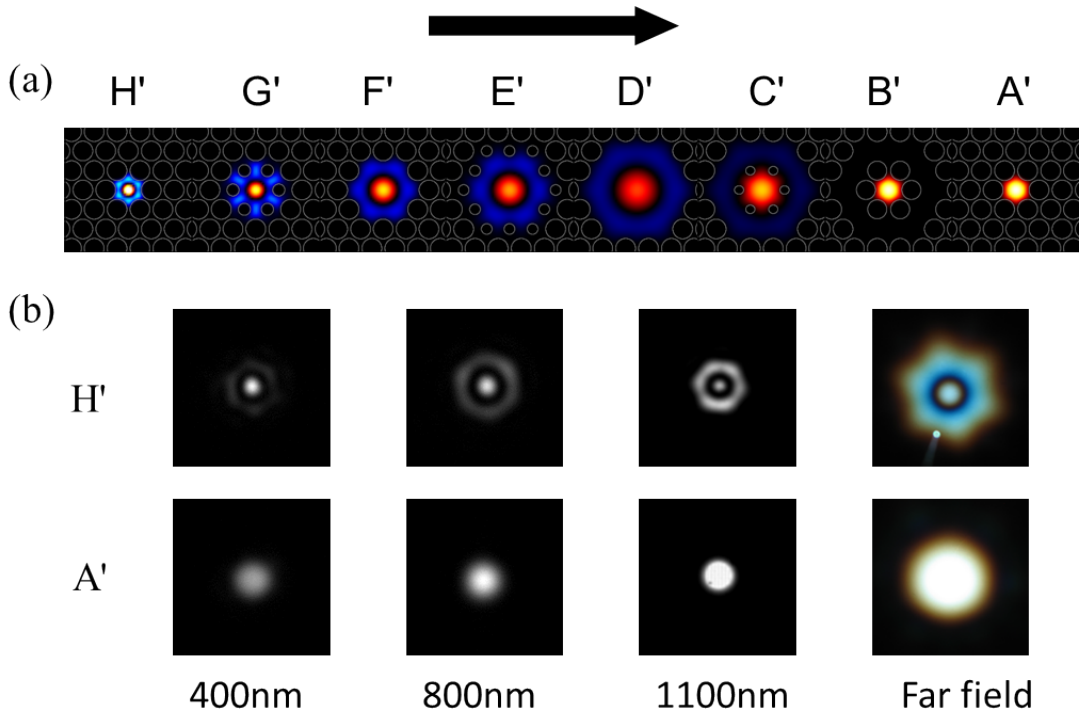

Fig. 5-10: The second MC converts the LP_{02} mode back to the LP_{01} mode. (a) is the simulation results. The arrow indicates the propagation direction of lights. (b) is similar to Fig. 5-7 (c-f) but the measured near field and far field mode patterns are shown just at the input and output of the MC (positions H′ and A′).

For the wavelength of 1000 nm the loss was 0.005 dB, illustrating not only the efficiency but also the broad wavelength range for this back conversion. It should be noted that a broad bandwidth is one of the essential properties of our mode convertors for the applications in Chapters 6 and 7.

5.6 Conclusions

By modifying the cladding structure of a PCF, the waveguide properties of this fibre can be changed. An abruptly generated parasitic core changes the mode order in the whole waveguide system, which allows mode conversion to happen. The symmetry of the system determines which type of modes will be converted to. In this way, by abruptly making an annular core, an all-fibre, low-loss, wavelength-independent LP_{01}-LP_{02} mode convertor was generated in a HNPCF. The remaining adiabatic structure allows this higher order mode to be squeezed into the fibre's original core. This LP_{02} mode can then be used for supercontinuum generation or specific wavelength generation through FWM. After passing

through a second, reversed mode convertor, the LP_{02} mode can be converted back to the fundamental LP_{01} mode.

Chapter 6

Supercontinuum generation in the LP_{02} mode

In Chapter 5, the way how an LP_{02} mode can be excited through an all-fibre, low-loss, broadband LP_{01}-LP_{02} mode convertor was investigated. The linear properties were also discussed. We now move to the nonlinear applications of this mode, focusing on UV and visible supercontinuum generation (this Chapter) and FWM (Chapter 7), taking advantage of its unique dispersion features.

6.1 Introduction

The nonlinear generation of new wavelengths of light in optical fibres is of great interest as an object of study and as a technology supporting many applications [96–99]. The introduction of glass-air PCFs greatly boosted the field, because the extraordinary control provided over chromatic dispersion permits phase matching and group-velocity matching at short wavelengths down to the visible [21, 53, 58, 100–105]. PCFs can also have a small tightly-confining core which enhances intensity for a given power. The most spectacular nonlinear interaction is supercontinuum generation, where short monochromatic pulses are converted into a spectrally broad output that is intense and in a single spatial mode, like a "white laser" beam.

Nearly all this effort has focused on just the Gaussian-like fundamental LP_{01}(or HE_{11}) mode. As mentioned in the last chapter, this is because its field distribution most closely resembles those of external light sources and systems (such as Gaussian laser beams, transmission fibres or spectrometers). This greatly simplifies input and output coupling. In contrast, special mode convertors are needed to

efficiently excite a higher-order mode and return the nonlinearly-generated wave back to the LP_{01} mode at the output. This second step in particular requires efficient broadband operation over an octave or more. Nonlinear propagation of higher modes in conventional fibres has been reported over a relatively narrow spectrum and without conversion back to the fundamental mode [99], using grating-based mode convertors that work over tens of nanometres at most [106]. In PCFs, previous studies of nonlinear propagation of higher-order modes (as distinct from nonlinear generation of higher-order modes from fundamental-mode or multimode light) used an offset launch to inefficiently generate an impure higher-order mode and also made no attempt to produce a fundamental mode output [21, 22, 107, 108].

However, higher-order modes have their own desirable properties for nonlinear propagation [21–23]. We show here that the LP_{02} (or HE_{12}) "Mexican sombrero" mode has dispersion spectra with valuable features unobtainable with the LP_{01} mode. Intense light in these modes can generate much shorter wavelengths - in principle down to 240 nm compared with 305 nm. To show how this can be realised experimentally, we made mode convertors, as discussed in the last chapter, to make an input LP_{01} wave to evolve into an output LP_{02} mode in the same waveguide, and vice versa. In this way we could generate a supercontinuum in the LP_{02} mode, and couple it back into the more-useful LP_{01} mode over the full octave wavelength range of the supercontinuum.

6.2 Theoretical analysis

Supercontinuum generation depends on the dispersion properties of the medium. Schematic spectra of group delay (the reciprocal of group velocity) and group velocity dispersion (the wavelength derivative of group delay) are plotted in Fig. 6-1. The dispersion has two zeros (and the group delay two local extrema), at the zero-dispersion wavelengths ZDW1 and ZDW2. A third key wavelength is the matching wavelength MW, shorter than ZDW1, at which the group delay matches that at ZDW2.

Generally speaking, the broadest supercontinuum is generated by input pump light (from a pulsed laser for example) with a wavelength close to but slightly greater than ZDW1 [14, 49, 56, 109]. Given enough power and fibre length, Kerr and Raman nonlinearity broaden the light wave into a supercontinuum filling the spectrum between MW and ZDW2. These wavelengths, deduced from

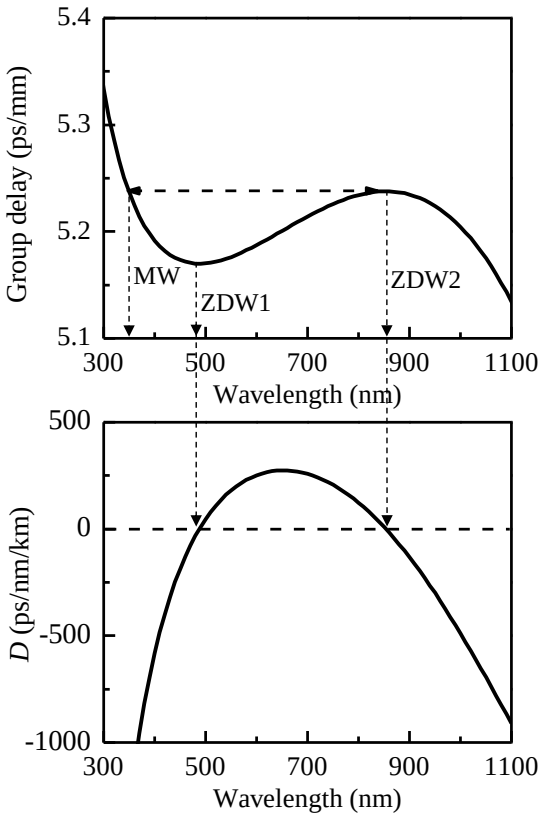

Fig. 6-1: Schematic group delay (upper) and dispersion spectra (lower), indicating the zero dispersion wavelengths ZDW1 and ZDW2 and the matching wavelength MW.

the group delay plot, therefore delimit the attainable supercontinuum spectrum [110]. In detail, the pump light forms one or more optical solitons because the dispersion is anomalous (ie, positive D, negative β_2) there. As it propagates, the soliton undergoes self frequency shifting to longer wavelengths, trapping a so-called dispersive wave at the wavelength shorter than ZDW1 for which the group delay matches the group delay at the soliton wavelength. As each soliton moves to longer wavelength under the soliton self-frequency shift, the trapped dispersive wave is shifted to shorter wavelength to maintain the group delay match [56]. With many solitons created differently (and so shifting to different extents) by different pump pulses, on averaging over many pulses the whole spectrum between these two wavelengths is therefore filled with light - a supercontinuum.

This process continues until the soliton can no longer propagate. Given strong-enough input power and a long-enough fibre, and if the fibre is low-loss for all wavelengths between ZDW1 and ZDW2, this happens when the soliton wavelength reaches ZDW2. The soliton cannot shift further because the disper-

sion becomes normal (ie, negative D) beyond ZDW2, anomalous dispersion being necessary for soliton propagation. The matching wavelength MW (shorter than ZDW1) where the group delay matches that at ZDW2 is therefore the shortest possible wavelength in the supercontinuum.

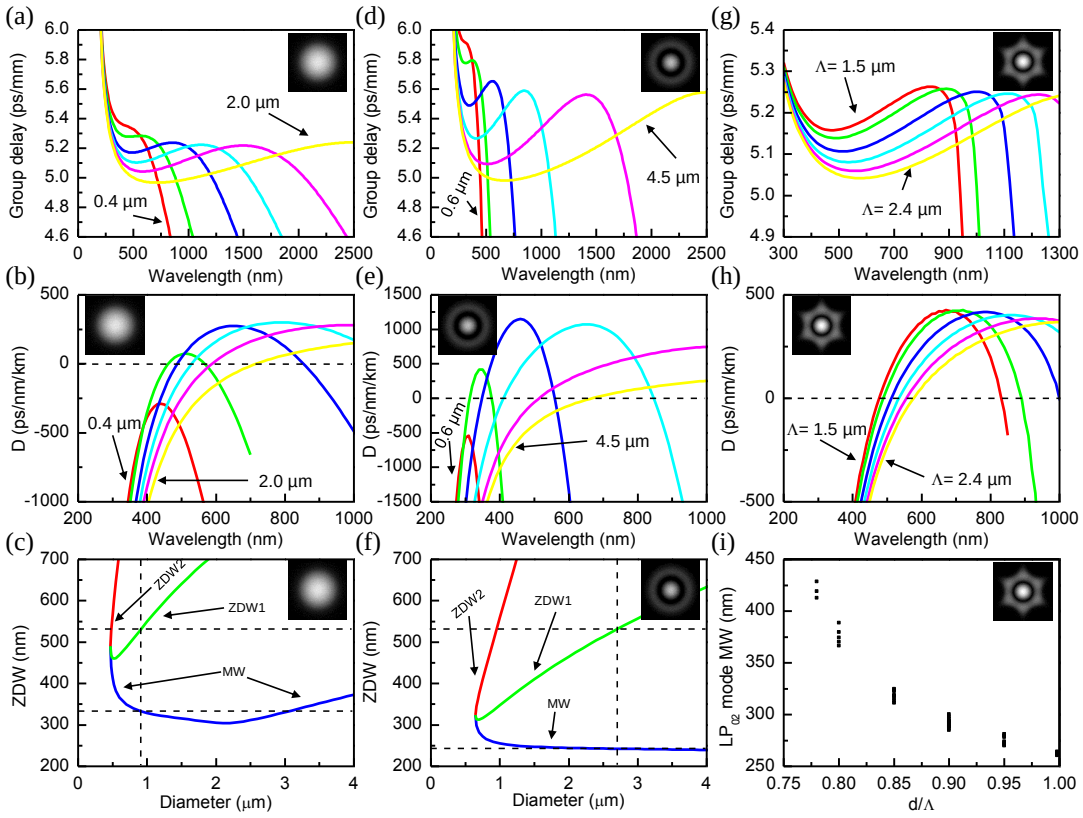

Fig. 6-2: Dispersion behaviour of microwires and PCFs. Calculated group delay (a) and dispersion (b) spectra for the LP_{01} mode of a microwire, for (left to right) diameters of 0.4, 0.5, 0.7, 0.9, 1.2 and 2.0 μm. (c) Variations of key LP_{01} mode dispersion wavelengths with microwire diameter. The diameter corresponding to ZDW1= 532 nm, and the corresponding MW, are indicated. (d-f) as (a-c) but for the LP_{02} mode and respective diameters 0.6, 0.7, 1.0, 1.5, 2.5 and 4.5 μm. (g-h) as (a-b) but for the LP_{02} mode of a PCF with $d/\Lambda = 0.85$ and (left to right) Λ = 1.5, 1.6, 1.8, 2.0, 2.2 and 2.4 μm. (i) MW versus d/Λ for the LP_{02} mode of PCFs with various values of Λ.

Alternatively, if the fibre attenuation becomes large at some wavelength λ between ZDW1 and ZDW2, the soliton is attenuated too much to remain as a soliton when it reaches λ. In this case MW is the short wavelength that matches the group delay at λ rather than at ZDW2. For silica fibres we will take $\lambda =$ 2500 nm [111], though loss due to hydroxyl in the glass can create such an attenuation barrier at $\lambda \approx 1400$ nm.

A convenient model for calculating dispersion is a silica microwire - a cylindrical thread of silica glass surrounded by air [112, 113]. This accurately represents a conventional tapered fibre waist [10, 112] and approximates an extreme PCF with large d/Λ, where it yields a lower bound on MW. Group delay and related dispersion spectra for the fundamental LP_{01} mode of microwires at series of diameters are plotted in Fig. 6-2(a-b). Fig. 6-2(c) is a plot of the key wavelengths (ZDW1, ZDW2, MW) versus microwire diameter. The minimum possible ZDW1 and MW are 460 nm and 304 nm respectively, and a diameter near 0.9 μm is needed to match ZDW1 to the 532 nm wavelength of a frequency-doubled Nd:YAG laser. Such small cores complicate input coupling and are susceptible to damage and nonlinear losses, limiting the supercontinuum power [10].

The calculations are repeated in Fig. 6-2(d-f) for the "sombrero" LP_{02} mode. The features are broadly similar but with larger overall values for group delay and dispersion [114]. Particular ZDW1 and MW values occur for bigger diameters. For example, a diameter of 2.7 μm matches ZDW1 to 532 nm. More significantly, however, ZDW1 and MW themselves are much shorter. The case where ZDW1 = 532 nm gives MW = 243 nm (instead of 333 nm for LP_{01}), and the minimum possible ZDW1 and MW are now 312 nm and 238 nm respectively. The shortest possible supercontinuum wavelength is therefore over 60 nm shorter for the LP_{02} mode than for the LP_{01} mode, and the shortest wavelength for a 532 nm pump laser is 90 nm shorter. These are large differences for ultraviolet light.

The calculated group delay, dispersion and MW for the LP_{02} mode of some silica-air PCFs are plotted in Fig. 6-2(g-i). These confirm the validity of the microwire as a limiting model for the PCF for large values of d/Λ.

It is notable that the local maximum group delay for a given mode in a given fibre structure (a silica microwire, or a PCF with a given d/Λ) is insensitive to the wavelength ZDW2 at which the maximum occurs, even though ZDW2 itself varies strongly with the scale of the fibre (the diameter of a microwire, or the hole pitch Λ of a PCF). This is clearer in plots of peak group delay (by definition at ZDW2) versus ZDW2, Fig. 6-3(a) , and can be explained by considering the group delay in the absence of material dispersion. A fibre with a transverse index distribution characterised by a length scale L has a mode whose propagation constant varies with frequency ω_0 as $\beta_0(\omega_0)$. Its group delay is

$$\beta_{1,0}(\omega_0) = \frac{d\beta_0}{d\omega_0} \tag{6.1}$$

By length scaling invariance [115], a fibre with the same index distribution but with a transverse scale of αL (ie, dilated by factor α) must support the same mode with propagation constant $\beta(\omega) = \beta_0(\omega_0)/\alpha$ at frequency $\omega = \omega_0/\alpha$, since the refractive indices do not depend on frequency in the absence of material dispersion. The group delay is now

$$\beta_1(\omega) = \frac{d\beta}{d\omega} = \frac{1}{\alpha}\frac{d\beta_0}{d\omega_0}\frac{d\omega_0}{d\omega} = \beta_{1,0}(\omega_0) = \beta_{1,0}(\alpha\omega) \tag{6.2}$$

The group delay curve for the scaled fibre is therefore the same as that for the unscaled fibre but compressed by the scaling factor α along the ω axis (or, stretched by α along a wavelength axis). Thus in the absence of material dispersion the peak group delay is a constant for a given mode in a given fibre structure, and ZDW2 is proportional to the scale.

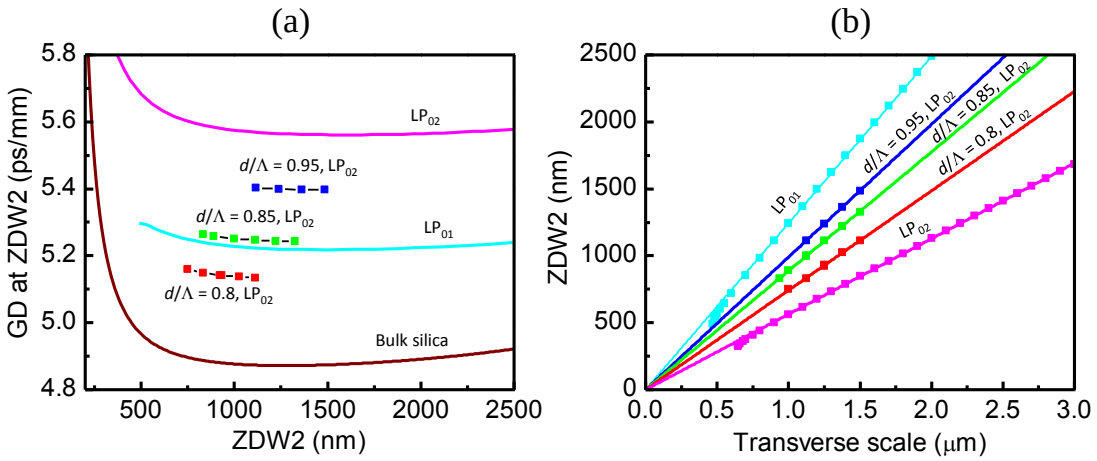

Fig. 6-3: Relationships between key dispersion parameters. (a) Group delay(GD) at ZDW2 versus ZDW2 (as varied by changing the scale of a given design of fibre), for the LP_{01} and LP_{02} modes of a microwire and (points) for the LP_{02} modes of PCFs with three values of d/Λ. The group delay in bulk silica is also plotted. (b) ZDW2 versus transverse scale for the same fibres as (a) (points), together with fits to straight lines through the origin. The transverse scale is the diameter for microwires and $\Lambda/1.6$ for the PCFs: the factor of 1.6 is chosen simply to avoid overlapping the microwire data. All results include the effects of material dispersion.

Fig. 6-3 shows that this behaviour remains approximately true even if material dispersion is not neglected. This is because, for wavelengths longer than about 500 nm, the group delay of bulk silica varies very little compared to its difference from the group delay of the guided modes of interest. On the other hand, the material group delay rises very rapidly for shorter wavelengths, and comes to

dominate the group delay of the modes too. Thus the value of group delay at ZDW2 is attained for similar short wavelengths MW regardless of the scale of the fibre, which explains why MW is so insensitive to the scale of a given design of fibre. However, when material properties are considered it is possible that ZDW2 is unattainable due to attenuation. In this case one must consider dispersive waves matched to a fixed IR absorption wavelength, and MW then does vary with fibre scale [109, 111].

Although MW is generally insensitive to fibre scale for both LP_{01} and LP_{02} modes, the local maximum group delay value for LP_{02} mode is larger than that of LP_{01} mode, which means the matching wavelength for LP_{02} mode is in the steeper region of the group delay curve when compare to that of LP_{01} mode. This gives another interesting property: MW for the LP_{02} mode varies even less with scale (microwire diameter or PCF Λ) and hence with ZDW1 compared to the LP_{01} mode, so a wide range of alternative pump sources will give very similar minimum possible supercontinuum wavelengths. In contrast, for the fundamental LP_{01} mode the minimum possible wavelength is only available for particular pump wavelengths or by using non-uniform fibres to vary dispersion with distance [102, 109, 110].

6.3 PCF fabrication and dispersion properties

In order to get suitable fibres for supercontinuum generation, two solid core PCFs were fabricated by the stack-and-draw technique from a common preform. They were designed to have the LP_{02} mode ZDW1 slightly less than the intended pump wavelength of 532 nm. Fig. 6-4 shows a SEM image of fibre PCF-SC-A. Fibre PCF-SC-B was only slightly different, but allowed us to explore the detailed effects of dispersion changes and to validate our simulations of the fibres. Further details are provided in Table 1. The measured parameters were also used for mode convertor simulation in Chapter 5.

The measured ZDW1 of the LP_{01} modes of fibres PCF-SC-A and PCF-SC-B were 789 and 777 nm respectively. It is not simple to measure the dispersion spectra of higher-order modes [23] so we calculated them from SEM measurements of the fibre cross-sections. The calculated LP_{01} mode ZDW1 matched the measured values to within a nanometre, and the calculated LP_{02} mode ZDW1 were 527 and 515 nm respectively. Although SEM measurements of PCF dimensions suffer from uncertainties in calibration and in locating hole boundaries, we found

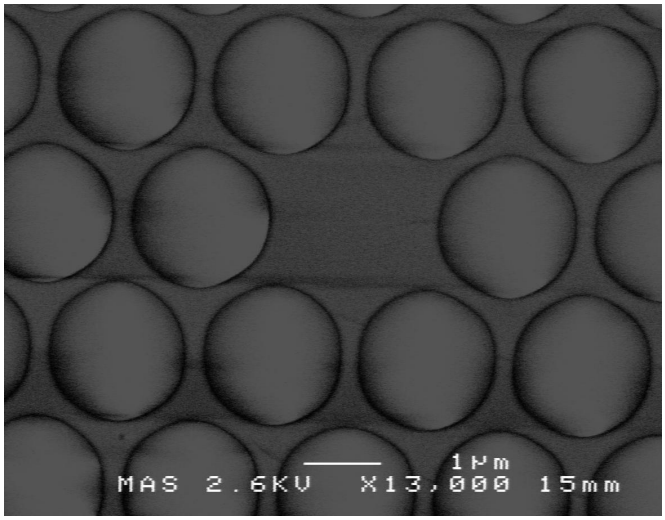

Fig. 6-4: A SEM image of fibre PCF-SC-A.

Table 6.1: Parameters of PCF-SC-A and PCF-SC-B

	Fibre PCF-SC-A	Fibre PCF-SC-B
Pitch,$\Lambda(\mu m)$	2.09 ± 0.02	2.05 ± 0.02
Diameter of core(μm)	2.25 ± 0.02	2.13 ± 0.02
Diameter of holes, $d(\mu m)$	1.86 ± 0.03	1.86 ± 0.03
d/Λ	0.89 ± 0.017	0.91 ± 0.017
Outer diameter(μm)	130 ± 0.3	125 ± 0.3

that ZDW1 values for the LP_{02} and LP_{01} modes are closely correlated even for widely different PCFs, which is shown in Fig. 6-5(c): they broadly have a linear relationship. We therefore have confidence in the simulated values for LP_{02} mode ZDW1, given the accuracy of the LP_{01} values, even if the SEM measurements are inaccurate: even without simulating the structure from the SEM, the measured ZDW1 for LP_{01} determines the ZDW1 for LP_{02} to within ± 5 nm.

6.4 Experiment setup

Using the method discussed in Chapter 5, several mode convertors were made in fibres PCF-SC-A and PCF-SC-B to study higher-order mode supercontinuum generation in detail. In order to avoid nonlinear effects happening before light been converted to the desired LP_{02} mode when pumped by a high power laser, the fibre length before a mode convertor was kept as short as possible. The typical length of a device, including MF, MC and fibre before and between them, was less than 20 cm. The fibre length after a MC was chosen to be several

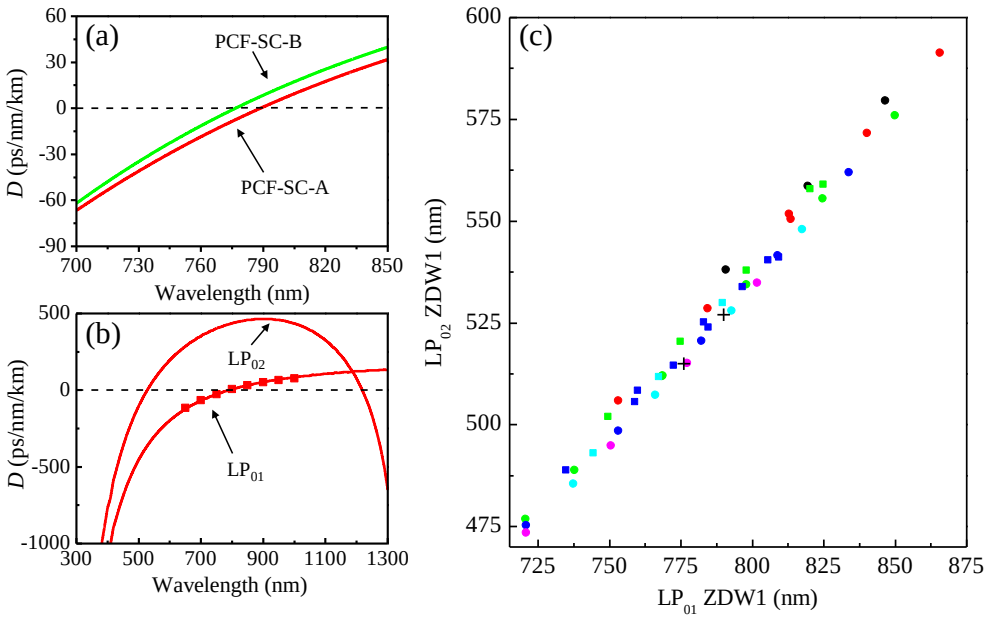

Fig. 6-5: (a) Measured dispersion spectra for the LP_{01} mode of fibres PCF-SC-A and PCF-SC-B. (b) Simulated LP_{01} and LP_{02} mode dispersion spectra for fibre PCF-SC-A. The points are measured LP_{01} values from (a). (c) Calculated relation between LP_{02} ZDW1 and LP_{01} ZDW1 for PCFs with differing Λ, d/Λ and distortions of the innermost holes. Round points are undistorted, square points have distortions. Relative hole size d/Λ= 0.78 (black), 0.80 (red), 0.85 (green), 0.90 (blue), 0.95 (cyan), 0.998 (magenta). All points lie on roughly the same straight line. Fibres PCF-SC-A and PCF-SC-B used for the experiments described in this chapter are marked by crosses.

metres. This length is a good balance between nonlinearity and loss. All nonlinear effects have been fully developed while the generated LP_{02} mode supercontinuum is not attenuated too much. For clarity, if not stated otherwise, fibre lengths mentioned in the remainder of this chapter specifically mean the length after a mode convertor.

A frequency-doubled Nd:YAG microchip laser (Teem Photonics, NG-10320-000) was used as a pump source. This common, efficient, rugged and low-cost light source emits 0.6 ns pulses of light of 532 nm wavelength with a repetition rate of 7.0 kHz and an average power of 24 mW. In order to get a high coupling efficiency, an aspheric lens (Newport 5723-H-A) was used. A neutral density filter was used to vary the input power level to avoid damage to the fibre core. Coupling efficiencies of $\sim$30% were achieved experimentally. An optical spectrum analyser (Ando AQ-6315B) was used to measure the supercontinuum spectra from 350 to 1750 nm. The step in the spectra at 600 nm is a calibration artifact of the

spectrum analyser at a change of order-sorting filter. The UV range of spectra was determined using a UV spectrometer (Bentham DTMc300). CCD cameras and grating were used to check the output near and far field mode patterns.

6.5 Results

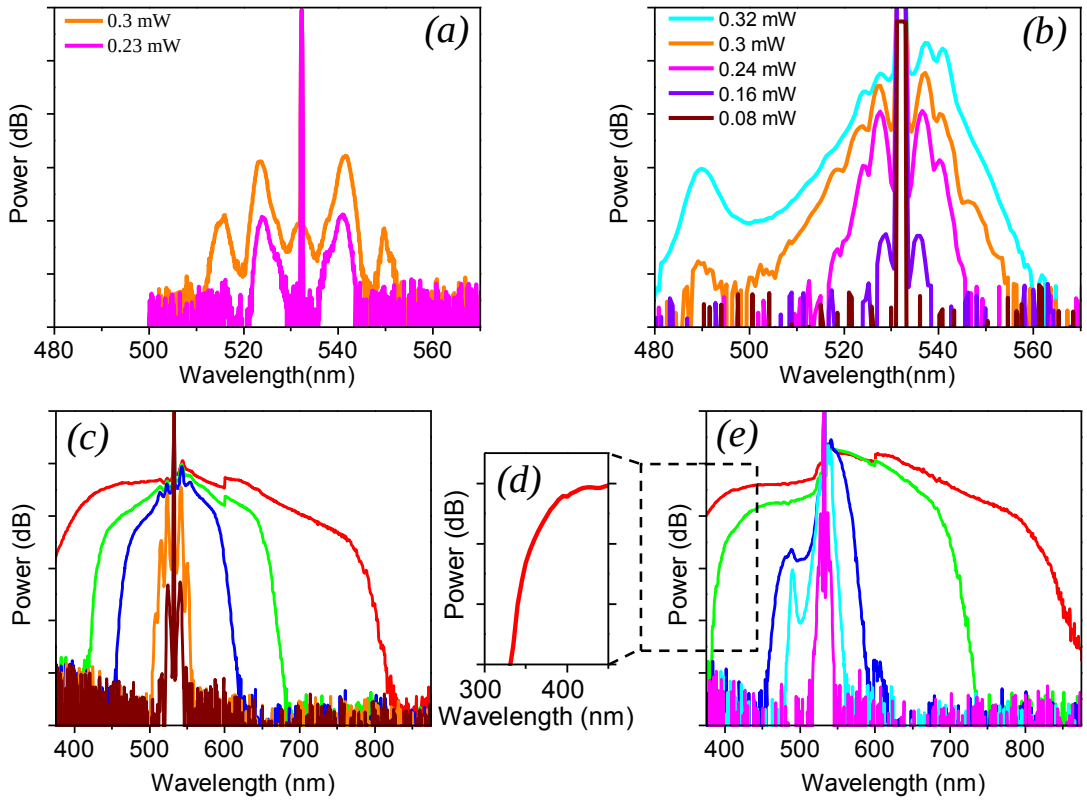

Fig. 6-6: (a,b) Low power LP_{02} output spectra for 1.8 m of PCF-SC-A and PCF-SC-B respectively, with MI sidebands in both fibers and a dispersive wave at 490 nm for PCF-SC-B. (c,e) As (a,b) for higher output powers leading to supercontinuum (outer to inner traces) of (c) 1.9, 1.1, 0.60, 0.30, and 0.19 mW and (e) fiber 2 at 1.9, 1.2, 0.49, 0.32, and 0.24 mW. (d) The UV end of spectrum (e) for 1.9 mW. Vertical scales 10 dB per division, resolutions (a) 0.2 nm, (b,c,e) 2 nm, (d) 5 nm.

Fig. 6-6 shows supercontinuum spectra for 1.8 m of LP_{02} mode propagation along PCF-SC-A and PCF-SC-B. At low power, Fig. 6-6 (a) and (b), both show the sidebands of modulation instability, then followed by broad continuum generation at higher powers, Fig. 6-6 (c-e).

The simulated LP_{02} mode ZDW1 for fibre PCF-SC-A is 527 nm, slightly shorter than 532 nm, and the presence of MI sidebands confirm that dispersion is

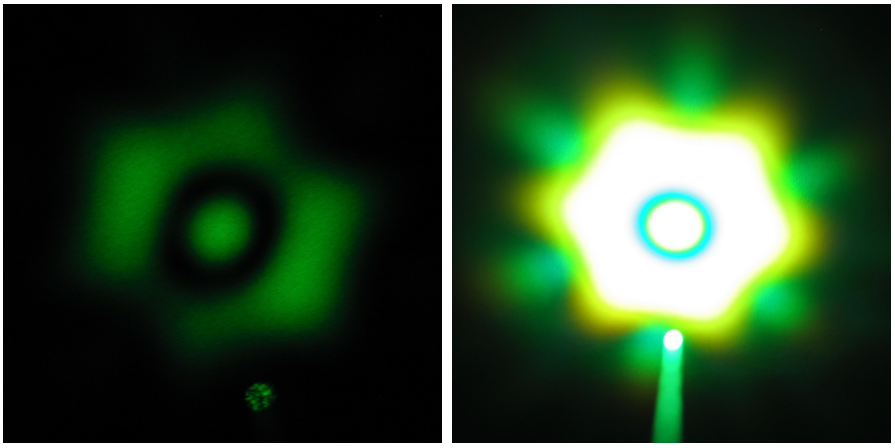

(a) (b)

Fig. 6-7: Far field mode patterns for lower(a) and high(b) output powers with 1.8 m PCF-SC-A. Not the same scale.

indeed anomalous at the pump wavelength [37]. The LP_{02} mode ZDW1 of fibre PCF-SC-B should be shorter (515 nm) and measurements show more closely-spaced MI sidebands and a phase-matched dispersive wave [55, 116, 117] below ZDW1 at 490 nm. From the wavelengths of the MI sidebands and the measured pump powers (assuming gaussian pulse shapes) we estimate the dispersion at 532 nm to be $\sim$ 30 and $\sim$ 125 ps/nm/km in fibres PCF-SC-A and PCF-SC-B respectively, using calculated values for the effective area of the LP_{02} mode and Chapter 5 of [37]. These compare with the simulated values of $\sim$ 15 and $\sim$ 60 ps/nm/km: the same ratio but different absolute values, probably due to common scale factors such as the conversion from average power to peak intensity. The simulated dispersion of fibre PCF-SC-B predicts a phase-matched dispersive wave at 483 nm, which is evident in Fig. 6-6 (b) and (e). In both fibres the output spectra extend below 375 nm for the maximum available power, and that of fibre PCF-SC-B extends to 330 nm, the extended part of Fig. 6-6 (e). The output powers were higher and the devices considerably more durable than in previous experiments using the same 532 nm pump laser for the LP_{01} mode, which required submicron core diameters [10]. The output pattern was a clear LP_{02} mode in all cases, which is shown in Fig. 6-7 for low and high output powers in fibre PCF-SC-A.

Shortening the fibres yielded similar behaviour with reduced bandwidth, Fig 6-8. With just 10 cm of fibre PCF-SC-A we observed no broadening at all except output power exceeding 3 mW, when we saw weak MI sidebands resembling those

in Fig. 6-6(a). This confirmed that broadening was insignificant before the LP_{02} mode was generated.

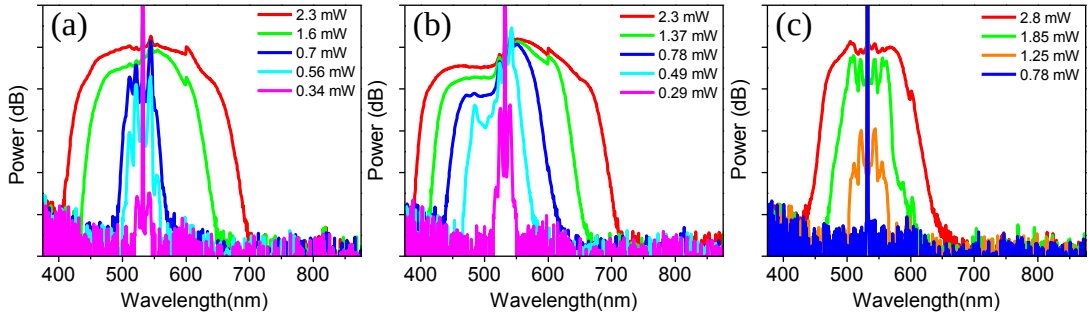

Fig. 6-8: (a,b) Measured supercontinuum spectra in the LP_{02} mode for 0.8 m of fibers PCF-SC-A and PCF-SC-B respectively. (c) Corresponding spectra for 0.3 m of PCF-SC-A. Vertical scales 10 dB per division, resolution 2 nm.

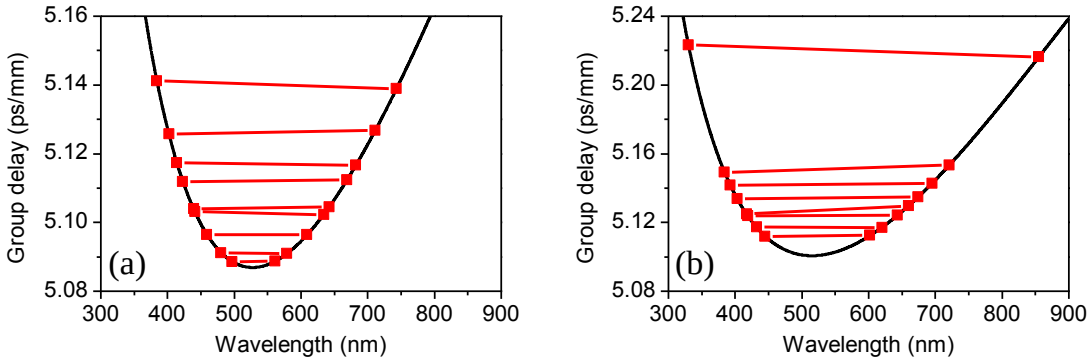

Fig. 6-9: Group index matching in measured supercontinuum spectra. Group delay for the longest and shortest wavelengths of supercontinua generated in fibre PCF-SC-A (a) and PCF-SC-B (b) for a range of fibre lengths and output powers.

The shortest wavelength obtained in our experiments was around 320 nm. This is longer than the minimum wavelength predicted in Fig. 6-2, because of the limited available pump power. Nevertheless, at all power levels and for various fibre lengths the calculated group delay of the longest wavelength generated closely matches that of the shortest wavelength, as shown in Fig. 6-9. Data are included for all traces where the power was high enough for soliton self-frequency shifting to be established, and for which the UV edge of the continuum was measured reliably. The group delay at these measured wavelengths is taken from simulations of the fibres. There is a somewhat arbitrary decision to be made about the power level which defines the edges of the supercontinuum, but different choices

do not make a qualitative difference to the form of Fig. 6-9. It is clear that the edges of the supercontinuum spectra are indeed closely matched in group delay as expected [56, 111]. The lines joining the group delay of the short and long wavelengths are close to, although not quite, horizontal. However the group delay curve is so steep at short wavelengths that a change of just a few nanometres is enough to match the long-wavelength group delay exactly.

6.6 Fundamental mode output

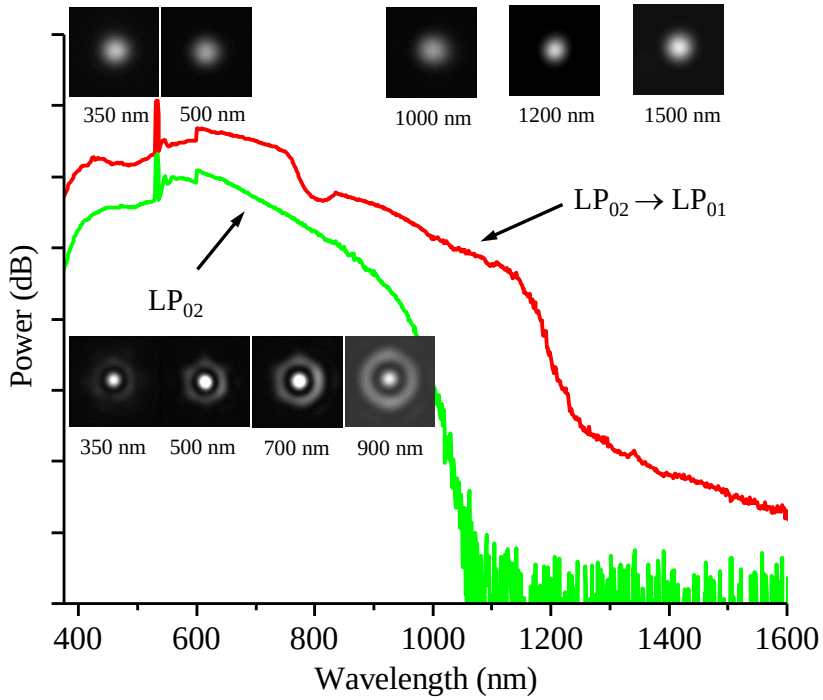

Fig. 6-10: Output spectra and selected near-field patterns for supercontinuum generated in 4 m of fibre between the two mode convertors, measured before and after the second mode convertor was cut away. The vertical offset of the traces is due to arbitrarily-different coupling into the spectrum analyser. The total power in the LP_{02} spectrum (1.60 mW) is slightly greater than that in the LP_{01} spectrum (1.55 mW). Vertical scale 10 dB per division, resolution 5 nm.

We have demonstrated supercontinuum generation in a higher order mode (LP_{02}). Further study was carried out to convert the generated light back into the more-useful LP_{01} mode. The feasibility of back conversion was investigated in the last chapter: a second mode converter is needed. An essential property of this mode converter is that it must be broadband across the whole supercontinuum spectrum spanning more than one octave. We therefore made another device

with fibre PCF-SC-A to demonstrate this. This device has a second, reversed, mode convertor at the end of the previous structure, with 4 m of unprocessed fibre between the mode convertors and 0.9 m of fibre beyond the second one. Supercontinuum spectra generated in the LP_{02} mode (before the second mode convertor) but output in the LP_{01} mode (after that second mode convertor and another 90 cm propagation in fibre PCF-SC-A) are plotted in Fig. 6-10. The whole spectrum was efficiently converted into the fundamental mode. However, the supercontinuum continued to evolve in the final 90 cm of fibre, showing that nonlinear processes continue for the high-intensity broadband light now propagating in the LP_{01} mode. This mode has a measured ZDW1 of 789 nm, and intense light at this wavelength can generate further supercontinuum. In Fig. 6-10 we can see a spectral notch around 800 nm, where light is converted from wavelengths around ZDW1 to longer and shorter wavelengths.

6.7 Induced loss mechanism

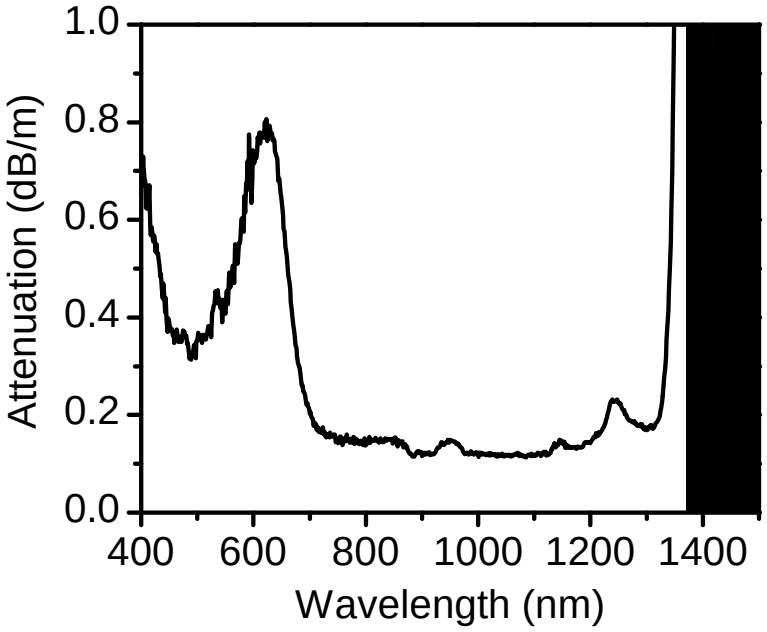

Fig. 6-11: Measured attenuation spectrum of the LP_{02} mode of fibre PCF-SC-A after exposed to strong UV light.

After supercontinuum generation, the loss of fibre PCF-SC-A in the LP_{02} mode was tested again to check for any difference caused by strong UV light generation and propagation. The attenuation spectrum is shown in Fig. 6-11.

Compared to loss spectrum measured in a fresh fibre, Fig. 5-8 of last chapter, there are some significant changes. The loss for short wavelength range has significantly increased, while that in long wavelength range have remained nearly constant. The other main feature is that a defect absorption, identified as a non-bridging oxygen hole centre (NBOHC) [118], appears at 630 nm. This is sometimes known as a drawing band as the defects can be created during the process of fibre drawing [95]. In this case it is not caused during drawing as it is not present in the measurements of fresh fibre (for both LP_{01} and LP_{02} modes). The real reason is the intensive UV light generated by supercontinuum generation in the fibre. It is known that pulses of intense UV light can cause NBOHCs and resultant photodarkening at 630 nm [119]. Effective techniques to reduce photodarkening in optical fibres include hydrogen or deuterium loading [120] which terminates the NBOHCs as O-H or (O-D). The subsequent infrared absorption does not overlap with the wavelengths of interest here.

6.8 Conclusions

We have explored the benefits of extending nonlinear fibre optics to higher-order modes, and implemented a complete experimental scheme to realise these benefits using all-fibre mode convertors that are non-resonant, broadband and low-loss. We described one example, supercontinuum generation in the LP_{02} mode of a PCF, in experiments where both input and output waves can be in the fundamental mode. The dispersion properties of the LP_{02} mode, and hence its nonlinear behaviour, are broadly similar to those of the fundamental mode. However, the key dispersion wavelengths are considerably shorter and occur for larger cores. Higher modes therefore allow the generation of shorter-wavelength UV light from shorter-wavelength pump sources in fibres that are more damage-resistant and easier to couple into.

The work described is important for applications requiring visible or ultraviolet continuum, such as fluorescence microscopy. Most systems, stains and markers are designed for visible light, and many biological structures exhibit signature autofluorescence from UV excitation. Despite the availability of efficient and rugged 532 nm lasers, current visible supercontinuum sources use infrared pump lasers emitting the much-longer wavelengths of 800 or 1064 nm. A major reason for this is because fibres with the appropriate dispersion for 532 nm pumping have very small submicron-diameter cores. These present input cou-

pling difficulties and are susceptible to damage and nonlinear losses at modest input power, limiting the supercontinuum power. In contrast, zero-dispersion wavelengths as short as 310 nm are possible with the LP_{02} mode (compared to 460 nm for LP_{01}), with a short-wavelength bound on the supercontinuum spectrum down to 240 nm (compared to 305 nm for LP_{01}). These desirable properties can be achieved for core diameters as big as 2.6 μm.

This is just one example of the way higher-modes provide new dispersion properties to be exploited for nonlinear interactions. Other examples include the combination of higher-mode and fundamental-mode interactions at different locations along the fibre, briefly shown in Fig. 6-10, and the generation of discrete short wavelengths by four-wave mixing in fibres with normal dispersion[121], which will be discussed in next chapter.

Chapter 7

Four wave mixing in the LP_{02} mode

In the last chapter, we investigated the benefits of using higher order modes for nonlinear applications. In particular, we chose supercontiuum generation as an example to demonstrate how higher-order modes can enhance this spectral broadening process in the blue and UV range. In this chapter, we discuss how higher-order modes can be used for discrete new wavelength generation via four wave mixing, especially in UV range. All of these become possible as a result of controllability (hole control) over the cladding structure of a PCF.

7.1 Introduction

Supercontinuum generation has been in vogue since the advent of PCFs. SC sources with spectra spanning more than 2 octaves are already commercially available [122], and can cover the whole visible and near IR region. However, in some situations, light at specific wavelengths is more important than broad bandwidth. For example, for dense wavelength division multiplexing (DWDM) wavelengths around 1550 nm are more favourable [123], while light sources in the blue and ultra violet (UV) region are valuable for applications like fluorescence microscopy. Furthermore, if one wants to generate intense narrowband laser-like light waves, one would probably avoid any kind of spectral broadening. Four wave mixing (FWM) is a well known technique to create such narrowband light at new wavelengths which are not in practice available from conventional lasers.

FWM, as mentioned in Chapter 1, is a well-known nonlinear effect arising from the third order susceptibility of a material, and can be observed in silica

optical fibres. Although it has been demonstrated in conventional fibres, like standard telecommunication fibres [124, 125] and dispersion shifted fibres [126], the relative weak controllability over waveguide dispersion makes the phase matching condition difficult to fulfill for commonly available laser sources. It is only possible to observe FWM if the pump and signal wavelengths are in the low dispersion region (very close to a fibre's ZDW), which is around 1.3 μm for standard telecommunication fibres and 1.55 μm for dispersion shifted fibres [124–126]. In other wavelength ranges, higher order dispersion terms are too small (when compared with β_2) to be accounted for in the phase matching calculation [127]. This leaded to the conclusion that there was no parametric four wave mixing gain in the normal dispersion region of a single mode optical fibre and this assumption was widely accepted in fibre optics community before the advent of PCFs [37]. For short wavelength generation, alternative methods were used, among which intermodal four wave mixing was a useful solution if a few mode fibre was used [128, 129]. However, special care over fibre design was needed to exploit the phase matching between different modes.

This was greatly helped by the control over nonlinearity and dispersion that is provided by PCFs [127]. Since Harvey et al. first reported well-separated FWM peaks in PCFs [130], FWM has been used for supercontinuum generation and high-power red and near-infrared sources [53, 54, 131, 132]. However, generation of discrete new wavelengths in the blue and UV range remains difficult with long-wavelength pump sources. FWM clearly cannot generate wavelengths shorter than half the pump wavelength, so UV generation requires a pump in the green or blue. For fibre FWM to generate discrete peaks widely separated from the pump, the pump wavelength must be shorter than, but close to, the zero dispersion wavelength (ZDW). In PCF the ZDW is shortest when the holes are large, and in that case is determined mainly by the core diameter. A core diameter of around 0.9 μm is needed for a ZDW of 532 nm in the fundamental mode [133]. However, PCFs with such a small core are difficult to draw and are susceptible to high loss and two-photon absorption and damage at high powers. This limits the shortest wavelength obtainable by FWM.

The enhanced waveguide dispersion of higher-order modes gives short ZDWs even with relatively large cores. For example, a core diameter of 2.7 μm gives a ZDW of 532 nm for the LP_{02} mode [133]. FWM in higher-order modes not only permits the use of 532 nm pump light in robust structures, but the shape of the dispersion curves makes it easier to target a particular pump and signal

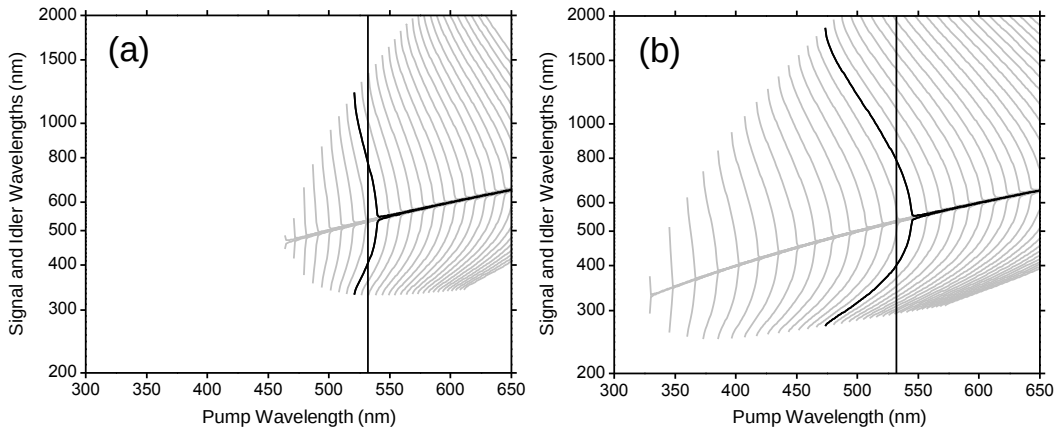

Fig. 7-1: Calculated phasematching curves for (a) the HE_{11} (LP_{01}) mode and (b) the HE_{12} (LP_{02}) mode of a strand of silica in air, giving the signal and idler wavelengths as functions of pump wavelength for particular diameters. The thicker curves are for diameters of (a) 0.952 μm and (b) 2.86 μm, in each case chosen to generate 400 nm and 800 nm light for a 532 nm pump. The thinner curves are for increments of 5% diameter of the thick curves, increasing from left to right (0.571 to 1.90 μm in (a) and 0.858 to 5.72 μm in (b)).

wavelength. Fig. 7-1 shows the calculated phasematching wavelengths as a function of pump wavelength for a range of different PCFs, approximated as strands of silica entirely surrounded by air. In the regime of visible wavelength pumping, the FWM wavelengths for the LP_{01} mode are a much stronger function of both pump wavelength and of fibre core diameter (even fraction change in core diameter) than for the LP_{02} mode. It is therefore very difficult experimentally to achieve a combination of fibre and pump wavelength which give rise to FWM (rather than supercontinuum[10]), and FWM in the LP_{01} mode in this regime has not been demonstrated. As well as being less sensitive to pump wavelength and relative diameter, FWM in the LP_{02} mode also offers the opportunity to use shorter pump wavelengths, and for a given pump wavelength offers shorter signal wavelengths.

In this chapter we discuss FWM entirely within the LP_{02} mode of three few-mode PCFs. When pumped with 532 nm light in the LP_{02} mode (converted from the LP_{01} mode, as demonstrated in Chapter 5) of these fibres, FWM peaks were seen at UV (signal) and near-IR (idler) wavelengths, all outputs also being in the LP_{02} mode. If necessary, all three light waves can be converted back to the fundamental mode by a reversed mode convertor at the output [133].

7.2 Phase matching and experimental conditions

Three fibres (PCF-FWM-A, PCF-FWM-B and PCF-FWM-C) were drawn from a common preform and had similar structures but slightly different core sizes. The cane used here and the one used for LP_{02} mode SC generation in the previous chapter were drawn from the same stack. Fig.7-2 (a) is an SEM image of fibre PCF-FWM-B. The dimensions of fibre structures were measured from high resolution SEM images. The plane wave method [52] was then applied to calculate the propagation constants and related dispersion curves for the LP_{02} mode of these fibres, which are shown in Fig.7-3 (b). These curves are very similar but with ZDWs at 545 nm, 550 nm and 567 nm for PCF-FWM-A, PCF-FWM-B and PCF-FWM-C, respectively.

To predict the signal and idler wavelengths as functions of the pump wavelength and ZDW, the phase matching curves for the LP_{02} mode of real PCFs were also calculated, Fig.7-3. It can be seen that the phase matching diagrams are similar for these three fibres (for the reason that they have similar dispersion curves). For pump wavelengths in the anomalous dispersion region, closely spaced modulation instability sidebands are very clear and pump power plays an important role. When pumped at normal dispersion regime, two photons at pump wavelength can be converted to widely separated signal and idler photons in the UV (below 400 nm) and near IR range, respectively. It should be noted that in this region there is nearly no difference for peak pump power of 500 W and 2000 W, which were used for computations. These values correspond to 2.1 mW and 8.4 mW (2.23 and 8.94 mW if a Gaussian pulse is assumed) of average power for the laser pulse used. The power levels used in the experiment fall into this range.

These calculations were tested using a frequency-doubled Nd:YAG microchip laser as the pump source, Fig.7-4. The same laser source was used for the supercontiuum generation in LP_{02} mode in Chapter 6. The pump light was coupled into each fibre device via neutral-density filters, a polariser and a half-wave plate to control input power and polarisation. Each fibre device contained a mode-filter to ensure a pure fundamental LP_{01} mode, followed by a low-loss, all-fibre, broadband LP_{02} mode convertor formed within the fibre [133]. The detailed mode filtering and mode conversion process were discussed in Chapter 5. To avoid any nonlinear effects in the LP_{01} mode before conversion to the LP_{02} mode, the distance of LP_{01} mode propagation was kept shorter than 20 cm. Mode patterns at

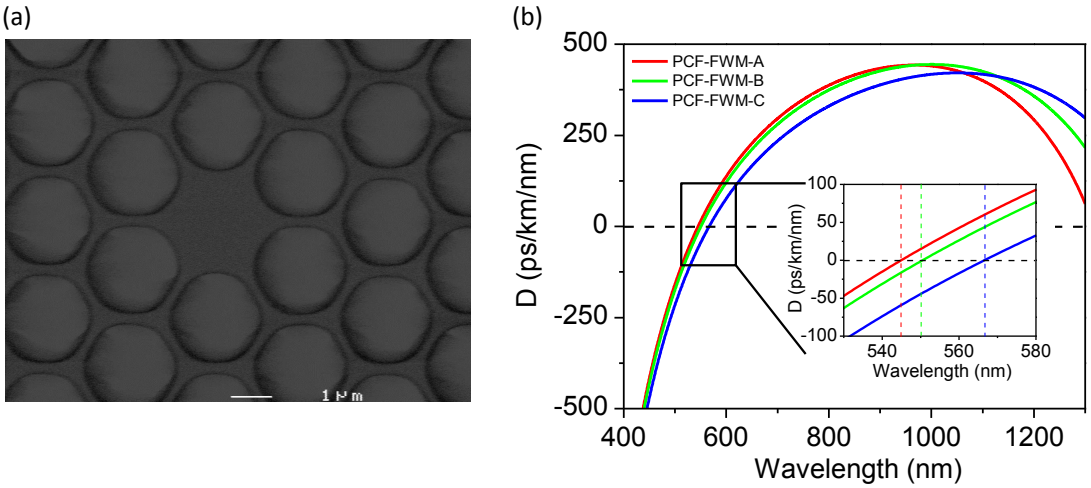

Fig. 7-2: (a) An SEM image of Fibre PCF-FWM-B, one of the three fibres used for the FWM experiment. (b) Calculated dispersion curves for all three fibres. Inset is a magnification of a small region near ZDWs.

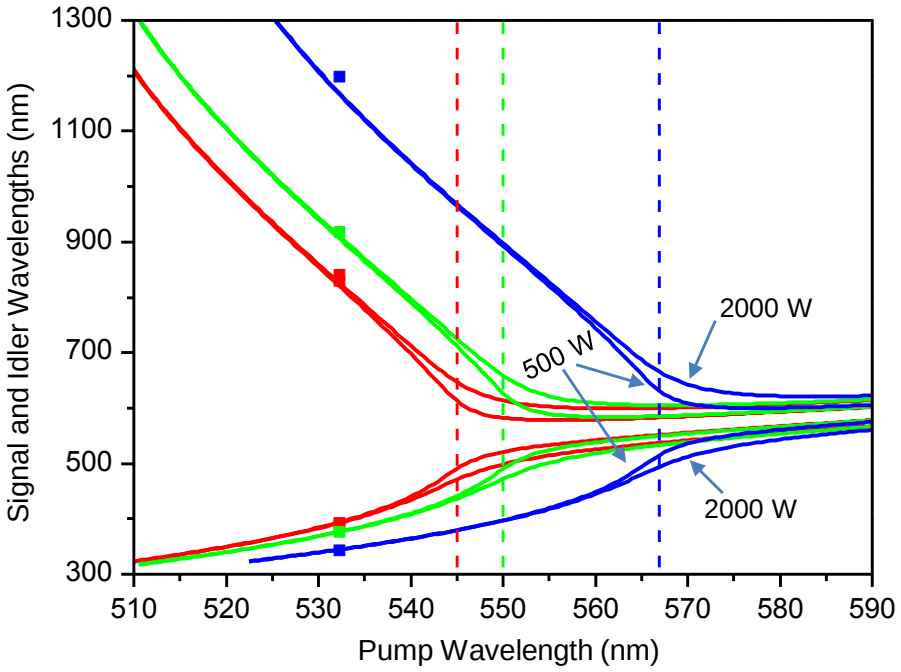

Fig. 7-3: Phasematching curves for fibres PCF-FWM-A(red), PCF-FWM-B(green) and PCF-FWM-C(blue). Solid lines are calculations for peak pump powers of 500 W and 2000 W. Points are experimental results for a 532 nm pump laser. Dashed lines are the ZDWs.

the pump and FWM wavelengths were examined at the output end of the fibre using a grating and/or bandpass filters. Output spectra were recorded with an optical spectrum analyser (OSA), but for wavelengths shorter than the 350 nm limit of the OSA a UV spectrometer (Ocean optics USB4000) was used.

7.3 Results

Fig.7-5 shows output spectra for 2 m of LP_{02} mode propagation in fibre PCF-FWM-A. The $\sim$ 140 ps calculated walk-off between pump and idler pulses for this length of fibre is much less than the pump pulse duration (pump-signal and signal-idler walk-off are smaller). The calculated signal and idler wavelengths were 393 and 824 nm respectively and the observed signal wavelength was 390 nm. This demonstrates that the plane-wave calculation based on the SEM image was quite accurate, which is fortunate because the dispersion of higher-order modes is difficult to measure directly [23, 133].

For low output power we see FWM peaks rise just above the background noise at locations well-separated from the pump wavelength. There are two stimulated Raman scattering (SRS) Stokes peaks at 545 and 558 nm and an anti-Stokes peak at 520 nm at about 15 dB less intensity than the 545 nm Stokes. Amplification of the anti-Stokes peak is due to weak coupling between SRS and FWM, as has been observed in the fundamental mode [54].

At an output power of 1.6 mW the signal remains narrowband nature while the pump Raman peaks near pump wavelength form a continuum, Fig.7-5 and Fig.7-6(a). Cascaded Raman peaks appeared in the signal after just a slight increase of output power to 1.7 mW, indicating sufficient power to generate new wavelengths. The idler is in the anomalous dispersion regime of the fibre, and its long-wavelength broadening is attributed to pulse breakup and the formation of Raman-shifting solitons. We observed weak sidebands at other wavelengths, such as the small peaks at 482 and 595 nm in Fig.7-5. These are consistent with an energy-conserving FWM process pumped at 532 nm but the corresponding phase-matching condition is not yet understood.

The near-field mode patterns at the pump and FWM wavelengths were checked regularly during the experiments and showed a good LP_{02} mode throughout. This included discrete images at wavelengths for which we have 10-nm bandpass filters, Fig. 7-5, and dispersed images produced by a diffraction grating providing information across all wavelengths. To test for fibre uniformity we repeated the

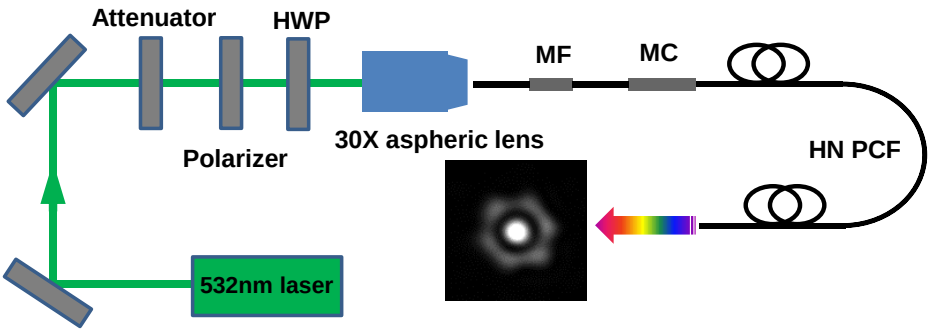

Fig. 7-4: Experimental setup. HWP = half-wave plate, MF = mode filter, MC = mode convertor. Inset: typical near-field mode pattern at 532 nm.

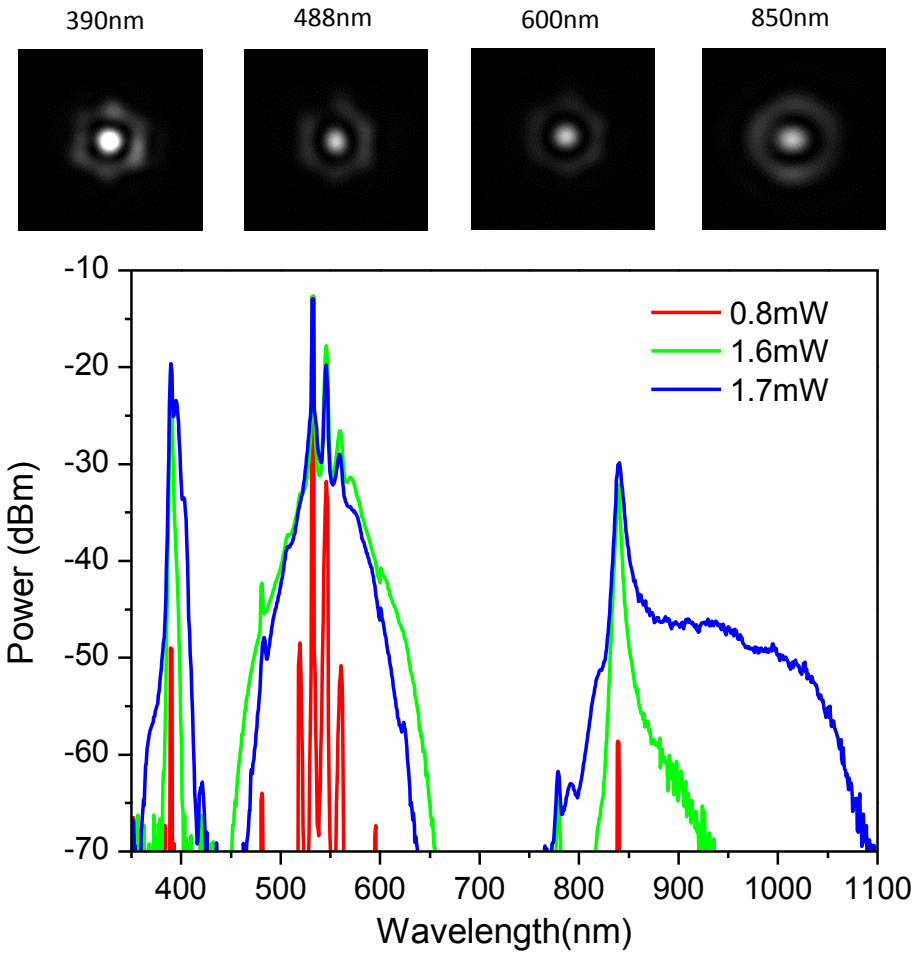

Fig. 7-5: Output spectra at different output powers in 2 m of fibre PCF-FWM-A. Resolution is 2 nm. Top row: output near-field patterns at selected wavelengths.

experiment for a different device also made from fibre PCF-FWM-A and observed small differences in the FWM wavelengths, Table 7.1. These correspond to a variation in fibre dimensions of around 0.2%, which is consistent with the uniformity of the fibre drawing process and potentially provides a way to measure core diameter variations to an accuracy of a few nanometres.

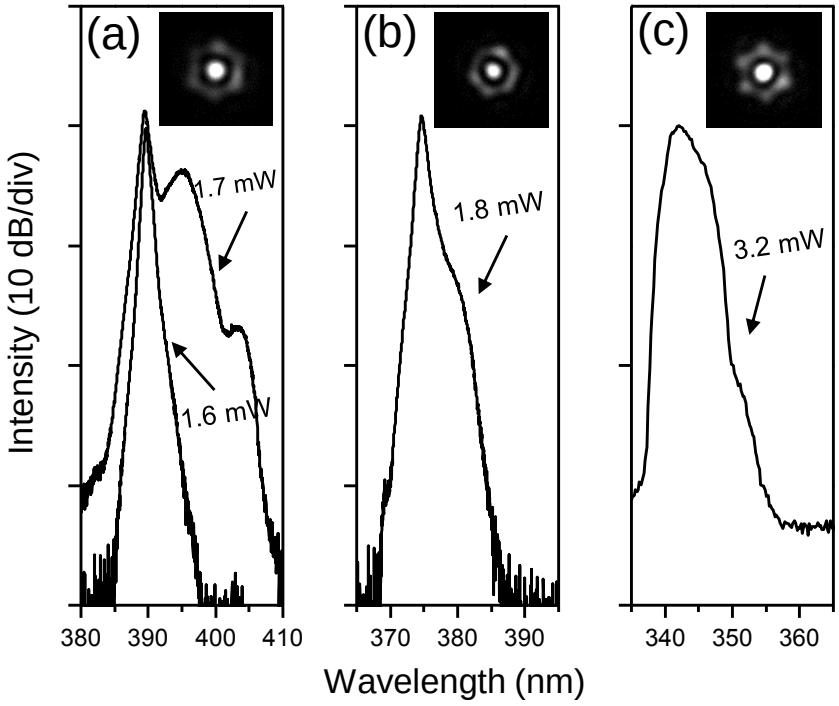

Fig. 7-6: (a,b,c) Signal spectra for fibres PCF-FWM-A, PCF-FWM-B and PCF-FWM-C respectively at specific output powers. (a) and (b) were recorded by an OSA, while (c) was obtained by a UV spectrometer. Insets: output near-field images at the signal wavelengths.

We repeated the experiment using fibre PCF-FWM-B, which had a slightly longer ZDW. The signal and idler were more widely separated than in fibre PCF-FWM-A, as expected from the phase-matching curve in Fig.7-3. The signal spectrum, with a peak at 375 nm, is shown in Fig.7-6(b). For 1.7 m of LP_{02} mode propagation in fibre PCF-FWM-C, which had an even longer ZDW, the signal wavelength was shorter still at 342 nm, Fig.7-6(c). In this case the calculated walk-off per metre between pump and idler pulses was more than 2 times that of fibre PCF-FWM-A. The wavelength conversion efficiency was therefore reduced and we did not observe any Raman Stokes line in the signal, even for a total output power of 3.2 mW.

Table 7.1: Theoretical (Th.) and experimental (Exp.) fibre parameters and FWM peaks

Fibre	ZDW (nm)	Signal (nm)		Idler (nm)	
		Th.	Exp.	Th.	Exp.
PCF-FWM-A (device 1)	545	393	390	824	839
PCF-FWM-A (device 2)	545	393	392	824	829
PCF-FWM-B	550	376	375	910	918
PCF-FWM-C	567	344	342	1171	1198

UV power measurements were challenging for the low powers in our experiments and also limited by the equipment available to us. We measured the total output power for fibre PCF-FWM-B with and without a UV bandpass filter. The measured powers were 90 μW and 1.6 mW respectively, corresponding to a conversion efficiency of about 6%. Unfortunately the filter's long wavelength transmission edge coincided with the peak signal wavelength of 375 nm so this measurement is an underestimate - the real value should be rather higher. However, the easily-observed cascaded Raman peaks in the signal peaks of fibres PCF-FWM-A and PCF-FWM-B indicate high conversion efficiency to short wavelengths.

7.4 Conclusions

In conclusion, we have experimentally demonstrated parametric four wave mixing in the LP_{02} mode via low-loss mode convertors pumped by a pulsed 532 nm laser. This provides an efficient way to generate well-defined UV wavelengths using an inexpensive source. As discussed before, all the generated wavelengths can be converted back to the fundamental mode if a reversed mode convertor is made at the output of the device. Applications for light of such wavelengths include fluorescence microscopy.

It must be stressed that although all experiments were done in the LP_{02} mode, there is no limit to extend this scheme to other higher-order modes. If designed appropriately, the hole control technique can be used to make other mode convertors, which can generate other useful higher-order modes, either converted from the fundamental mode or an intermediate mode. The combination of different fibres, different pump wavelengths and different modes can provide a very large tunability over the signal wavelength generation by FWM.

Chapter 8

Bessel-like beams generated by photonic crystal fibres

In this chapter, we describe how hole control techniques can be used to make all-fibre devices which generate a Bessel-like beam or its Fourier transform, an annular beam. Three methods are investigated experimentally to convert the fundamental mode to these higher order modes with low loss. The basic concepts of Bessel beams are introduced first, followed by detailed experimental methods and results.

8.1 Introduction

Diffraction is due to the wave nature of light. A tight focused beam will spread out as it propagates in free space. A Gaussian beam, expands its area of cross-section by a factor of two over a distance of Z_{R}. The beam radius increases to $\sqrt{2}\omega_{\mathrm{bw}}$, where ω_{bw} is the beam waist [134]. This characteristic parameter Z_{R} is the Rayleigh length:

$$Z_{\mathrm{R}} = \frac{\pi\omega_{\mathrm{bw}}^2}{\lambda}, \tag{8.1}$$

Although a laser beam, is highly coherent and has a low divergence over a very long distance, the Rayleigh length of a tightly confined beam, focused by a high power objective, is just a few microns [135]. Diffraction then sets a limit for a lot of applications.

However there exist, at least in theory, several types of beams that can be immune to diffraction. The Bessel beam is one such beam and was first studied

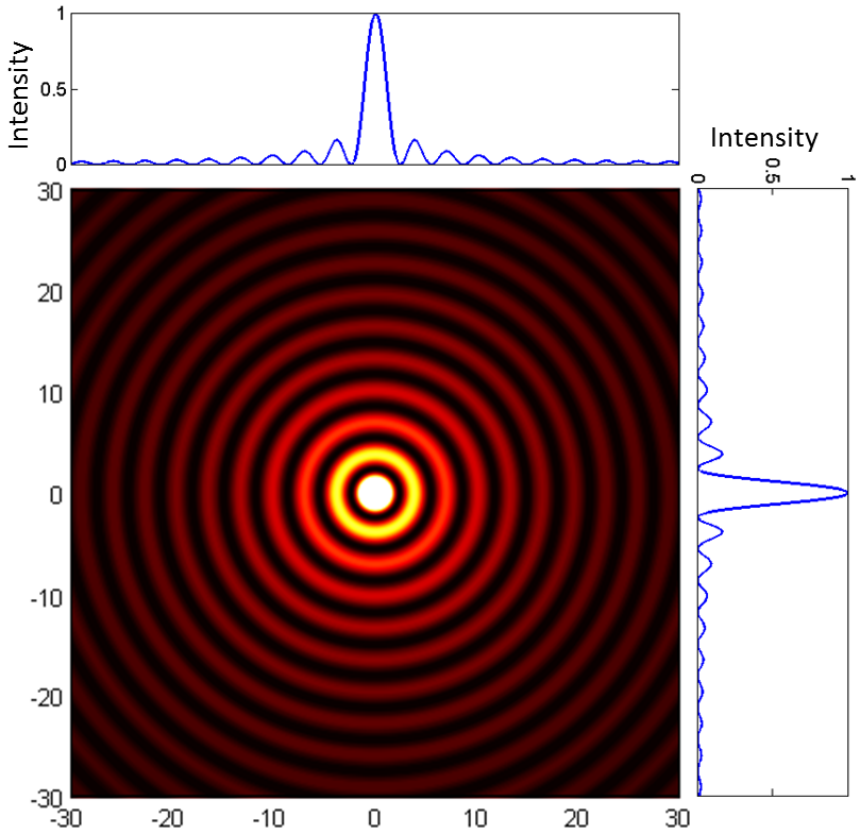

Fig. 8-1: Intensity distribution of a zero order Bessel beam.

theoretically [136] and experimentally [137] by Durnin et al. in 1987. Mathematically, the electric field, $E(r, \phi, z)$, of an ideal Bessel beam is described by the Bessel functions of the first kind, $\mathrm{J_n}(\kappa_\mathrm{r} r)$, in the form of [138]

$$E(r, \phi, z) = \exp(i\beta z)\mathrm{J_n}(\kappa_\mathrm{r} r)\exp(\pm in\phi), \tag{8.2}$$

where $\kappa_\mathrm{r} = \sqrt{k^2 - \beta^2} = \sqrt{(2\pi/\lambda)^2 - \beta^2}$ is the radial wavevector, while β is propagation constant. r, ϕ and z are the radial, azimuthal, and longitudinal components respectively. The intensity of a Bessel beam during propagation can be written as

$$I(r, \phi, z) = |E(r, \phi, z)|^2 = \mathrm{J_n}(\kappa_\mathrm{r} r)^2 = I(r, \phi, 0). \tag{8.3}$$

Eq. (8.3) demonstrates that an ideal Bessel beam is diffraction free in free space and its intensity is determined by the Bessel functions. This is how the Bessel beam gets its name. Eqs. (8.2) and (8.3) are the generalised representations of Bessel beams, while the most important one is the zeroth order Bessel beam,

which is described by the zero order Bessel function, J_0. This is also the case we study here. In the remainder of this chapter, the term of Bessel beam specifically means this zeroth order one if not stated otherwise.

The intensity distribution of this type of Bessel beam is shown in Fig. 8-1. We can decompose it as a set of plane waves propagating along a conical surface, Fig. 8-2 (a). All of these plane waves have identical wavevector components along the Z axis. During propagation, the phase shift gained by each plane wave along this axis is the same and the mutual phase relationship between them does not change. So the interference pattern of these plane waves keeps the same shape and amplitude along all the planes perpendicular to the propagation direction [138, 139].

The angular spectrum representation of an ideal Bessel beam is a ring shape with infinitely thin width in the K-space, which is shown in Fig. 8-2 (b) [138]. Thus the optical Fourier transform of a ring is a Bessel beam, and vice versa. More importantly, if we consider the Bessel beam or Bessel mode as the near field of a fibre mode, its far field mode pattern will be a ring, and vice versa, which is shown in Fig8-2 (c). These properties will be verified by our experimental results. However, it should be noted that an ideal Bessel beam requires an infinite distance to reach its far field.

Another important property of a Bessel beam is self-healing: using information contained in the rest of the beam to reform the central peak after passing an obstacle [140]. This can be easily understood since the Bessel beam can be considered as a set of plane waves propagating along the surface of a cone.

The energy distributed in each ring (between two zeros of the Bessel function) of a Bessel beam is approximately the same. An ideal Bessel beam has an infinite number of rings and carries infinite energy, so it cannot be generated in reality. However, a truncated Bessel-like (or quasi-Bessel) beam does not need all the rings to approximately maintain its intriguing properties, like diffraction-free propagation and self-healing. Good approximations have been achieved since Bessel beams were first proposed. From then, Bessel beams have been intensively studied and found numerous applications in different areas: particle guiding and manipulation [140, 141], optical accelerators [142], imaging and microscopy [143], materials processing [144, 145], and nonlinear optics [146].

There are many methods to generate a Bessel beam. Recall that the optical Fourier transform of a ring is a Bessel beam. This fact was used by Durnin et al. to first experimentally realise such a beam [137]. An annular aperture

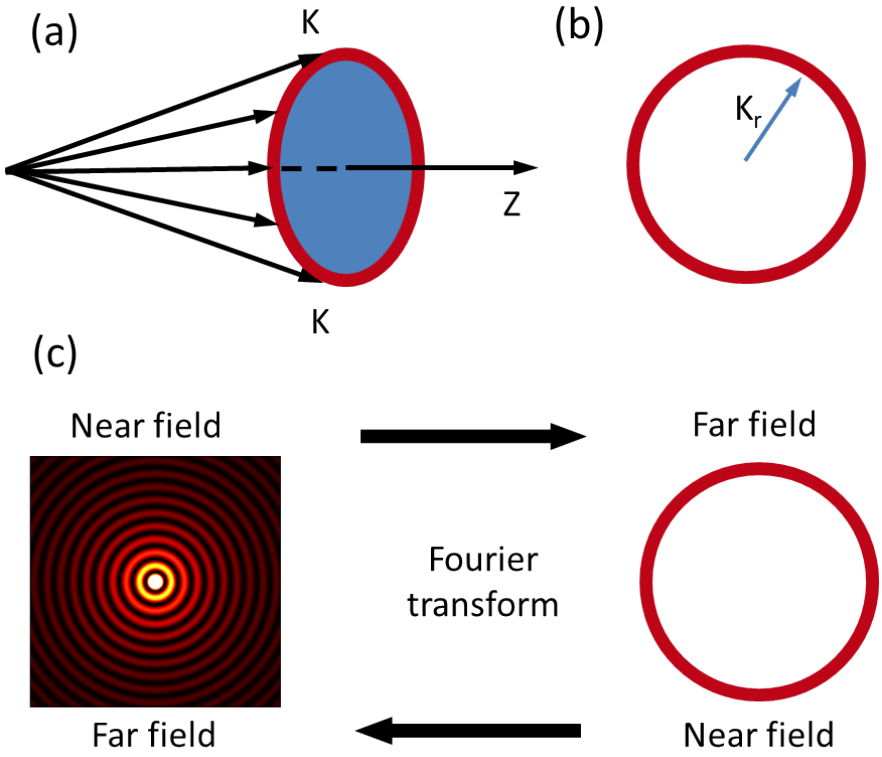

Fig. 8-2: (a) The k vectors of a Bessel beam propagating on the surface of a cone. (b) The angular spectrum representation of a Bessel beam. (c) The relationships between a Bessel beam and a ring beam can be considered as the near field and far field of a fibre mode.

was put at the back focal plane of a converging lens, which is shown in Fig. 8-4. This is a straightforward but not efficient way, as most incident light was blocked by the annular slits. An axicon, an optical component having a conic surface, was utilised to solve this problem [147, 148]. This method is cost effective and probably the best known technique for generating a Bessel beam. However, alignment is essential for this configuration and astigmatism can be caused by a small displacement [138]. Other ways, including spatial light modulator and holographic techniques, were used to change the phase and/or intensity of an incoming laser beam to form a Bessel beam.

All the aforementioned methods are implemented in free space, and bulk optics and careful alignment are needed. However, generating Bessel beams in optical fibres avoids the alignment and stability issues of bulk optical methods. One approach involves forming a tiny axicon at the end of a fibre [149, 150], which is difficult to implement experimentally. Multimode excitation in a multimode or

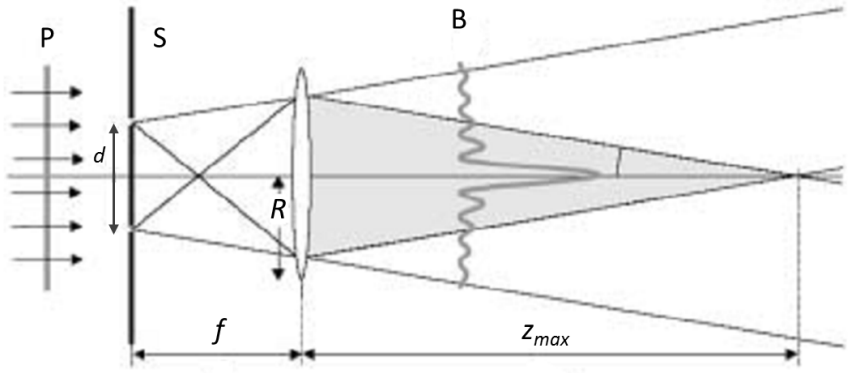

Fig. 8-3: The experimental setup for realisation of a Bessel beam used by Durnin et al. Image from [137].

core-less fibre produces a beam which is quite far from Bessel-like [151, 152].The most convincing method used a long-period grating to excite just one high-order cladding mode, which is inherently Bessel-like [153], but the grating functions only over a very narrow wavelength range. Moreover, until now no methods were proposed to generate a non-diffractive beam in PCFs.

In this chapter, we present three different ways for generating a Bessel-like beam and/or annular beam from PCFs. All of these methods are based on hole control techniques, which modify the cladding structure of a photonic crystal fibre.

8.2 Device 1

Theory

An ideal Bessel beam cannot be made in reality. Reasonable approximations however, like truncated Bessel beams, can be generated experimentally. Recalling the fibre modes shown in Fig. 1-6 of Chapter 1, higher order LP_{0n} modes (n relatively big, such as $n \geq 5$) resemble the shape of a Bessel beam quite well. The higher the mode excited, the better the approximation it can achieve. The diffraction-resistant and self-healing properties of a Bessel beam can be demonstrated by this higher order mode. In experiments, Ramachandran et al. obtained a good Bessel-like beam by exciting an $LP_{0,12}$ mode [82]. It is natural to think whether we can get similar or even better results using PCF mode convertors. The mode conversion method has a major advantage– it is broadband, in contrast to the fibre grating based method, which only works near the resonance frequency of

the grating.

In Chapter 5, we demonstrated how the fundamental mode (LP_{01}) can be converted to the LP_{02} mode. The fundamental mode of the central core has the biggest propagation constant in the region before the mode convertor. When the annular core is formed abruptly by hole collapse, a totally new waveguide appears in that local region. This waveguide contains two core regions: the central core and the annular core. Depending on the relative size of these two cores, the mode with the biggest propagation constant can be either in the central core region or in the annular core region. In the former case, the fundamental mode of the central core remains as the fundamental mode of the whole waveguide and, nothing much happens. However, in the latter case, a mode conversion occurs. This is exactly the case we studied earlier in this thesis. Moreover, depending on how big the annular core is compared to the central core, the converted mode varies. As we know from Chapter 5, an LP_{02} mode can be generated easily by collapsing the second and third rings of holes. It should be possible to convert the fundamental mode to higher order modes, like LP_{03} by collapsing more rings of holes or using a new PCF with smaller d/Λ. However, for even higher order modes, which require a very big annular core to favour such a conversion, the cladding structure of a solid core PCFs may not big enough, so this configuration reaches its limit. At the same time, another problem may arise, which relates to the adiabatic condition of the device. Although the fundamental mode is converted to a higher order mode when the annular core formed abruptly, its physical appearance remains the same. It requires a certain length to get the converted higher order mode to evolve its shape to the more familiar one. This can be done by joining those two cores (central and annular cores) together to get an expanded core. The length should be long enough to make sure the process is adiabatic. If the fundamental mode has been converted to a very high order mode directly, it may require a very long transition. This is may not be achievable, as the longest post-processing length of our taper rig is less than 20 cm.

However, these two problems can be potentially solved by the design shown in Fig. 8-4. The first part of this device, region I, has the same structure as the one used for the LP_{01} to LP_{02} mode convertor. However, the rest of the structure, II and III, is different. Instead of reopening of collapsed holes to squeeze the light to its original central core, we keep the enlarged core and further collapse (adiabatically) all the holes in the outer cladding to form a solid rod. This new waveguide confines and guides light by the refractive index difference

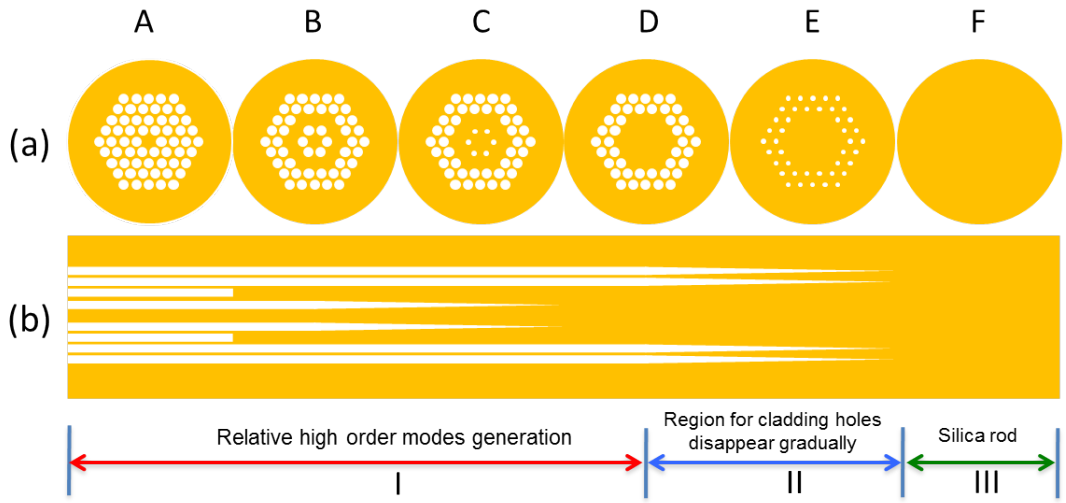

Fig. 8-4: Schematic diagram for making a Bessel-like beam using mode conversion. (a) is the cross-section at specific positions and (b) is the longitudinal structure evolution along the device. The silica area is shown in gold, while holes are shown in white.

between silica and air. It is known from the LP_{01} to LP_{02} mode convertor that the fundamental mode has been converted to the LP_{02} mode when the annular core appears abruptly. However, only the label "LP_{02}" moves to the light in the central core; the mode distribution is unaffected in that point. If the holes between the central core and annular core are big enough to isolate these two waveguides, this labelled "LP_{02}" mode behaves exactly as the fundamental mode of the original fibre. This means the light which stays in the central core can be either the LP_{01} mode or the LP_{02} mode depending on which waveguide it refers to.

The situation is similar in Fig. 8-4. When the light is coupled to the PCF at position A, the light apparently propagates along the central core in the fundamental mode. However, this ignores the waveguide in the outer cladding (beyond the holey region and consisting of pure silica). This is normally correct because the holey region isolates these two waveguides along the whole length of a PCF. However, if we treat them together as a whole waveguide, the situation changes. Although the light stays in the central core and keeps the fundamental mode appearance, the mode order changes. As the silica area in the outer cladding is very large compared to the central core, the light in the central core can be in a very high order mode of the entire structure. If the holey region can disappear adiabatically, the "higher order" mode can reach its normal appearance, which

resembles the Bessel beam. This evolution in principle can be realised directly by collapsing the holey region. However, as mentioned above, this direct evolution requires a very long transition. Instead in Fig. 8-4, this evolution is fulfilled via an intermediate process: conversion of the LP_{01} to the LP_{02} mode. The light in the central core sees an intermediate waveguide (B-D) before it reach its final appearance (D-F).

Experiment and results

This device was realised by heating a fibre with a small flame (on the taper rig) and applying pressure to the holes being kept open but not to holes being collapsed. Hole size transitions were formed by varying the motion of the flame, which is described in Chapters 2 and 5. The final structure along the whole device is illustrated in Fig. 8-4(b). Furthermore, in order to provide a pure fundamental mode (for the central core) in the input, a short length of fibre was heated without any pressurisation to form a mode filter locally, which is similar to that shown in Chapter 5.

The experimental results are shown in Fig. 8-5. The near and far field patterns at specific positions along the device show changes of light distribution. The cross-sections at these points are also provided. The fundamental mode was converted and evolved to the normal appearance of a LP_{02} mode, at position D of Fig. 8-4. After collapsing the cladding holes, the importance of the silica area in the outer cladding becomes obvious. The original light distribution actually lies in a very high order mode and evolves to its normal shape by this collapse, at position F of Fig. 8-4. Its near field has kind of multi-ring shape, while the far field pattern looks like a ring, both of which resemble those of an ideal Bessel beam. However, the quality of this beam is not good. We conjecture that there are two main reasons that may contribute to this imperfection. The first relates the structure of the PCF used. As can be seen from the cross-section at position D, neither in the radial nor the azimuthal direction are the sizes of the holes the same. The other possible reason is that the transition is not long enough to be adiabatic. Both of these reasons cause mode coupling, which results in light staying in multiple modes instead of a pure mode. Although by designing a PCF with better structure and increasing the transition length one can potentially improve the quality of this beam, it is very difficult to totally avoid coupling to other modes and get a pure higher order mode.

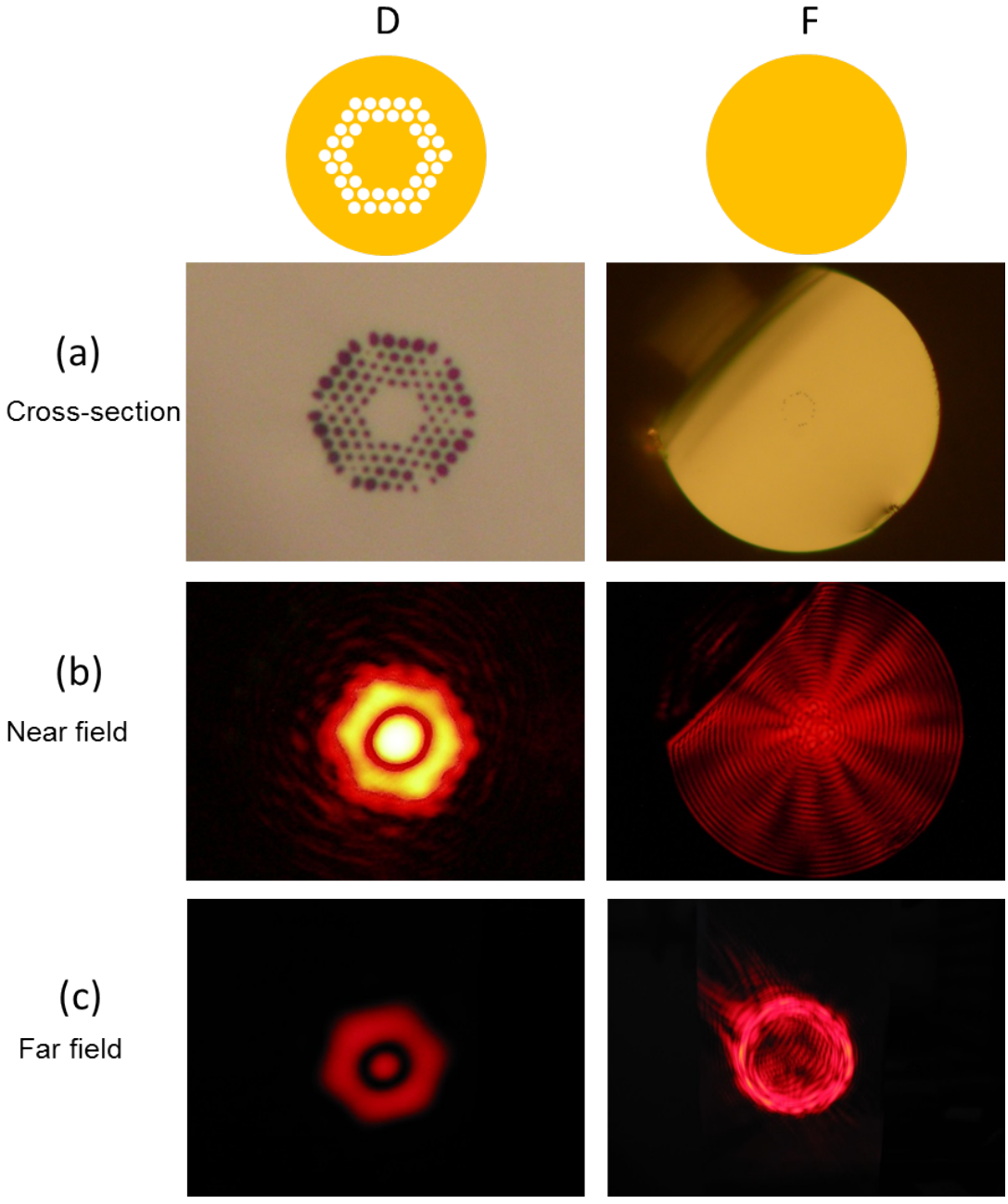

Fig. 8-5: The experimental (a) cross section, (b) near field patterns and (c) far field patterns at specific positions along the device. The light is at a wavelength of 635 nm.

8.3 Device 2

In this section, a new method of hole control is discussed. Previously, collapse or expansion of holes were done either by using the fibre tower during drawing or the taper rig after the fibre has been made. Viscosity, surface tension and applied pressure all together determine which effect dominating in the process. However, there is another way, using a fusion splicer, which also can change the structure of a PCF, although in most cases this has been used to collapse holes. Here, a Bessel-like beam generator is made by sequentially collapsing different rings of holes of a PCF. The phenomenon described in this section was first observed by Jim Stone. Because of the similarity between this and my other Bessel-like beam generators, I joined this project and obtained all the experimental results presented in this section.

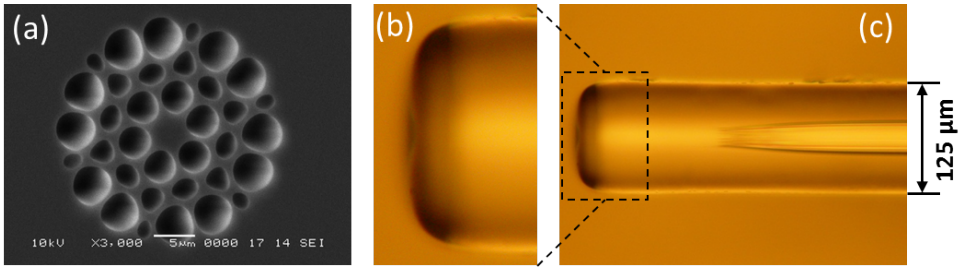

Fig. 8-6: (a) SEM image of the unprocessed PCF; the scale bar is 5 μm.(b) Magnified endface from (c) a side view of the structure formed at the end of the fibre using the splicer.

The PCF, shown in Fig. 8-6 (a), has three rings of air holes with different sizes and can be used for supercontinuum generation. The Bessel beam generator device was made by placing the fibre in a commercial fusion splicer (Fujikura FSM-40PM) with the cleaved end level with the electrodes, and activating the arc for 500 ms at a power of 14.1 mA to obtain the structure of Fig. 8-6 (b-c). This has a $\sim$170 μm long transition over which the holes in the fibre steadily shrink until they completely disappear, followed by a similar length to the end of the fibre without holes. The sequence of hole collapse in the three rings structure was determined by the relative size. The endface of the fibre was also rounded off by the arc, Fig. 8-6(b), with a small concave "dimple" in the middle where the holes in the fibre shrank longitudinally as well as transversely, drawing material inwards [154]. The result was a fairly-complicated annular lens. However, we found it very easy to repeatedly make structures that were identical, at least as far as the production of Bessel-like beams was concerned.

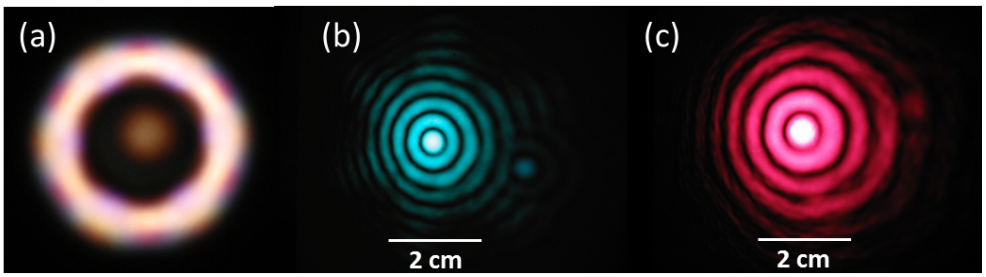

Fig. 8-7: (a) Far field pattern from the end of the fibre for white supercontinuum light. (b,c) Bessel-like beams imaged by a 60X microscope objective via bandpass (BP) filters at (b) 500 nm and (c) 700 nm.

To characterise the device, we injected light from a 1064 nm pulsed laser into about 3 m of the fibre to generate SC light. This was simply a convenient way to couple broadband light into the fundamental mode of the fibre (which could readily be confirmed by cleaving the device off the end of the fibre afterwards). The far field pattern emerging from the processed end of the fibre was a thin ring resembling the Fourier transform of a Bessel beam, Fig. 8-7(a). The whiteness of the ring indicates that the same far-field pattern was generated over a wide wavelength range. The Bessel-like patterns shown in Fig. 8-7 (b) and (c) were imaged by transforming this beam using a 60X microscope objective (NA = 0.85) focused to a point inside the fibre (around the position where holes disappeared completely and the pure silica region started), as if observing a virtual near-field pattern through the lensed fibre end. The two images were projected into a screen via 500 nm and 700 nm bandpass filters respectively, confirming that formation of the Bessel-like beam was spectrally broadband.

To investigate the self-healing property of the generated Bessel-like beam, the central peak of the beam was blocked by a triangular obstacle about 250 μm across attached to a glass cover slip following a 589 nm bandpass filter. The light pattern beyond the obstruction was projected onto a screen using a 10X objective and recorded with a camera, Fig. 8-8(a). The 10X objective, screen and camera could be repositioned in Z as a unit, so that the scales of the images were the same. The central lobe of the beam was blocked by the obstacle but after $\sim$7.5 cm the first two rings have been largely reconstructed, Fig. 8-8(b). For comparison, Fig. 8-8(c) shows the beam without the obstacle, confirming the self-healing property of the generated beam.

Replacing the objective with a doublet lens (Comar 40OD14, focal length 40 mm, NA = 0.18) yielded a spectacular pattern with many more rings, which

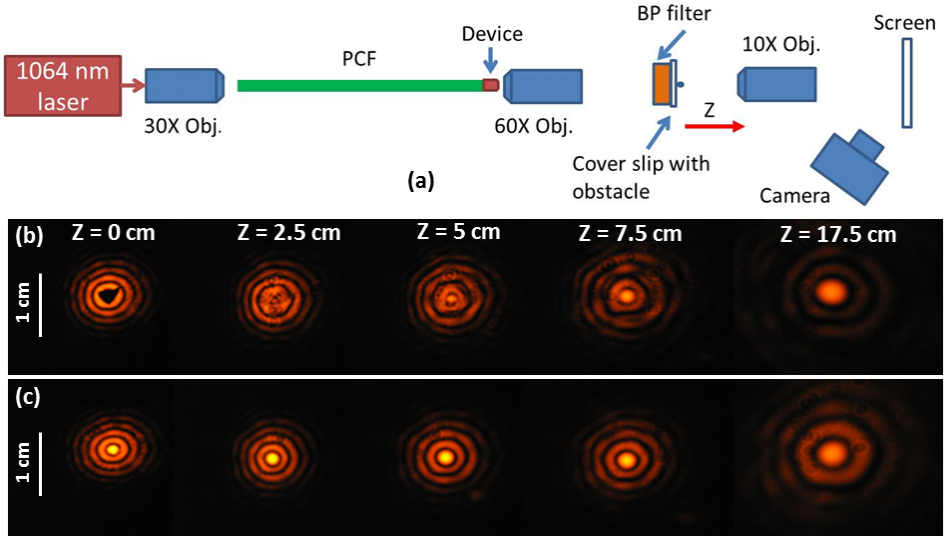

Fig. 8-8: (a) Self-healing experimental setup. (b) Images of the 589 nm beam formed by a 10X objective with its focus at different distances Z behind an obstacle. (c) as (b) but without the obstacle.

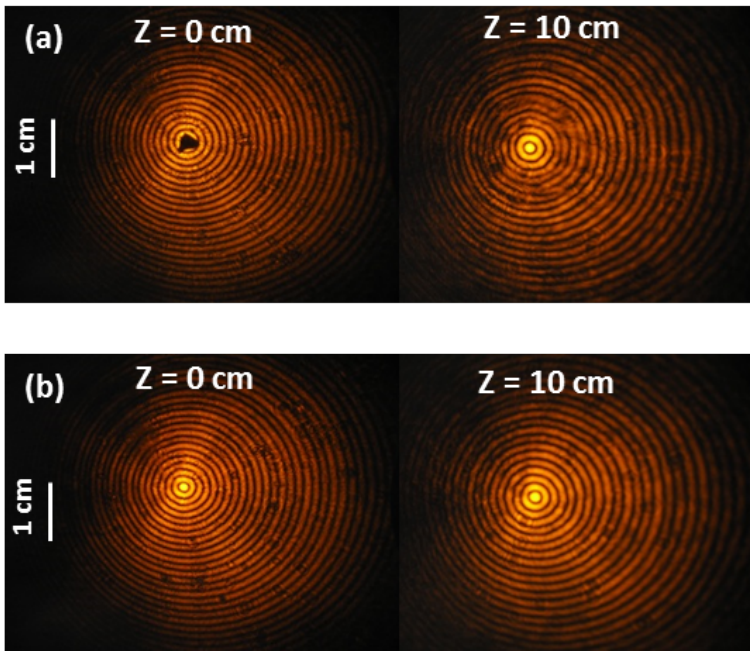

Fig. 8-9: Self-healing experiment. The same as Fig. 8-8, but for a beam formed using a doublet lens instead of the 60X objective.

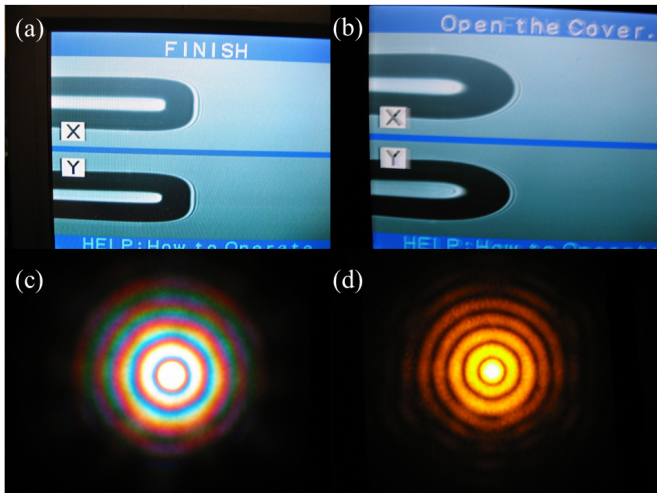

Fig. 8-10: Images displayed in the monitor of the fusion splicer after devices have been made with arc time of (a) 500 ms and (b) 950 ms. Far field patterns of the device illuminated by (c) white supercontinuum light and (d) light at 589 nm

looked like a more-complete Bessel beam. Fig. 8-9 shows self-healing of this beam following the same obstruction.

It is not completely clear yet how these Bessel-like beams are being formed, but our investigations indicate three key contributions. Firstly, the hole size transition in the PCF converts the fundamental mode into a different low-order mode, perhaps LP_{02} or LP_{03}, by a similar process to that discussed in Chapter 5. In the final solid-glass section of fibre, the mode should evolve into a far-field pattern dominated by a broad ring. Secondly, this far-field pattern is distorted by the annular lens at the fibre's endface to make the ring thinner and inhibiting the central peak – a thinner far-field ring corresponding to the Fourier transform of a Bessel function with more rings. Finally, it appears that Fresnel diffraction from an aperture stop within the doublet lens fortuitously contributes extra rings to the Bessel-like beam imaged by that lens.

When increasing the arc time from 500 ms to 950 ms but keeping other parameters unchanged, the endface of the device changed dramatically, which was even obvious in the monitor of the splicer, Fig. 8-10 (a-b). The radius of curvature of the lens became short and the small concave "dimple" in the middle of the lens disappeared. More interestingly, we observed a Bessel-like beam in the far field, Fig. 8-10 (c-d). The lensed end of this device served as an imaging lens, which brings out the Bessel-like beam from inside the fibre to the free space.

In conclusion, a PCF-based Bessel-like beam generator has been made by a commercially-available fusion splicer. Collapse of holes in the PCF yield a

waveguide transition, a solid-glass free-diffraction zone and an lens at the fibre's endface. These features together convert the fundamental mode of the fibre into the Fourier transform of a Bessel-like beam. The Bessel-like beam itself can be imaged using a lens focusing inside the device. Self-healing of these beam was demonstrated experimentally. When the curvature (focal length) of the lensed end of the device matches the position of the Bessel-like beam, this beam can be brought out into free space.

8.4 Device 3

In this section, a third method is used to generated a Bessel-like beam. In previous sections, we concentrated on generating a Bessel-like beam in the near field, and getting a ring shape pattern in the far field. Here, we generate a ring mode in the near field. As known from Section 8.1, its far field is a Bessel-like beam.

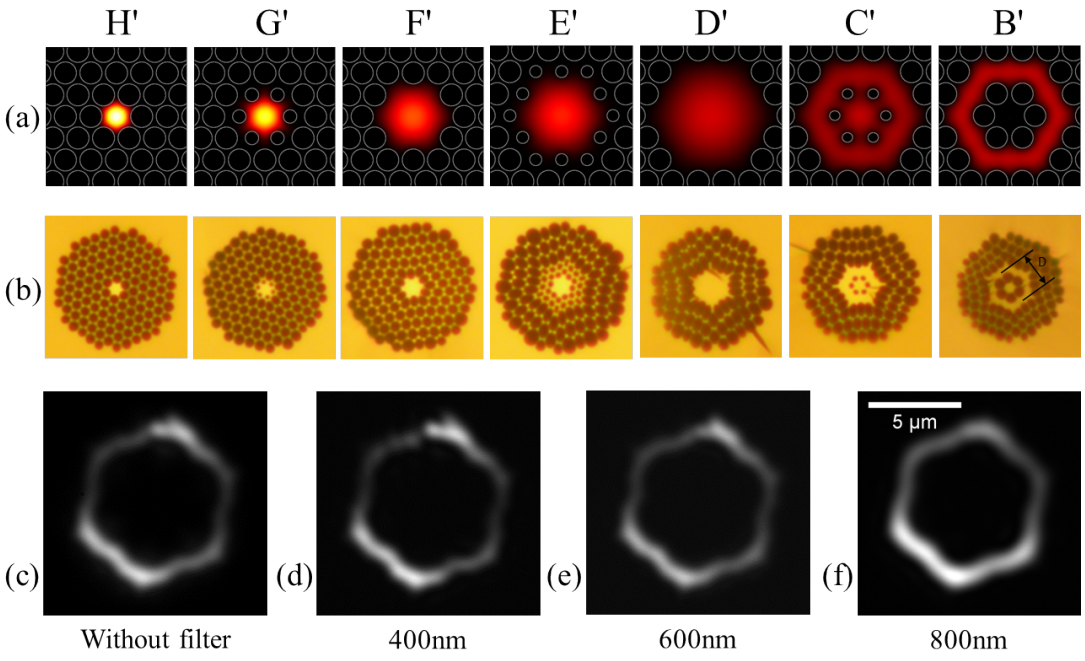

Fig. 8-11: Cross sections at location H′-B′ along which a ring mode has been generated. (a) Simulated fields for an LP_{01} mode input at H′. Grey circles are hole boundaries. (b) Optical micrographs of an experimental structure, to the same scale. The holey region at location H′ is around 23 μm across. The diameter of annular core, D, at location H′ is 7 μm, while the width is 1.3 μm. (c-f) Measured near-field patterns for (c) whole wavelengths and for light at selected wavelengths of (d) 400 nm, (e) 600 nm and (f) 800 nm, to the same scale

The way to generate a ring mode in a PCF is shown in Fig. 8-11. A BPM simulation is shown in Fig. 8-11 (a) and Typical cross sections along an experimentally generated device are shown in Fig. 8-11 (b). The diameter and width of the generated annular core is around 7 μm and 1.3 μm respectively, location B$'$ in Fig. 8-11 (b). This structure actually is the same as the one used to convert the generated LP_{02} mode back to LP_{01} mode in Chapter 6. In that chapter, we called it a reverse mode convertor, as the structure is the same as that of an LP_{01}- LP_{02} mode convertor but in a reverse sequence. In that case the input light, at location H$'$, is the generated LP_{02} mode. However, in the device discussed here we use an LP_{01} mode input light instead of a higher order mode. In order to achieve a pure LP_{01} mode input, a short length of fibre was heated to form a mode filter, which stripped out all higher order modes and cladding modes. From location H$'$ to D$'$, the device works as a beam expander, as the core is becoming larger and larger. When the first ring of holes appears again and the two core system is formed, the annular core is the destination for the mode with the greatest propagation constant β. This means that the fundamental mode at the location H$'$ will end as a ring mode at location B$'$. The near field patterns at this point, Fig. 8-11 (c-f), were recorded by a CCD camera (Basler, A631F) when illuminated by a white light source (bandpass filters were used in (d-f)). As expected, a ring mode shape has been generated (although they are a little bit hexagonal, resembling the hexagonal lattice of the PCF). As this device does not rely on any kind of resonance, it can work over a very broad frequency band, like the mode convertor discussed in previous chapters. It is obvious that there is no light staying in the central core, Fig. 8-11 (c-f), indicating a pure ring mode. By checking the light intensity in the central dark region where corresponding to the central core, we found that the detected light intensity there below the noise level of the CCD camera used.

Combing the knowledge from Chapter 5 and here, it is easy to know that this device can also be used as a mode splitter for the fundamental mode [155]. If the input light, location H$'$, contains both LP_{01} and LP_{02} modes, the trajectories of these two modes are different. The LP_{01} mode will end in the annular core at location B$'$, while the LP_{02} mode will be converted to the LP_{01} mode in the central core.

The far field of a ring mode is a Bessel-like beam. The evolution from the near field (ring mode) to the far field (Bessel like beam) is shown in Fig. 8-12 for the wavelength of 800 nm. Other wavelengths gave similar results. The images

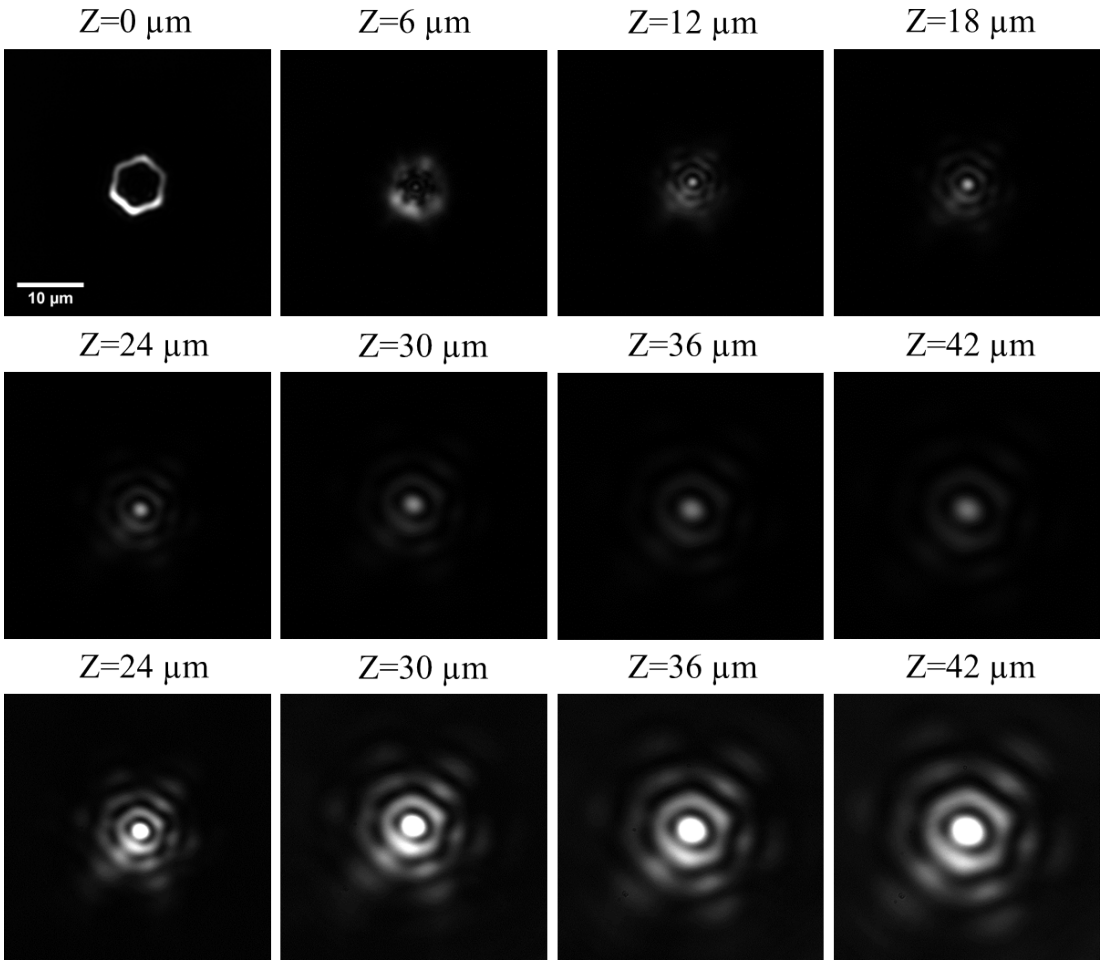

Fig. 8-12: The evolution of a ring mode from the near field to the far field for the wavelength of 800 nm. Z indicates different propagation distances. Z=0 μm means the near field plane. The bottom array is the same as the medium array, apart from enhanced brightness and contrast, which were adjusted to highlight faint outside rings. All images were plotted to the same scale.

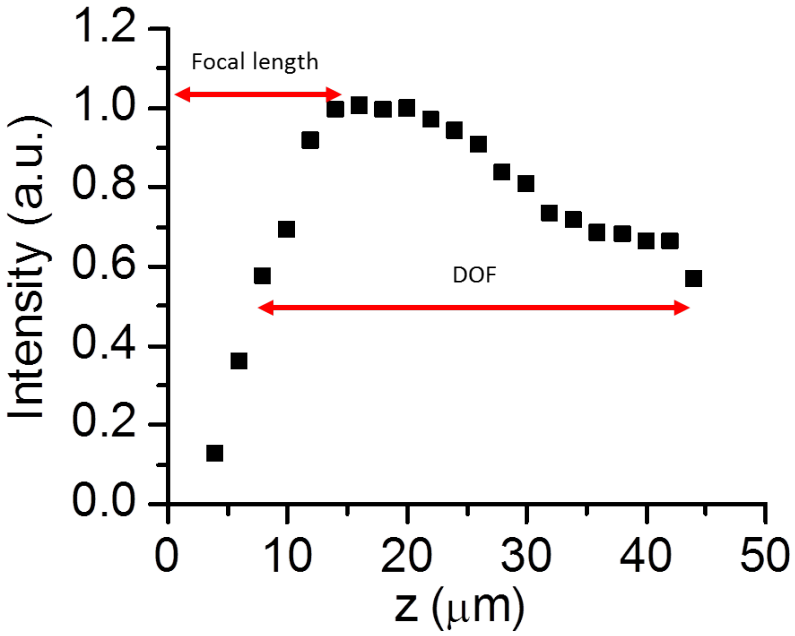

Fig. 8-13: The peak intensity evolution of the central lobe of the Bessel-like beam along the propagation direction (Z).

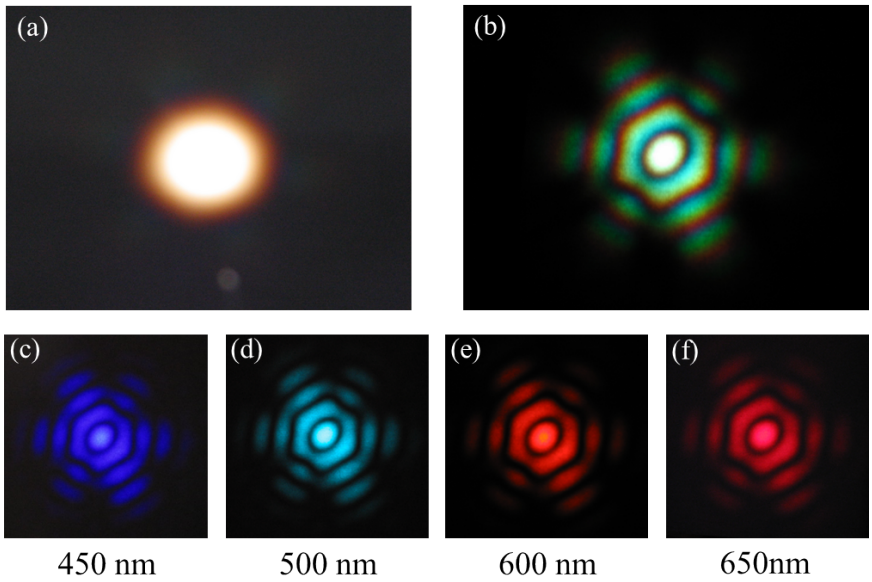

Fig. 8-14: Far field patterns. (a) Image was taken at location H$'$ when illuminated by a white light source, showing true LP_{01} mode input. (b-f) Images were taken at location B$'$ for (b) white light source, and for wavelengths of (c)450 nm, (d)500 nm, (e)600nm and (f) 650 nm, showing Bessel-like beam in the output.

were taken (Basler, A631F) at different propagation distances Z in free space by adjusting the focal plane of the objective (40X, NA = 0.65). The Bessel-like beam was found at a propagation distance of about 12 μm. In order to estimate the performance of this Bessel-like beam, we obtained the focal length and depth of focus (DOF) by analysing the images shown in Fig. 8-12. The focal length is defined as the propagation distance when the focal spot was achieved (maximum intensity of central lobe), while DOF can be considered as the interval between halves of this maximum intensity along the propagation axis. The results is shown in Fig. 8-13. The focal length is about 16 μm, at which the Bessel-like beam has a central lobe around 1.3 μm (FWHM). The DOF of this Bessel-like beam is more than 38 μm. In comparison, a Gaussian-shaped beam with the same spot size reaches its half intensity after just a few microns (as estimated by its Rayleigh length).

The far field patterns at other wavelengths were also checked and recorded using a commercial camera, Fig. 8-14. It is clear that the few rings characteristic of the Bessel-like beam occurs for all wavelengths. The insertion loss of this device was measured by the cut-back technique to be less than 0.3 dB for all measured wavelengths (450 nm, 530 nm, 800 nm), confirming low loss and broad bandwidth. The far field pattern after the mode filter was a pure fundamental mode, as shown in Fig. 8-14 (a). This confirmed that the input light, location H$'$, was indeed in the LP_{01} mode.

Performance can be improved by appropriate design. Reducing the width of the annular core can increase the number of rings formed in the Bessel-like beam, which approaches the ideal Bessel beam and would have a longer diffraction-resistant propagation distance [138]. It has also been demonstrated that increasing the diameter of the annular core gives a similar tendency of performance improvement [156, 157]. In our device, the Bessel-like beam was formed and propagated in free space. However, this beam still suffers from strong diffraction. If looking back to the setup used by Durnin et al.[137], we can find some differences in the experimental configuration. In their configuration, the ring shaped light is obtained by passing an annular slit at the back focal plane of a lens. The Bessel beam was formed after this lens. Following this, it would be a good idea to form an fibre lens with appropriate focal length at the end of our device. This lens can be formed either by self-assembly [156] or using a fusion splicer, as shown in last section.

8.5 Conclusions

As an ideal Bessel beam cannot be made in reality, a truncated Bessel-like beam allows us to investigate and utilise its intriguing properties, such as diffraction-free propagation and self-healing. In this chapter, we proposed three different ways to make a Bessel-like beam, manifested by its multiple concentric rings and specific characteristics. The Bessel-like beam and ring beam can be converted into each other via the Fourier transform, by the near field to far field evolution in cases studied in this chapter. Although we concentrated on how to make such a beam, there are many interesting applications which are worthy of further investigation. Moreover, the third device has other potential applications, such as a mode splitter.

Chapter 9

Conclusions

This thesis reported hole control in PCFs during the fibre fabrication process and after they have been made. Different types of all-fibre devices were made based on modifications over the holey region of PCFs for a series of linear and nonlinear applications.

Hole control during fibre drawing process

In Chapter 3, we revealed for the first time that a direct knowledge of the viscosity (or temperature) of the glass in the furnace is not necessary for describing the drawing process of fibres with holes. In our model, the effect of viscosity is represented by the fibre draw tension which, unlike viscosity, can readily be measured in practice by the fibre fabricator. This makes it possible to simulate the outcome of PCFs, at least those fibres whose holes are well separated, using only quantities that can actually be measured. We have designed and fabricated a special 3-hole fibre to test our model and found the experimental results agree with the model without recourse to any adjustable fitting parameters. These results give directions as to how hole size can be controlled by varying draw tension, pressure and drawdown ratio, which is important for special fibres, like PCFs.

Hole contol based on post-processing techniques

From Chapter 4, our investigations moved from fibre drawing to fibre post-processing, which means hole control is done after the fibre has been made. Thanks to the versatility and controllability of post-processing techniques, several novel devices were formed in situ within PCFs, ranging from Young's slits to mode converters.

In Chapter 4, we demonstrated a structure with two high aspect ratio (4:1) cores, which resembles Young's slits. The interference pattern has much improved performance over that based on normal circular cores. The well-defined interferogram is compatible with the 1-D detector array used for static, passive spectrometers. Enhanced intensity is critical to increase the sensitivity for weak signal detection. This special device can find applications in fibre optic spectrometers.

In Chapter 5, all fibre $LP_{01}-LP_{02}$ mode convertors were made in highly nonlinear PCFs to convert the fundamental mode to a higher order LP_{02} mode. Through careful characterisation we showed that this mode convertor has high mode purity (more than 20 dB), low loss (0.1 dB at some wavelengths), and broadband conversion (at least 400-1100 nm). The converted higher order mode can be converted back by simply forming a second, reversed MC at the end of the device. The study on mode convetors was continued in Chapter 8, where we focused on converting the fundamental mode to a Bessel-like beam or its Fourier transform version, an annular beam. Three different methods were investigated experimentally to achieve this non-diffractive, self-healing beam.

Nonlinear fibre optics in higher order modes

In Chapters 6 and 7, we extended nonlinear fibre optics to higher-order modes using our all-fibre mode convertors. We chose supercontinuum generation and FWM in the LP_{02} mode as two examples to demonstrate that higher-order modes in optical fibre are good candidates for many nonlinear applications, due to their distinct properties. Our analysis showed that zero-dispersion wavelengths as short as 310 nm are possible with the LP_{02} mode (compared to 460 nm for LP_{01} mode), giving a predicted short-wavelength supercontinuum edge down to 240 nm (compared to 305 nm for LP_{01} mode). Desirable properties can be achieved for much bigger cores. We demonstrated supercontinuum generation pumped by nanosecond pulses at 532 nm in fibres with $> 2\mu$m core diameter and generated wavelengths as short as 320 nm. In order to provide an output compatible with other optical systems, the whole spectrum was efficiently converted back to the fundamental mode. The generated light is important for applications requiring visible or ultraviolet continuum, such as fluorescence microscopy. Using the same laser source and similar mode convertors but pumped in the normal disperion region, we experimentally achieved UV four wave mixing in the LP_{02} mode. Ultraviolet signal wavelengths as short as 342 nm were generated. It should be

noted that all of these can of course be generalised to other modes besides LP_{02}. Our mode convertors provide a low-loss and broadband tool for realising this unexplored space of possibilities.

Appendix A

Modelling of fibre drawing

In this appendix we explain the model and derive the analytical solution in detail, following the procedures described in Section 3.2. The analysis of this model was done by Tim Birks.

A.1 Drawdown

As we discussed in Chapter 3, a solid preform of radius r_1 is fed into a furnace at the feed rate u_f and a fibre of radius r_2 is drawn out at the draw speed u_d, all in the direction of positive x, Fig. 3-1. The furnace gives the glass a viscosity distribution $\mu(x)$, defined for all x by having infinite values outside the furnace. We assume the drawing process has reached a steady state, with a constant draw tension, and that volume of glass is conserved. The invariance of glass flux through transverse planes at arbitrary x relates the longitudinal glass speed *u(x)* to the local radius *r(x)* at x

$$u(x) = \frac{dx}{dt} = \frac{r_1^2}{r^2(x)} u_\mathrm{f} \equiv \frac{u_\mathrm{f}}{\rho^2(x)}, \tag{A.1}$$

where the local drawdown ratio $\rho(x)$ is

$$\rho(x) = \frac{r(x)}{r_1} \leq 1. \tag{A.2}$$

As $x \to \infty$ this gives the final drawdown ratio ρ_0 in terms of the process speeds

$$\rho_0 = \rho(\infty) = \frac{r_2}{r_1} = \sqrt{\frac{u_\mathrm{f}}{u_\mathrm{d}}}. \tag{A.3}$$

The force F required to induce a velocity gradient du/dx along an extending

viscous thread is [158]

$$F = 3\pi r^2(x)\mu(x)\frac{du}{dx}. \tag{A.4}$$

Since we neglect inertia (all accelerations are small) and gravity (the weight of the glass is small compared to the draw tension), F is uniform along the glass body and equal to the draw tension in the fibre.

By considering the elongation of a cylindrical slice of length l at x we can equate du/dx to the strain rate $(1/l)dl/dt$, differentiate the volume of the cylinder to relate it to the rate of change of fibre radius dr/dt, and finally use Eq. (A.1) to obtain the rate of change of fibre radius with x

$$\frac{dr}{dx} = \frac{dr}{dt}/\frac{dx}{dt} = -\frac{Fr(x)}{6\pi u_{\mathrm{f}} r_1^2 \mu(x)}. \tag{A.5}$$

For the case of a preform containing a hole we will use this result in two ways. Firstly, Eq.(A.5) describes the drawdown of the incompressible glassy portions of the fibre

$$\frac{d\rho}{dx} = -\frac{F\rho(x)}{6\pi u_{\mathrm{f}} r_1^2 \mu(x)}, \tag{A.6}$$

Here the drawdown ratio $\rho(x)$ of Eq. (A.2) is generalised so that r values in Eqs. (A.2) and (A.3) are defined by

$$r(x) = r_1\rho(x) = \sqrt{\frac{A(x)}{\pi}}, \tag{A.7}$$

where *A(x)* is the cross-sectional area of glass at position *x*. In other words, r is the radius the fibre would have if all holes had collapsed and the fibre had circularised. This interpretation is justified because it is really the glass cross-section A that enters directly into both Eqs. (A.1) and (A.4).

Secondly, Eq. (A.5) also describes the variation of hole radius R in the absence of deforming forces, under the action of drawdown alone:

$$\frac{dR}{dx} = -\frac{FR(x)}{6\pi u_{\mathrm{f}} r_1^2 \mu(x)}. \tag{A.8}$$

A.2 Transverse pressures

The theory of surface tension has also been discussed in Chapter 2. For the completeness of this model, we present some of familiar results here. Surface

tension γ_{st} at the hole boundary exherts an inward pressure p_{st} according to the Young-Laplace equation

$$p_{\mathrm{st}} = \frac{\gamma_{\mathrm{st}}}{R}. \tag{A.9}$$

Since the hole is small compared to the size of the preform, the $1/R$ dependence means that surface tension at the outer boundary of the preform can be neglected.

If the hole is changing size, the viscosity μ causes an effective pressure p_{v} that opposes the change in size. This effective pressure (defined positive if acting inwards) is

$$p_{\mathrm{v}} = \frac{2\mu}{R}\frac{dR}{dt}, \tag{A.10}$$

with the strain rate in [159] expressed in terms of rate of change of R. If the hole is expanding ($dR/dt > 0$) viscosity acts like an inward pressure ($p_v > 0$) whereas if the hole is shrinking ($dR/dt < 0$) it acts like an outward pressure ($p_v < 0$). Again we can neglect viscosity at the outer boundary of the preform (more precisely, the lack of viscous forces due to the glass that isn't there between the outer radius and infinity).

Finally there may be an ordinary hydrostatic pressure difference applied between the pressure p_{H} of the gas in the hole and the atmospheric pressure p_{a} outside, with a net outward pressure of

$$p_{\mathrm{o}} = p_{\mathrm{H}} - p_{\mathrm{a}}. \tag{A.11}$$

Again neglecting inertia because all accelerations are small, these pressures must be balanced. The resulting equation gives the rate of change of hole size with x using Eq. (A.1), as we did with Eq. (A.5)

$$\frac{dR}{dx} = \frac{\rho^2}{2u_{\mathrm{f}}\mu}(Rp_o - \gamma_{\mathrm{st}}). \tag{A.12}$$

A.3 Solution

For small intervals of time or distance, the small changes of hole radius due to drawdown Eq. (A.8) and pressure Eq. (A.12) can be added to give a differential equation for *R(x)*

$$\frac{dR}{dx} = -\frac{F}{6\pi u_{\mathrm{f}} r_1^2 \mu(x)} \left\{ \left[1 - \frac{3\pi r_1^2 p_{\mathrm{o}}}{F} \rho^2(x) \right] R(x) + \frac{3\pi r_1^2 \gamma_{\mathrm{st}}}{F} \rho^2(x) \right\}. \tag{A.13}$$

This equation can in principle be solved given the viscosity profile $\mu(x)$, with the drawdown profile $\rho(x)$ obtained by solving Eq. (A.6). However, if instead ρ is chosen to be the independent variable with the aid of Eq. (A.6) we obtain

$$\frac{dR}{d\rho} + \left[\frac{3\pi r_1^2 p_{\mathrm{o}}}{F} \rho - \frac{1}{\rho} \right] R(\rho) = \frac{3\pi r_1^2 \gamma_{\mathrm{st}}}{F} \rho. \tag{A.14}$$

A crucial consequence of the change of variable, along with the inclusion of the draw tension F in the analysis at the outset, is that the viscosity profile $\mu(x)$ has now been completely eliminated from the problem. This is at the cost of losing information about length scales along x, but does not prevent us finding the hole size in the final fibre because the appropriate final condition $\rho = \rho_0$ is well defined.

Eq. (A.14) is a first-order linear differential equation for hole radius $R(\rho)$ as a function of local drawdown ratio, which varies from $\rho = 1$ at the preform ($x \to -\infty$) to $\rho = \rho_0 = r_2/r_1$ at the final fibre ($x \to \infty$). It can be solved by the integrating factor method to give

$$R(\rho) = \rho e^{\frac{-3\pi p_o r_1^2}{2F}\rho^2} \left[e^{\frac{3\pi p_o r_1^2}{2F}} R_0 - \frac{3\pi \gamma_{st} r_1^2}{F} \int_\rho^1 e^{\frac{3\pi p_o r_1^2}{2F} z^2} dz \right]. \tag{A.15}$$

where R_0 is the initial hole radius (in the preform). This is the Eq. (3.1) in the chapter 3. We define s the mean draw stress in the glass in the final fibre

$$s = \frac{F}{\pi r_2^2}, \tag{A.16}$$

and the normalised parameter E combining the excess pressure in the hole and the draw stress

$$E = \frac{3p_o}{2s\rho_0^2} = \frac{3\pi p_o r_2^2}{2F\rho_0^2} = \frac{3\pi p_o r_1^2}{2F}, \tag{A.17}$$

E is actually the exaggeration parameter defined in the chapter 3. Eq. (A.15) can then be simplified as

$$R(\rho) = \rho e^{-E\rho^2} \left[e^E R_0 - \frac{3\gamma_{st}}{s\rho_0^2} \int_\rho^1 e^{Ez^2} dz \right], \tag{A.18}$$

It is worth noting that the combination $s\rho_0^2$ that appears in both Eqs. (A.17) and (A.18) is the draw stress in the preform.

The integral in Eq.(A.18) does not have elementary solutions in general. However, it can be expressed in terms of the error function erf or the imaginary error function erfi, depending on the sign of E

$$\int_{\rho}^{1} e^{Ez^2} dz = \begin{cases} \frac{\sqrt{\pi}}{2\sqrt{E}} \left[\text{erfi}(\sqrt{E}) - \text{erfi}(\sqrt{E}\rho) \right] & E > 0 \\ \frac{\sqrt{\pi}}{2\sqrt{-E}} \left[\text{erf}(\sqrt{-E}) - \text{erf}(\sqrt{-E}\rho) \right] & E < 0. \\ 1 - \rho & E = 0 \end{cases} \tag{A.19}$$

Publications list

1. Y. Chen, J. M. Stone, W. J. Wadsworth, J. C. Knight, and T. A. Birks, "Bessel-like beams generated by photonic crystal fibre," in preparation for *Opt. Lett.*.

2. Y. Chen, W. J. Wadsworth, and T. A. Birks, "Ultraviolet four-wave mixing in the LP_{02} fibre mode," *Opt. Lett.,* **38**(19), 3747-3750 (2013).

3. Y. Chen, Z. Chen, W. J. Wadsworth, and T. A. Birks, "Nonlinear optics in the LP_{02} higher-order mode of a fiber," *Opt. Express,* **21**(15), 17786-17799 (2013).

4. Y. Chen and T. A. Birks, "Predicting hole sizes after fibre drawing without knowing the viscosity," *Opt. Mater. Express* **3**(3), 346-356 (2013).

5. D. F. Murphy, Y. Chen and T. A. Birks, "Ultra Mobile Optical Fibre Interferometry and FT-Spectrometry," Sense'13, Finland (2013).

6. Y. Chen, J. M. Stone, W. J. Wadsworth, J. C. Knight, and T. A. Birks, "Bessel-like beams generated by photonic crystal fibre," in *Conference on Lasers and Electro-Optics,* paper JTu1K.2. Optical Society of America (2012).

References

[1] T. A. Birks, P. J. Roberts, P. St. J. Russell, D. M. Atkin, and T. J. Shepherd. Full 2-D photonic bandgaps in silica/air structures. *Electron. Lett.*, 31(22):1941–1943, 1995.

[2] J. C. Knight, T. A. Birks, P. St. J. Russell, and D. M. Atkin. All-silica single-mode optical fiber with photonic crystal cladding. *Opt. Lett.*, 21(19):1547–1549, 1996.

[3] P. Russell. Photonic crystal fibers. *Science*, 299(5605):358–362, 2003.

[4] J. C. Knight, J. Broeng, T. A. Birks, and P. St. J. Russell. Photonic band gap guidance in optical fibers. *Science*, 282(5393):1476–1478, 1998.

[5] R. F. Cregan, B. J. Mangan, J. C. Knight, T. A. Birks, P. St. J. Russell, P. J. Roberts, and D. C. Allan. Single-mode photonic band gap guidance of light in air. *Science*, 285(5433):1537–1539, 1999.

[6] T. A. Birks, J. C. Knight, and P. St. J. Russell. Endlessly single-mode photonic crystal fiber. *Opt. Lett.*, 22(13):961–963, 1997.

[7] A. W. Snyder and J. D. Love. *Optical Waveguide Theory*. Chapman and Hall, 1983.

[8] R. Kashyap. *Fiber Bragg Gratings*. Academic Press, 2009.

[9] T. A. Birks and Y. W. Li. The shape of fiber tapers. *J. Lightwave Technol.*, 10(4):432–438, 1992.

[10] S. Leon-Saval, T. A. Birks, W. J. Wadsworth, P. St. J. Russell, and M. Mason. Supercontinuum generation in submicron fibre waveguides. *Opt. Express*, 12(13):2864–2869, 2004.

[11] G. Kakarantzas, T. A. Birks, and P. St. J. Russell. Structural long-period gratings in photonic crystal fibers. *Opt. Lett.*, 27(12):1013–1015, 2002.

[12] G. Kakarantzas, A. Ortigosa-Blanch, T. A. Birks, P. St. J. Russell, L. Farr, F. Couny, and B. J. Mangan. Structural rocking filters in highly birefringent photonic crystal fiber. *Opt. Lett.*, 28(3):158–160, 2003.

[13] W. J. Wadsworth, A. Witkowska, S. G. Leon-Saval, and T. A. Birks. Hole inflation and tapering of stock photonic crystal fibres. *Opt. Express*, 13(17):6541–6549, 2005.

[14] J. M. Dudley and J. R. Taylor. *Supercontinuum Generation in Optical Fibers*. Cambridge University Press, 2010.

[15] R. H. Stolen, E. P. Ippen, and A. R. Tynes. Raman oscillation in glass optical waveguide. *Appl. Phys. Lett.*, 20(2):62–64, 1972.

[16] E. P. Ippen and R. H. Stolen. Stimulated Brillouin scattering in optical fibers. *Appl. Phys. Lett.*, 21(11):539–541, 1972.

[17] R. H. Stolen, J. E. Bjorkholm, and A. Ashkin. Phase-matched three-wave mixing in silica fiber optical waveguides. *Appl. Phys. Lett.*, 24(7):308–310, 1974.

[18] R. Stolen. Phase-matched-stimulated four-photon mixing in silica-fiber waveguides. *IEEE J. Quantum Electron.*, 11(3):100–103, 1975.

[19] R. H. Stolen and C. Lin. Self-phase-modulation in silica optical fibers. *Phys. Rev. A*, 17(4):1448, 1978.

[20] L. F. Mollenauer, R. H. Stolen, and J. P. Gordon. Experimental observation of picosecond pulse narrowing and solitons in optical fibers. *Phys. Rev. Lett.*, 45:1095–1098, 1980.

[21] J. M. Dudley, L. Provino, N. Grossard, H. Maillotte, R. S. Windeler, B. J. Eggleton, and S. Coen. Supercontinuum generation in air–silica microstructured fibers with nanosecond and femtosecond pulse pumping. *J. Opt. Soc. Am. B*, 19(4):765–771, 2002.

[22] R. Cherif, M. Zghal, L. Tartara, and V. Degiorgio. Supercontinuum generation by higher-order mode excitation in a photonic crystal fiber. *Opt. Express*, 16(3):2147–2152, 2008.

[23] P. Nandi, Z. Chen, A. Witkowska, W. J. Wadsworth, T. A. Birks, and J. C. Knight. Characterization of a photonic crystal fiber mode converter using low coherence interferometry. *Opt. Lett.*, 34(7):1123–1125, 2009.

[24] J. A. Buck. *Fundamentals of Optical Fibers*. John Wiley & Sons Inc., 2004.

[25] D. N. Payne and A. H. Hartog. Determination of the wavelength of zero material dispersion in optical fibres by pulse-delay measurements. *Electron. Lett.*, 13(21):627–629, 1977.

[26] L. G. Cohen, C. Lin, and W. G. French. Tailoring zero chromatic dispersion into the 1.5 μm-1.6 μm low-loss spectral region of single-mode fibres. *Electron. Lett.*, 15(12):334–335, 1979.

[27] J. Hecht. *City of Light: The Story of Fiber Optics*. Oxford University Press, 1999.

[28] A. Ghatak and K. Thyagarajan. *An Introduction to Fiber Optics*. Cambridge University Press, 1998.

[29] E. Yablonovitch. Inhibited spontaneous emission in solid-state physics and electronics. *Phys. Rev. Lett.*, 58(20):2059, 1987.

[30] S. John. Strong localization of photons in certain disordered dielectric superlattices. *Phys. Rev. Lett.*, 58(23):2486–2489, 1987.

[31] J. M. Stone. *Photonic crystal fibres and their applications in the nonlinear regime*. Phd thesis, University of Bath, 2009.

[32] K. Tsujikawa, K. Tajima, and M. Ohashi. Rayleigh scattering reduction method for silica-based optical fiber. *J. Lightwave Technol.*, 18(11):1528–1532, 2000.

[33] K. Tajima. Low loss PCF by reduction of hole surface imperfection. In *Optical Communication-Post-Deadline Papers (published 2008), 2007 33rd European Conference and Exhibition of*, pages 1–2. VDE, 2007.

[34] P. J. Roberts, F. Couny, H. Sabert, B. J. Mangan, D. P. Williams, L. Farr, M. W. Mason, A. Tomlinson, T. A. Birks, J. C. Knight, and P. St. J. Russell. Ultimate low loss of hollow-core photonic crystal fibres. *Opt. Express*, 13(1):236–244, 2005.

[35] K. Nagayama, M. Kakui, M. Matsui, T. Saitoh, and Y. Chigusa. Ultra-low-loss (0.1484 dB/km) pure silica core fibre and extension of transmission distance. *Electron. Lett.*, 38(20):1168–1169, 2002.

[36] D. Derickson. *Fiber Optic Test and Measurement*. Prentice Hall, 1997.

[37] G. P. Agrawal. *Nonlinear Fibre Optics*. Academic Press, 2007.

[38] C. D. Cantrell and D. M. Hollenbeck. Fiberoptic mode functions: A tutorial. www.utdallas.edu/ cantrell/ee6328/modefunctions.pdf, 2001.

[39] A. Witkowska. *Post-processing of photonic crystal fibres and standard fibres*. Phd thesis, University of Bath, 2009.

[40] T. A. Birks, D. Mogilevtsev, J. C. Knight, P. S. J. Russell, J. Broeng, P. J. Roberts, J. A. West, D. C. Allan, and J. C. Fajardo. The analogy between photonic crystal fibres and step index fibres. In *Optical Fiber Communication Conference, 1999, and the International Conference on Integrated Optics and Optical Fiber Communication. OFC/IOOC'99. Technical Digest*, volume 4, pages 114–116. IEEE, 1999.

[41] K. Saitoh, Y. Tsuchida, M. Koshiba, and N. A. Mortensen. Endlessly single-mode holey fibers: the influence of core design. *Opt. Express*, 13(26):10833–10839, 2005.

[42] K. Lai. Core shape transitions in photonic crystal fibres. Master's thesis, University of Bath, 2006.

[43] I. H. Malitson. Interspecimen comparison of the refractive index of fused silica. *J. Opt. Soc. Am.*, 55(10):1205–1208, 1965.

[44] N. Bai, E. Ip, Y. K. Huang, E. Mateo, F. Yaman, M.-J. Li, S. Bickham, S Ten, J. Liñares, C. Montero, et al. Mode-division multiplexed transmission with inline few-mode fiber amplifier. *Opt. Express*, 20(3):2668–2680, 2012.

[45] L. Gruner-Nielsen, Y. Sun, J. W. Nicholson, D. Jakobsen, K. G. Jespersen, R. Lingle, and B. Pálsdóttir. Few mode transmission fiber with low dgd, low mode coupling, and low loss. *J. Lightwave Technol.*, 30(23):3693–3698, 2012.

[46] M. Tateda, N. Shibata, and S. Seikai. Interferometric method for chromatic dispersion measurement in a single-mode optical fiber. *IEEE J. Quantum Electron.*, 17(3):404–407, 1981.

[47] W. H. Reeves. *Photonic crystal fibre : the ultra-fattened dispersion regime.* PhD thesis, University of Bath, 2003.

[48] Y. Chen and T. A. Birks. Predicting hole sizes after fibre drawing without knowing the viscosity. *Opt. Mater. Express*, 3(3):346–356, 2013.

[49] J. M. Dudley, G. Genty, and S. Coen. Supercontinuum generation in photonic crystal fiber. *Rev. Mod. Phys.*, 78(4):1135–1184, 2006.

[50] A. V. Husakou and J. Herrmann. Supercontinuum generation of higher-order solitons by fission in photonic crystal fibers. *Phys. Rev. Lett.*, 87(20):203901–203901, 2001.

[51] J. Herrmann, U. Griebner, N. Zhavoronkov, A. Husakou, D. Nickel, J. C. KKnight, W. J. Wadsworth, P. St. J Russell, and G. Korn. Experimental evidence for supercontinuum generation by fission of higher-order solitons in photonic fibers. *Phys. Rev. Lett.*, 88(17):173901, 2002.

[52] G. J. Pearce, T. D. Hedley, and D. M. Bird. Adaptive curvilinear coordinates in a plane-wave solution of maxwells equations in photonic crystals. *Phys. Rev. B*, 71(19):195108, 2005.

[53] W. J. Wadsworth, N. Joly, J. C. Knight, T. A. Birks, F. Biancalana, and P. St. J. Russell. Supercontinuum and four-wave mixing with Q-switched pulses in endlessly single-mode photonic crystal fibres. *Opt. Express*, 12(2):299–309, 2004.

[54] S. Coen, A. H. L. Chau, R. Leonhardt, J. D. Harvey, J. C. Knight, W. J. Wadsworth, and P. St. J. Russell. Supercontinuum generation by stimulated Raman scattering and parametric four-wave mixing in photonic crystal fibers. *J. Opt. Soc. Am. B*, 19(4):753–764, 2002.

[55] N. Akhmediev and M. Karlsson. Cherenkov radiation emitted by solitons in optical fibers. *Phys. Rev. A*, 51(3):2602–2607, 1995.

[56] A. V. Gorbach and D. V. Skryabin. Light trapping in gravity-like potentials and expansion of supercontinuum spectra in photonic-crystal fibres. *Nat. Photonics*, 1(11):653–657, 2007.

[57] A. V. Gorbach and D. V. Skryabin. Theory of radiation trapping by the accelerating solitons in optical fibers. *Phys. Rev. A*, 76(5):053803, 2007.

[58] J. K. Ranka, R. S. Windeler, and A. J. Stentz. Visible continuum generation in air-silica microstructure optical fibers with anomalous dispersion at 800 nm. *Opt. Lett.*, 25(1):25–27, 2000.

[59] R. R. Alfano and S. L. Shapiro. Emission in the region 4000 to 7000 Å via four-photon coupling in glass. *Phys. Rev. Lett.*, 24(11):584–587, 1970.

[60] http://www.bath.ac.uk/physics/groups/cppm/tapers.php.

[61] B. S. Kawasaki, K. O. Hill, and R. G. Lamont. Biconical-taper single-mode fiber coupler. *Opt. Lett.*, 6(7):327–328, 1981.

[62] K. P. Jedrzejewski, F. Martinez, J. D. Minelly, C. D. Hussey, and F. P. Payne. Tapered-beam expander for single-mode optical-fibre gap devices. *Electron. Lett.*, 22(2):105–106, 1986.

[63] J. D. Love, W. M. Henry, W. J. Stewart, R. J. Black, S. Lacroix, and F. Gonthier. Tapered single-mode fibres and devices. I. adiabaticity criteria. *IEE Proc.*, 138(5):343–354, 1991.

[64] D. Tabor. *Gases, Liquids and Solids*. Penguin Books, 1969.

[65] W. D. Kingery. Surface tension of some liquid oxides and their temperature coefficients. *J. Am. Ceram. Soc.*, 42(1):6–10, 1959.

[66] T. A. Birks' private analysis.

[67] A. Witkowska, K. Lai, S. G. Leon-Saval, W. J. Wadsworth, and T. A. Birks. All-fiber anamorphic core-shape transitions. *Opt. Lett.*, 31(18):2672–2674, 2006.

[68] A. L. Yarin, P. Gospodinov, and V. I. Roussinov. Stability loss and sensitivity in hollow fiber drawing. *Phys. Fluids*, 6:1454, 1994.

[69] A. D. Fitt, K. Furusawa, T. M. Monro, C. P. Please, and D. J. Richardson. The mathematical modelling of capillary drawing for holey fibre manufacture. *J. Eng. Math.*, 43(2-4):201–227, 2002.

[70] S. C. Xue, R. I. Tanner, G. W. Barton, R. Lwin, M. C. J. Large, and L. Poladian. Fabrication of microstructured optical fibers-part I: Problem formulation and numerical modeling of transient draw process. *J. Lightwave Technol.*, 23(7):2245, 2005.

[71] S. C. Xue, M. C. J. Large, G. W. Barton, R. I. Tanner, L. Poladian, and R. Lwin. Role of material properties and drawing conditions in the fabrication of microstructured optical fibers. *J. Lightwave Technol.*, 24(2):853–860, 2006.

[72] R. M. Wynne. A fabrication process for microstructured optical fibers. *J. Lightwave Technol.*, 24(11):4304–4313, 2006.

[73] C. J. Voyce, A. D. Fitt, and T. M. Monro. Mathematical modeling as an accurate predictive tool in capillary and microstructured fiber manufacture: the effects of preform rotation. *J. Lightwave Technol.*, 26(7):791–798, 2008.

[74] R. H. Doremus. Viscosity of silica. *J. Appl. Phys.*, 92(12):7619–7629, 2002.

[75] W. Reeves, J. Knight, P. Russell, and P. Roberts. Demonstration of ultra-flattened dispersion in photonic crystal fibers. *Opt. Express*, 10(14):609–613, 2002.

[76] K. O'Mahoney and D. Murphy. A static fiber Fourier transform spectrometer. In *Frontiers in Optics*. Optical Society of America, 2011.

[77] S. Johnson, M. Ibanescu, M. Skorobogatiy, O. Weisberg, T. Engeness, M. Soljacic, S. Jacobs, J. Joannopoulos, and Y. Fink. Low-loss asymptotically single-mode propagation in large-core omniguide fibers. *Opt. Express*, 9(13):748–779, 2001.

[78] Q. Zhan. Cylindrical vector beams: from mathematical concepts to applications. *Adv. Opt. Photon.*, 1(1):1–57, 2009.

[79] S. Ramachandran. Dispersion-tailored few-mode fibers: a versatile platform for in-fiber photonic devices. *J. Lightwave Technol.*, 23(11):3426–3443, 2005.

[80] S. Ramachandran, S. Ghalmi, J. W. Nicholson, M. F. Yan, P. Wisk, E. Monberg, and F. V. Dimarcello. Anomalous dispersion in a solid, silica-based fiber. *Opt. Lett.*, 31(17):2532–2534, 2006.

[81] F. Poletti and P. Horak. Dynamics of femtosecond supercontinuum generation in multimode fibers. *Opt. Express*, 17(8):6134–6147, 2009.

[82] S. Ramachandran and S. Ghalmi. "Diffraction-free," self-healing Bessel beams from fibers. *in CLEO/QELS, OSA Technical Digest (OSA, 2008), paper CPDB5*, 2008.

[83] Y. Chen, J. M. Stone, W. J. Wadsworth, J. C. Knight, and T. A. Birks. Bessel-like beams generated by photonic crystal fibre. In *CLEO: Applications and Technology*. Optical Society of America, 2012.

[84] H. R. Stuart. Dispersive multiplexing in multimode optical fiber. *Science*, 289(5477):281–283, 2000.

[85] C. Yu, J. Liou, Y. Chiu, and H. Taga. Mode multiplexer for multimode transmission in multimode fibers. *Opt. Express*, 19(13):12673–12678, 2011.

[86] M. Imai and E. H. Hara. Excitation of fundamental and low-order modes of optical fiber waveguides by gaussian beams. 1: Tilted beams. *Appl. Opt.*, 13(8):1893–1899, 1974.

[87] M. Imai and E. H. Hara. Excitation of the fundamental and low-order modes of optical fiber waveguides with gaussian beams. 2: Offset beams. *Appl. Opt.*, 14(1):169–173, 1975.

[88] M. Hu, C. Wang, Y. Song, Y. Li, L. Chai, E. E. Serebryannikov, and A. M. Zheltikov. A hollow beam from a holey fiber. *Opt. Express*, 14(9):4128–4134, 2006.

[89] W. Q. Thornburg, B. J. Corrado, and X. D. Zhu. Selective launching of higher-order modes into an optical fiber with an optical phase shifter. *Opt. Lett.*, 19(7):454–456, 1994.

[90] M. Skorobogatiy, C. Anastassiou, S. G. Johnson, O. Weisberg, T. D. Engeness, S. A. Jacobs, R. U. Ahmad, and Y. Fink. Quantitative characterization of higher-order mode converters in weakly multimoded fibers. *Opt. Express*, 11(22):2838–2847, 2003.

[91] T. G. Euser, G. Whyte, M. Scharrer, J. S. Y. Chen, A. Abdolvand, J. Nold, C. F. Kaminski, and P. St. J. Russell. Dynamic control of higher-order

modes in hollow-core photonic crystal fibers. *Opt. Express*, 16(22):17972–17981, 2008.

[92] K. Lai, S. G. Leon-Saval, A. Witkowska, W. J. Wadsworth, and T. A. Birks. Wavelength-independent all-fiber mode converters. *Opt. Lett.*, 32(4):328–330, 2007.

[93] A. Witkowska, S. G. Leon-Saval, A. Pham, and T. A. Birks. All-fiber LP_{11} mode convertors. *Opt. Lett.*, 33(4):306–308, 2008.

[94] *BeamPROP by RSoft, http://www.rsoft.com.*

[95] I. Gris-Sanchez, B. J. Mangan, and J. C. Knight. Reducing spectral attenuation in small-core photonic crystal fibers. *Opt. Mater. Express*, 1(2):179–184, 2011.

[96] T. Okuno, M. Onishi, T. Kashiwada, S. Ishikawa, and M. Nishimura. Silica-based functional fibers with enhanced nonlinearity and their applications. *IEEE J. Sel. Top. Quantum Electron.*, 5(5):1385–1391, 1999.

[97] J. Hansryd, P. A. Andrekson, M. Westlund, J. Li, and P. Hedekvist. Fiber-based optical parametric amplifiers and their applications. *IEEE J. Sel. Top. Quantum Electron.*, 8(3):506–520, 2002.

[98] C. J. McKinstrie, S. Radic, and A. R. Chraplyvy. Parametric amplifiers driven by two pump waves. *IEEE J. Sel. Top. Quantum Electron.*, 8(3):538–547, 2002.

[99] J. van Howe, J. H. Lee, S. Zhou, F. Wise, C. Xu, S. Ramachandran, S. Ghalmi, and M. F. Yan. Demonstration of soliton self-frequency shift below 1300nm in higher-order mode, solid silica-based fiber. *Opt. Lett.*, 32(4):340–342, 2007.

[100] J. E. Sharping, M. Fiorentino, A. Coker, P. Kumar, and R. S. Windeler. Four-wave mixing in microstructure fiber. *Opt. Lett.*, 26(14):1048–1050, 2001.

[101] H. N. Paulsen, K. M. Hilligse, J. Thøgersen, S. R. Keiding, and J. J. Larsen. Coherent anti-Stokes Raman scattering microscopy with a photonic crystal fiber based light source. *Opt. Lett.*, 28(13):1123–1125, 2003.

[102] A. Kudlinski, A. K. George, J. C. Knight, J. C. Travers, A. B. Rulkov, S. V. Popov, and J. R. Taylor. Zero-dispersion wavelength decreasing photonic crystal fibers for ultraviolet-extended supercontinuum generation. *Opt. Express*, 14(12):5715–5722, 2006.

[103] J. H. V. Price, T. M. Monro, H. Ebendorff-Heidepriem, F. Poletti, P. Horak, V. Finazzi, J. Y. Y. Leong, P. Petropoulos, J. C. Flanagan, G. Brambilla, X. Feng, and D. J. Richardson. Mid-IR supercontinuum generation from nonsilica microstructured optical fibers. *IEEE J. Sel. Top. Quantum Electron.*, 13(3):738–749, 2007.

[104] S. P. Stark, F. Biancalana, A. Podlipensky, and P. St. J. Russell. Nonlinear wavelength conversion in photonic crystal fibers with three zero-dispersion points. *Phys. Rev. A*, 83(2):023808, 2011.

[105] N. Granzow, S. P. Stark, M. A. Schmidt, A. S. Tverjanovich, L. Wondraczek, and P. St. J. Russell. Supercontinuum generation in chalcogenide-silica step-index fibers. *Opt. Express*, 19(21):21003–21010, 2011.

[106] S. Ramachandran, Z. Wang, and M. Yan. Bandwidth control of long-period grating-based mode converters in few-mode fibers. *Opt. Lett.*, 27(9):698–700, 2002.

[107] A. Mussot, T. Sylvestre, L. Provino, and H. Maillotte. Generation of a broadband single-mode supercontinuum in a conventional dispersion-shifted fiber by use of a subnanosecond microchip laser. *Opt. Lett.*, 28(19):1820–1822, 2003.

[108] C. Lesvigne, V. Couderc, A. Tonello, P. Leproux, A. Barthélémy, S. Lacroix, F. Druon, P. Blandin, M. Hanna, and P. Georges. Visible supercontinuum generation controlled by intermodal four-wave mixing in microstructured fiber. *Opt. Lett.*, 32(15):2173–2175, 2007.

[109] J. M. Stone and J. C. Knight. From zero dispersion to group index matching: How tapering fibers offers the best of both worlds for visible supercontinuum generation. *Opt. Fiber Technol.*, 2012.

[110] J. C. Travers, S. V. Popov, and J. R. Taylor. Extended blue supercontinuum generation in cascaded holey fibers. *Opt. Lett.*, 30(23):3132–3134, 2005.

[111] J. M. Stone and J. C. Knight. Visibly "white" light generation in uniform photonic crystal fiber using a microchip laser. *Opt. Express*, 16(4):2670–2675, 2008.

[112] J. C. Knight, J. Arriaga, T. A. Birks, A. Ortigosa-Blanch, W. J. Wadsworth, and P. St. J. Russell. Anomalous dispersion in photonic crystal fiber. *IEEE Photon. Technol. Lett.*, 12(7):807–809, 2000.

[113] T. A. Birks, D. Mogilevtsev, and P. St. J. Knight, J. C. andRussell. Dispersion compensation using single-material fibers. *IEEE Photon. Technol. Lett.*, 11(6):674–676, 1999.

[114] C. D. Poole, J. M. Wiesenfeld, D. J. Digiovanni, and A. M. Vengsarkar. Optical fiber-based dispersion compensation using higher order modes near cutoff. *J. Lightwave Technol.*, 12(10):1746–1758, 1994.

[115] J. D. Joannopoulos, S. G. Johnson, J. N. Winn, and R. D. Meade. *Photonic Crystals: Molding The Flow of Light*. Princeton university press, 2008.

[116] A. Mussot, E. Lantz, H. Maillotte, T. Sylvestre, C. Finot, and S. Pitois. Spectral broadening of a partially coherent CW laser beam in single-mode optical fibers. *Opt. Express*, 12(13):2838–2843, 2004.

[117] A. V. Yulin, D. V. Skryabin, and P. St. J. Russell. Four-wave mixing of linear waves and solitons in fibers with higher-order dispersion. *Opt. Lett.*, 29(20):2411–2413, 2004.

[118] L. Skuja. Optically active oxygen-deficiency-related centers in amorphous silicon dioxide. *J. Non-Cryst. Solids*, 239(1):16–48, 1998.

[119] K. Kajihara, L. Skuja, M. Hirano, and H. Hosono. Formation and decay of nonbridging oxygen hole centers in SiO_2 glasses induced by F_2 laser irradiation: In situ observation using a pump and probe technique. *Appl. Phys. Lett.*, 79:1757, 2001.

[120] K. Nagasawa, Y. Hoshi, Y. Ohki, and K. Yahagi. Improvement of radiation resistance of pure silica core fibers by hydrogen treatment. *Jpn. J. Appl. Phys.*, 24(9):1224–1228, 1985.

[121] Y. Chen, W. J. Wadsworth, and T. A. Birks. Ultraviolet four-wave mixing in the LP_{02} fibre mode. *Opt. Lett.*, 38(19):3747–3750, 2013.

[122] http://www.fianium.com/.

[123] T. Ohara, H. Takara, T. Yamamoto, H. Masuda, T. Morioka, M. Abe, and H. Takahashi. Over-1000-channel ultradense WDM transmission with supercontinuum multicarrier source. *J. Lightwave Technol.*, 24(6):2311–2317, 2006.

[124] K. Washio, K. Inoue, and S. Kishida. Efficient large-frequency-shifted three-wave mixing in low dispersion wavelength region in single-mode optical fibre. *Electron. Lett.*, 16(17):658–660, 1980.

[125] C. Lin, W. A. Reed, A. D. Pearson, and H. T. Shang. Phase matching in the minimum-chromatic-dispersion region of single-mode fibers for stimulated four-photon mixing. *Opt. Lett.*, 6(10):493–495, 1981.

[126] D. K. Serkland and P. Kumar. Tunable fiber-optic parametric oscillator. *Opt. Lett.*, 24(2):92–94, 1999.

[127] W. H. Reeves, D. V. Skryabin, F. Biancalana, J. C. Knight, P. St. J. Russell, F. G. Omenetto, A. Efimov, and A. J. Taylor. Transformation and control of ultra-short pulses in dispersion-engineered photonic crystal fibres. *Nature*, 424(6948):511–515, 2003.

[128] C. Lin and M. A. Bosch. Large-stokes-shift stimulated four-photon mixing in optical fibers. *Appl. Phys. Lett.*, 38(7):479–481, 1981.

[129] J. Cheng, M. E. V. Pedersen, K. Charan, K. Wang, C. Xu, L. Gruner-Nielsen, and D. Jakobsen. Intermodal four-wave mixing in a higher-order-mode fiber. *Appl. Phys. Lett.*, 101(16):161106–161106, 2012.

[130] J. D. Harvey, R. Leonhardt, S. Coen, G. K. L. Wong, J. C. Knight, W. J. Wadsworth, and P. S. J. Russell. Scalar modulation instability in the normal dispersion regime by use of a photonic crystal fiber. *Opt. Lett.*, 28(22):2225–2227, 2003.

[131] C. Xiong, Z. Chen, and W. J. Wadsworth. Dual-wavelength-pumped supercontinuum generation in an all-fiber device. *J. Lightwave Technol.*, 27(11):1638–1643, 2009.

[132] L. Lavoute, J. C. Knight, P. Dupriez, and W. J. Wadsworth. High power red and near-IR generation using four wave mixing in all integrated fibre laser systems. *Opt. Express*, 18(15):16193–16205, 2010.

[133] Y. Chen, Z. Chen, W. J. Wadsworth, and T. A. Birks. Nonlinear optics in the LP_{02} higher-order mode of a fibre. *Opt. Express*, 21(15):17786–17799, 2013.

[134] A. E. Siegman. *Lasers*. University Science, 1986.

[135] M. Mazilu, D. J. Stevenson, F. Gunn-Moore, and K. Dholakia. Light beats the spread:non-diffracting beams. *Laser Photon. Rev.*, 4(4):529–547, 2010.

[136] J. Durnin. Exact solutions for nondiffracting beams. I. the scalar theory. *J. Opt. Soc. Am. A*, 4(4):651–654, 1987.

[137] J. Durnin, J. J. Jr. Miceli, and J. H. Eberly. Diffraction-free beams. *Phys. Rev. Lett.*, 58(15):1499–1501, 1987.

[138] D. McGloin and K. Dholakia. Bessel beams: diffraction in a new light. *Contemp. Phys.*, 46(1):15–28, 2005.

[139] F. Gori, G. Guattari, and C. Padovani. Bessel-Gauss beams. *Opt. Commun.*, 64(6):491–495, 1987.

[140] V. Garcés-Chávez, D. McGloin, H. Melville, W. Sibbett, and K. Dholakia. Simultaneous micromanipulation in multiple planes using a self-reconstructing light beam. *Nature*, 419(6903):145–147, 2002.

[141] J. Arlt, V. Garces-Chavez, W. Sibbett, and K. Dholakia. Optical micromanipulation using a Bessel light beam. *Opt. Commun.*, 197(4):239–245, 2001.

[142] B. Hafizi, E. Esarey, and P. Sprangle. Laser-driven acceleration with Bessel beams. *Phys. Rev. E*, 55(3):3539, 1997.

[143] P. Dufour, M. Piché, Y. De Koninck, and N. McCarthy. Two-photon excitation fluorescence microscopy with a high depth of field using an axicon. *Appl. Opt.*, 45(36):9246–9252, 2006.

[144] F. Courvoisier, P-A. Lacourt, M. Jacquot, M. K. Bhuyan, L. Furfaro, and J. M. Dudley. Surface nanoprocessing with nondiffracting femtosecond Bessel beams. *Opt. Lett.*, 34(20):3163–3165, 2009.

[145] M. K. Bhuyan, F. Courvoisier, P. A. Lacourt, M. Jacquot, R. Salut, L. Furfaro, and J. M. Dudley. High aspect ratio nanochannel machining using single shot femtosecond Bessel beams. *Appl. Phys. Lett.*, 97(8):081102–081102, 2010.

[146] T. Wulle and S. Herminghaus. Nonlinear optics of Bessel beams. *Phys. Rev. Lett.*, 70(10):1401–1404, 1993.

[147] J. H. McLeod. The axicon: a new type of optical element. *J. Opt. Soc. Am.*, 44(8):592–592, 1954.

[148] G. Indebetouw. Nondiffracting optical fields: some remarks on their analysis and synthesis. *J. Opt. Soc. Am. A*, 6(1):150–152, 1989.

[149] S. K. Eah, W. Jhe, and Y. Arakawa. Nearly diffraction-limited focusing of a fiber axicon microlens. *Rev. Sci. Instrum.*, 74(11):4969–4971, 2003.

[150] T. Grosjean, S. S. Saleh, M. A. Suarez, I. A. Ibrahim, V. Piquerey, D. Charraut, and P. Sandoz. Fiber microaxicons fabricated by a polishing technique for the generation of Bessel-like beams. *Appl. Opt.*, 46(33):8061–8067, 2007.

[151] X. Zhu, A. Schulzgen, L. Li, and N. Peyghambarian. Generation of controllable nondiffracting beams using multimode optical fibers. *Appl. Phys. Lett.*, 94(20):201102–201102, 2009.

[152] S. R. Lee, J. Kim, S. Lee, Y. Jung, J. K. Kim, and K. Oh. All-silica fiber Bessel-like beam generator and its applications in longitudinal optical trapping and transport of multiple dielectric particles. *Opt. Express*, 18(24):25299–25305, 2010.

[153] P. Steinvurzel, K. Tantiwanichapan, M. Goto, and S. Ramachandran. Fiber-based Bessel beams with controllable diffraction-resistant distance. *Opt. Lett.*, 36(23):4671–4673, 2011.

[154] F. Benabid, F. Couny, J. C. Knight, T. A. Birks, and P. St. J. Russell. Compact, stable and efficient all-fibre gas cells using hollow-core photonic crystal fibres. *Nature*, 434(7032):488–491, 2005.

[155] J. D. Love. Single-, few-, and multimode Y-junctions. *J. Lightwave Technol.*, 30(3):304–309, 2012.

[156] J. K. Kim, J. Kim, Y. Jung, W. Ha, Y. S. Jeong, S. Lee, A. Tünnermann, and K. Oh. Compact all-fiber Bessel beam generator based on hollow optical fiber combined with a hybrid polymer fiber lens. *Opt. Lett.*, 34(19):2973–2975, 2009.

[157] Y. Y. Yu, D. Z. Lin, L. S. Huang, and C. K. Lee. Effect of subwavelength annular aperture diameter on the nondiffracting region of generated Bessel beams. *Opt. Express*, 17(4):2707–2713, 2009.

[158] F. T. Trouton. On the coefficient of viscous traction and its relation to that of viscosity. *Proc. R. Soc. London Ser. A*, 77(519):426–440, 1906.

[159] R. T. Knapp, J. W. Daily, and F. G. Hammitt. *Cavitation*. McGraw-Hill New York, 1970.